

NUMERICAL AND EXPERIMENTAL EVALUATION OF COMPUTATIONAL  
SPECTRAL IMAGING WITH PHOTON SIEVES

A THESIS SUBMITTED TO  
THE GRADUATE SCHOOL OF NATURAL AND APPLIED SCIENCES  
OF  
MIDDLE EAST TECHNICAL UNIVERSITY

BY

TUNÇ ALKANAT

IN PARTIAL FULFILLMENT OF THE REQUIREMENTS  
FOR  
THE DEGREE OF MASTER OF SCIENCE  
IN  
ELECTRICAL AND ELECTRONICS ENGINEERING

SEPTEMBER 2016



Approval of the thesis:

**NUMERICAL AND EXPERIMENTAL EVALUATION OF COMPUTATIONAL  
SPECTRAL IMAGING WITH PHOTON SIEVES**

submitted by **TUNÇ ALKANAT** in partial fulfillment of the requirements for the degree of **Master of Science in Electrical and Electronics Engineering Department, Middle East Technical University** by,

Prof. Dr. Gülbin Dural Ünver  
Dean, Graduate School of **Natural and Applied Sciences** \_\_\_\_\_

Prof. Dr. Tolga Çiloğlu  
Head of Department, **Electrical and Electronics Engineering** \_\_\_\_\_

Assist. Prof. Dr. Figen S. Öktem  
Supervisor, **Electrical and Electronics Engineering Dept., METU** \_\_\_\_\_

**Examining Committee Members:**

Prof. Dr. Gözde Bozdağı Akar  
Electrical and Electronics Engineering Department, METU \_\_\_\_\_

Assist. Prof. Dr. Figen S. Öktem  
Electrical and Electronics Engineering Department, METU \_\_\_\_\_

Prof. Dr. Çağatay Candan  
Electrical and Electronics Engineering Department, METU \_\_\_\_\_

Assist. Prof. Dr. Selçuk Yerci  
Micro and Nanotechnology Programme, METU \_\_\_\_\_

Prof. Dr. Haldun M. Özaktaş  
Electrical and Electronics Engineering Dept., Bilkent University \_\_\_\_\_

**Date:** \_\_\_\_\_



**I hereby declare that all information in this document has been obtained and presented in accordance with academic rules and ethical conduct. I also declare that, as required by these rules and conduct, I have fully cited and referenced all material and results that are not original to this work.**

Name, Last Name: TUNÇ ALKANAT

Signature :

# ABSTRACT

## NUMERICAL AND EXPERIMENTAL EVALUATION OF COMPUTATIONAL SPECTRAL IMAGING WITH PHOTON SIEVES

Alkanat, Tunç

M.S., Department of Electrical and Electronics Engineering

Supervisor : Assist. Prof. Dr. Figen S. Öktem

September 2016, 94 pages

Spectral imaging, the simultaneous imaging and spectroscopy of a radiating scene, is an important diagnostic tool for an expanding range of applications in physics, chemistry, biology, medicine, astronomy, and remote sensing. In this thesis, a recently developed computational imaging technique that enables high-resolution spectral imaging is studied both numerically and experimentally. This technique employs a diffractive imaging element called photon sieve, and distributes the image formation task between the photon sieve system and a data-processing unit. In the data-processing unit, the measurements obtained with the photon sieve system are used in an inverse problem framework to reconstruct the spectral images from their superimposed and blurred measurements. Here, we first develop a fast and accurate method to compute the two-dimensional point spread function (PSF) of any diffractive imaging element. Using this method, imaging properties of photon sieves are analyzed under different design scenarios. Secondly, we construct an experimental setup for the photon sieve imaging system, and PSF measurements obtained with this setup are compared with the theoretical calculations. Lastly, the image reconstruction method used to solve the inverse problem is studied and its performance is analyzed numerically for different regularization choices and various potential observing scenarios.

Keywords: Photon sieve, spectral imaging, computational imaging, diffractive imaging, point-spread function, inverse problems, image reconstruction



# ÖZ

## FOTON SÜZGECİ İLE HESAPLAMALI SPEKTRAL GÖRÜNTÜLEMENİN SAYISAL VE DENEYSEL İNCELEMESİ

Alkanat, Tunç

Yüksek Lisans, Elektrik ve Elektronik Mühendisliği Bölümü

Tez Yöneticisi : Assist. Prof. Dr. Figen S. Öktem

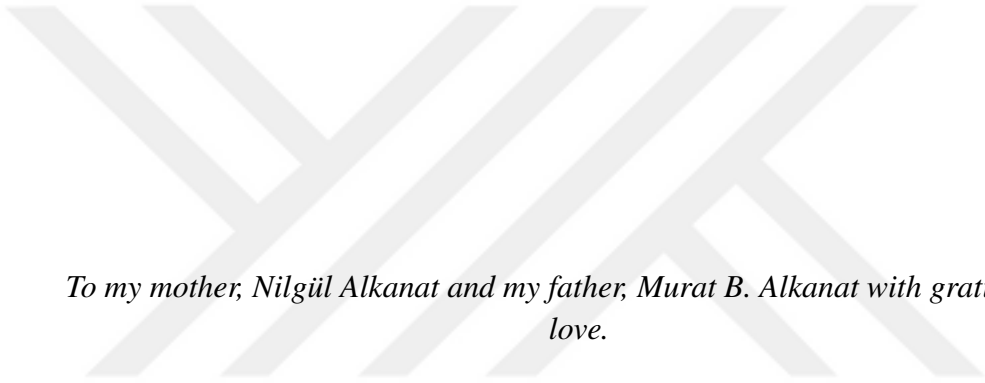
Eylül 2016 , 94 sayfa

Spektral görüntüleme, yani ışınım yapan bir ortamın eşzamanlı spektroskopisi ve görüntülenmesi, fizik, kimya, biyoloji, tıp, astronomi ve uzaktan algılama gibi uygulama alanları giderek genişleyen önemli bir teşhis aracıdır. Bu tezde, yüksek çözünürlüklü spektral görüntülemeyi mümkün kılan yeni bir hesaplamalı görüntüleme yöntemi sayısal ve deneysel olarak incelenmektedir. Bu yöntem, foton süzgeci adında kırınım tabanlı bir görüntüleme elemanı içermekte ve görüntü oluşturma işini foton süzgeci sistemi ve veri işleme birimi arasında dağıtmaktadır. Veri işleme biriminde, foton süzgeci sisteminden alınan ölçümler, ters problem çerçevesinde kullanılarak, bulanık ve üst üste eklenmiş ölçümlerden spektral görüntüler geri oluşturulmaktadır. Bu çalışmada, ilk olarak, herhangi bir kırınım tabanlı görüntüleme elemanının iki boyutlu nokta dağılım fonksiyonunu (NDF) hızlı ve hassas olarak hesaplayan bir yöntem geliştirilmiştir. Bu yöntem kullanılarak, foton süzgecinin görüntülemeye ilişkin özellikleri farklı tasarım yönleri ile incelenmiştir. İkinci olarak, spektral görüntüleme sistemi için bir deneysel ortam oluşturulmuş ve bu ortamdan alınan NDF ölçümleri kuramsal hesaplamalar ile karşılaştırılmıştır. Son olarak, görüntü geri oluşturma yöntemi çalışılmış ve olası farklı gözlem koşulları ve düzenleme seçenekleri için spektral görüntüleme sisteminin performansı sayısal olarak incelenmiştir.

Anahtar Kelimeler: Foton süzgeci, spektral görüntüleme, hesaplamalı görüntüleme, kırınım tabanlı görüntüleme, nokta dağılım fonksiyonu, ters problemler, görüntü geri oluşturma







*To my mother, Nilgöl Alkanat and my father, Murat B. Alkanat with gratitude and love.*

## ACKNOWLEDGMENTS

I would like to express my deep gratitude and appreciation to my supervisor Assist. Prof. Dr. Figen S. Öktem for her guidance, patience, continuous support and encouragement that made this study possible. I also thank Assist. Prof. Dr. Selçuk Yerci for his help on constructing the experimental setup.

I am also thankful to my employer, ASELSAN Inc., for a stimulating work environment, encouraging me during my M.Sc. studies and lending me optical equipments for experimental tests of this study.

I would like to thank to my family; my mother Nilgöl Alkanat for her unconditional love, caring, patience and wisdom, and my deceased father, Murat B. Alkanat, for his inspiring figure illuminating my way through good and bad times. I am also thankful to my *significant other*, N. Eylem İmamoğlu, for her love, patience and support. Finally, I want to express my gratitude to my friends for their emotional support and being there for me.

# TABLE OF CONTENTS

ABSTRACT . . . . .	v
ÖZ . . . . .	vii
ACKNOWLEDGMENTS . . . . .	x
TABLE OF CONTENTS . . . . .	xi
LIST OF TABLES . . . . .	xiv
LIST OF FIGURES . . . . .	xv
LIST OF ABBREVIATIONS . . . . .	xx

## CHAPTERS

1	INTRODUCTION . . . . .	1
1.1	Contributions and Outline . . . . .	3
2	REVIEW OF SPECTRAL IMAGING TECHNIQUES . . . . .	5
2.1	Spectral Imaging . . . . .	5
2.2	Spectral Imaging Terminology . . . . .	6
2.3	Spectral Imaging System Parameters . . . . .	7
2.4	Overview of Spectral Imaging Techniques . . . . .	8
2.4.1	Optics-based Techniques . . . . .	9

	2.4.1.1	Conventional Techniques . . . . .	9
	2.4.1.2	Image Slicing based Techniques . . . . .	12
	2.4.1.3	Image Dividing based Techniques . . . . .	14
	2.4.2	Computational Imaging Techniques . . . . .	16
	2.4.2.1	Transformation based Techniques . . . . .	16
	2.4.2.2	Reconstruction based Techniques . . . . .	18
3		POINT-SPREAD FUNCTIONS OF DIFFRACTIVE IMAGING ELEMENTS . . . . .	25
	3.1	Diffractive Imaging . . . . .	25
	3.1.1	Fresnel Zone Plate . . . . .	26
	3.1.2	Photon Sieves . . . . .	28
	3.2	Fast PSF Computation Method for Diffractive Imaging . . . . .	28
	3.2.1	Point-Spread Function (PSF) . . . . .	30
	3.2.2	Closed-Form PSF Formula . . . . .	30
	3.2.3	Developed Fast PSF Computation Method . . . . .	31
	3.2.4	Computational Efficiency and Accuracy of Method . . . . .	33
	3.2.5	Numerical Simulations for Photon Sieves . . . . .	33
	3.3	Experimental Validation of Theoretical PSFs . . . . .	35
	3.3.1	Experimental Setup . . . . .	35
	3.3.2	PSF Measurements and Comparisons . . . . .	40
4		PERFORMANCE ANALYSIS OF PHOTON SIEVE SPECTRAL IMAGING . . . . .	45

4.1	Computational Spectral Imaging with Photon Sieves . . . . .	45
4.2	Image Reconstruction Algorithm . . . . .	49
4.3	Performance Analysis . . . . .	53
4.3.1	Reconstruction Performance Metrics . . . . .	54
4.3.2	Utilized Images for Performance Analysis . . . . .	55
4.3.3	Regularization Choices . . . . .	58
4.4	Numerical Results . . . . .	59
4.4.1	Selection of Regularization Parameters . . . . .	60
4.4.2	Effect of Measurement Plane Locations . . . . .	66
4.4.3	Effect of Measurement Noise . . . . .	68
4.4.4	Effect of Number of Measurements . . . . .	68
4.4.5	Effect of Spectral Separation . . . . .	72
5	CONCLUSIONS . . . . .	77
5.1	Future Work . . . . .	79
APPENDICES		
A	RECONSTRUCTION PERFORMANCE FOR DIFFERENT REGU- LARIZATION PARAMETERS . . . . .	81
B	RECONSTRUCTION PERFORMANCE FOR DIFFERENT MEA- SUREMENT PLANE LOCATIONS . . . . .	87
REFERENCES . . . . .		89

## LIST OF TABLES

### TABLES

Table 3.1	Properties of the tested photon sieve. . . . .	42
Table 4.1	Reconstruction performance with optimal regularization parameters for each regularization operator and image pair. . . . .	60
Table 4.2	Changing separation between the foci of wavelengths in terms of DOF of $\lambda_2$ . . . . .	76

# LIST OF FIGURES

## FIGURES

Figure 2.1	A sample spectral image data set. Image retrieved from [1]. . . . .	5
Figure 2.2	A sample spectral datacube where each inner cube represents a voxel. Image retrieved from [2]. . . . .	7
Figure 2.3	Two spatial features become indistinguishable as the spatial spacing between them gets smaller than the spatial resolution of the imaging system. Image retrieved from [3]. . . . .	8
Figure 2.4	A sample spectral datacube with a spectral range of 500nm to 686nm and a spectral resolution of 6nm, hence consisting of a total of 32 spectral bands. Image retrieved from [4]. . . . .	9
Figure 2.5	Overview of spectral imaging techniques. . . . .	10
Figure 2.6	(a) Whiskbroom approach. (b) Pushbroom approach. (c) Tunable filter approach. Image retrieved from [5]. . . . .	11
Figure 2.7	Bowen-Walraven image slicer. Image retrieved from [2]. . . . .	12
Figure 2.8	Illustration of SRDA approach to spectral imaging. Image retrieved from [2]. . . . .	15
Figure 2.9	An MAFC implementation where each filter - detector array pair is given. Image retrieved from [2]. . . . .	17
Figure 2.10	Left: Depiction of the Computed Tomography Imaging Spectrometer (CTIS), right: An illustration of 5x5 diffraction pattern on the detector array. Image retrieved from [2]. . . . .	18
Figure 2.11	Illustration of coded aperture snapshot spectral imager. Image retrieved from [2]. . . . .	20
Figure 2.12	Illustration of photon sieve based spectral imaging approach. Image retrieved from [6]. © 2014 IEEE. . . . .	22

Figure 3.1	Single-slit experiment that illustrates the diffraction phenomena for a wider and a narrower slit. . . . .	26
Figure 3.2	(a) Aperture transmission (transmittance) function of a Fresnel zone plate with 9 transparent zones as shown with white rings. (b) A Fresnel zone plate shown along with its focus at a distance of $f$ . . . . .	27
Figure 3.3	(a) Aperture function of a Fresnel zone plate. (b) Aperture function of a photon sieve that is formed by replacing Fresnel zones in (a) with pinholes. . . . .	29
Figure 3.4	(a) RMSE between the PSFs obtained with the two methods for increasing number of samples used in the fast method. (b) Computation time versus number of processed zones for the two methods [7]. . . . .	34
Figure 3.5	(a) Cross-sections of 2-D PSFs for photon sieves with circular and square holes. (b) From top to bottom, the corresponding 2-D PSFs. (c) PSLR of the PSF versus pinhole existence probability [7]. . . . .	36
Figure 3.6	A view of the experimental setup where the optical path is depicted with a red line. . . . .	37
Figure 3.7	A depiction of the DMD chip with $M \times N$ micro-mirrors. The tilt direction of micro-mirrors is 45 degrees as shown. Image retrieved from [8].	38
Figure 3.8	A depiction of DMD chip illumination angle and micro-mirror tilt axis. Image retrieved from [8]. . . . .	40
Figure 3.9	(a) Theoretical demonstration of the "blaze" and "anti-blaze" conditions. Retrieved from [9]. (b) - (c) Experimental diffraction patterns for "blaze" and "anti-blaze" conditions, respectively. Note that in (b), most of the energy is contained within the $0^{th}$ diffraction order at the center, and in (c), most of the energy is distributed between four brightest orders. . . .	41
Figure 3.10	Aperture transmission function of the tested photon sieve. . . . .	42
Figure 3.11	(a),(c), and (e): The cross-sectional views of the theoretical and experimental PSFs, respectively, at the focus, +1 and +3 depth of focus away from the focus. (b), (d), and (f): The corresponding 2D PSFs (top: theoretical, bottom: experimental). . . . .	44
Figure 4.1	Imaging system used in photon sieve based spectral imaging technique. Image retrieved from [6]. © 2014 IEEE. . . . .	46



Figure 4.2	Top row: Obtained observations at the focus of each wavelength of interest. Second row: Contributions of the first and second sources to the observation at the focus of $\lambda_1$ . Third row: Contributions of the first and second sources to the observation at the focus of $\lambda_2$ . Bottom row: Reconstructed images for both sources. . . . .	47
Figure 4.3	Pseudo-code for the preconditioned conjugate gradient algorithm. . . . .	50
Figure 4.4	Pseudo-code for the modified preconditioned conjugate gradient algorithm. . . . .	51
Figure 4.5	(a) - (b) and (c) - (d): Two pairs of solar images that are used for performance evaluation. Note the visual resemblance of the upper pair. Pairs a-b and c-d will be referred as SI1 and SI2. Courtesy of NASA/SDO and the AIA, EVE and HMI science teams. . . . .	56
Figure 4.6	(a) - (b): A pair of images from the corrected Indian pines dataset that will be referred to as IP. . . . .	57
Figure 4.7	(a) "Cameraman" and (b) "Lena" images. . . . .	58
Figure 4.8	Reconstruction performance for different regularization operators and SI1 image pair. . . . .	61
Figure 4.9	Reconstruction performance for different image pairs and DDO operator. . . . .	62
Figure 4.10	From top to bottom: Diffraction-limited SI1 image pair, reconstructions with DDO, DCT and DWT operators for regularization. . . . .	63
Figure 4.11	From top to bottom: Diffraction-limited IP image pair, reconstructions with DDO, DCT and DWT operators for regularization. . . . .	64
Figure 4.12	From top to bottom: Diffraction-limited NI image pair, reconstructions with DDO, DCT and DWT operators for regularization. . . . .	65
Figure 4.13	Reconstruction performance for varying measurement plane locations, $d_1$ and $d_2$ , for SI1 image pair. . . . .	67
Figure 4.14	Reconstruction performance (a) in SSIM and (b) in PSNR for varying SNR levels for SI1, SI2, IP and NI image pairs. . . . .	69
Figure 4.15	Top left: First diffraction-limited intensity image of SI1 pair. Rest from left to right and top to bottom: Reconstructed images for a measurement noise with SNR values of 10, 15, 20, 25, 30, 35 and 40 dB. . . . .	70

Figure 4.16 Top left: First diffraction-limited intensity image of NI pair. Rest from left to right and top to bottom: Reconstructed images for a measurement noise with SNR values of 10, 15, 20, 25, 30, 35 and 40 dB. . . . .	71
Figure 4.17 Reconstruction performance (a) in SSIM and (b) in PSNR for varying number of observations. . . . .	73
Figure 4.18 Reconstructed images obtained with a single measurement and SNR=30 dB. Top row from left to right: single measurement taken at $(f_1 + f_2)/2$ , reconstructed images for the first and second wavelengths. Middle row from left to right: single measurement taken at $f_1$ , reconstructed images for the first and second wavelengths. Bottom row from left to right: single measurement taken at $f_2$ , reconstructed images for the first and second wavelengths. . . . .	74
Figure 4.19 Reconstruction performance for varying $\lambda_2$ and for SI1 pair of images. . . . .	75
Figure A.1 Reconstruction performance for regularization with DDO operator and for SI1 image pair where the left column shows the results in SSIM metric and the right column in PSNR. . . . .	81
Figure A.2 Reconstruction performance for regularization with DDO operator. From top to bottom: SI2, IP and NI image pairs where the left column shows the result in SSIM metric and right column in PSNR. . . . .	82
Figure A.3 Reconstruction performance for regularization with DCT operator. Top row for SI1 image pair and bottom is for SI2 where the left column shows the results in SSIM metric and right column in PSNR. . . . .	83
Figure A.4 Reconstruction performance for regularization with DCT operator. Top row for IP image pair and bottom is for NI where the left column shows the performance in SSIM metric and the right column in PSNR. . .	84
Figure A.5 Reconstruction performance for regularization with DWT operator. Top row for SI1 image pair and bottom is for SI2 where the left column shows the performance in SSIM metric and the right column in PSNR. . .	85
Figure A.6 Reconstruction performance for regularization with DWT operator. Top row for IP image pair and bottom is for NI where the left column shows the performance in SSIM metric and the right column in PSNR. . .	86
Figure B.1 Reconstruction performance for varying measurement plane locations, $d_1$ and $d_2$ , for SI1 image pair where left column is the performance in SSIM metric and right column is in PSNR. . . . .	87

Figure B.2 Reconstruction performance for varying measurement plane locations,  $d_1$  and  $d_2$ , for SI2, IP and NI image pairs, from top to bottom. Left column is the performance in SSIM metric and right column is in PSNR. . 88



## LIST OF ABBREVIATIONS

1-D	One Dimensional
2-D	Two Dimensional
3-D	Three Dimensional
AOTF	Acousto-Optical Tunable Filter
CASSI	Coded Aperture Snapshot Spectral Imager
CCD	Charge-Coupled Device
CMOS	Complementary Metal-Oxide-Semiconductor
CS	Compressive Sensing
CTIS	Computed Tomography Imaging Spectrometer
DCT	Discrete Cosine Transform
DD-CASSI	Double Dispenser - Coded Aperture Snapshot Spectral Imager
DDO	Discrete Derivative Operator
DFT	Discrete Fourier Transform
DMD	Digital Micro-Mirror Device
DOF	Depth of Focus
DWT	Discrete Wavelet Transform
EUV	Extreme Ultra-Violet
FFT	Fast Fourier Transform
FOV	Field of View
FPA	Focal-Plane Array
IFTS	Imaging Fourier Transform Spectrometer
IFU	Integral Field Unit
IMS	Image Mapping Spectrometry
IRIS	Image Replicating Imaging Spectrometer
JPEG	Joint Photographic Experts Group
LCTF	Liquid Crystal Tunable Filter
LSI	Linear Space Invariant
MAFC	Multi-Aperture Filtered Camera

MART	Multiplicative Algebraic Reconstruction Technique
MSSIM	Mean Structural Similarity Index
OTF	Optical Transfer Function
PCG	Preconditioned Conjugate Gradient
PSF	Point-Spread Function
PSLR	Peak-to-Sidelobe Ratio
PSNR	Peak Signal-to-Noise Ratio
RGB	Red-Green-Blue
RMSE	Root Mean Squared Error
SD-CASSI	Single Disperser - Coded Aperture Snapshot Spectral Imager
SHIFT	Snapshot Hyperspectral Imaging Fourier Transform Spectrometer
SNR	Signal-to-Noise Ratio
SRDA	Spectrally Resolving Detector Arrays
SSIM	Structural Similarity Index
TEI	Tunable Echelle Imager
OPD	Optical Path Difference



# CHAPTER 1

## INTRODUCTION

*The saddest aspect of life right now is that science gathers knowledge faster than society gathers wisdom[10].*

– Isaac Asimov

Spectral imaging is the acquisition of the spectrum of radiation for each spatial point in a scene. Different than a traditional grayscale image that is two-dimensional and formed by measuring the integrated intensity within a spectral range, a spectral data set is a three-dimensional data that contains multiple images of the scene, each obtained at a different narrow spectral range.

There is an ever increasing need for novel spectral imaging modalities that offer higher performance and flexibility as the applications in science and engineering grow rapidly. This is because spectral imaging provides spectral signatures for the objects in the imaged scene. More specifically, spectral information is useful for understanding the chemical composition and physical properties of the targeted objects. For instance, in astrophysics, spectral data is useful for investigating the chemical structure and reactions of celestial bodies; in mineralogy, it is useful for exploring new mining sites; and in military, it is useful for revealing threats.

Older approaches to the nearly a century and a half year old field of spectral imaging are based on optical manipulation of light. Slit spectroscopy [11] and interferometry [12] based techniques are the first approaches that enabled a scene to be viewed at different wavelengths. Then, as the manufacturing capabilities increase, techniques that involve more hardware complexity with precisely aligned and manufactured op-

tical elements are developed and improved the success of spectral imaging devices. Nevertheless, all optics-based techniques suffer from the physical limitations inherent in their optical components and face the difficulty of acquiring the three-dimensional spectral data set with the intrinsically two-dimensional detectors. As a result of these, spectral image acquisition techniques have been an active research area for a considerably long time and new approaches are still of interest to improve the spectral imaging capabilities such as spatial resolution, spectral resolution, time resolution and optical throughput.

As a result of the limitations of the optics-based techniques and the advancements in computing power, computational imaging approaches to spectral imaging have emerged. This has led to the development of novel spectral imagers with new capabilities that would not otherwise be possible with optics-based techniques. Although there is ample room for improvement and novel developments, exciting advancements in the field of computational spectral imaging are already pushing the limits in spectral imaging.

Among different computational imaging approaches for acquiring spectral information, the focus of this study is on a recently developed technique that exploits the unique properties of a diffractive imaging element called photon sieve to enable high-resolution spectral imaging. This imaging modality distributes the image formation task between the photon sieve system and a data-processing unit. In the data-processing unit, the measurements obtained with the photon sieve system are used in an inverse problem framework and the spectral images of a radiating scene with a discrete spectrum are reconstructed from their superimposed and blurred measurements. This technique is of utmost importance at short wavelengths such as extreme ultra-violet (EUV) and x-rays where radiations with discrete spectrum are common. This is because alternative techniques suffer from the strong absorption of materials or manufacturing difficulties at these short wavelengths.

In this thesis, this spectral imaging technique with photon sieves is studied through both numerical and experimental analysis and its performance is evaluated for scenarios of practical importance. Helping to bridge the gap between the theoretical and experimental evaluation of the technique, this study aims to conclusively demonstrate



its performance and practical feasibility.

## 1.1 Contributions and Outline

This work is organized as follows. In Chapter 2, an up-to-date survey of existing spectral imaging techniques is presented along with the terminology and parameters associated with such systems.

In Chapter 3, first, some background about diffractive imaging elements and their mathematical characterization are given. Then in Section 3.2, a fast and accurate method is developed to compute the two-dimensional point spread function (PSF) of any diffractive imaging element. Using this method, imaging properties of photon sieves under different design scenarios are also analyzed. Finally, in Section 3.3, a flexible experimental setup built for the photon sieve imaging system is described, and PSF measurements obtained with this setup are compared with the theoretical PSFs computed using the method developed in Section 3.2.

Chapter 4 focuses on the image reconstruction aspect of the photon sieve spectral imaging technique. First, a detailed explanation of the imaging system, and the corresponding forward and inverse problems are presented in Section 4.1. Then, the image reconstruction algorithm for solving the inverse problem is described in Section 4.2. Lastly, in Section 4.3, results of a comprehensive set of numerical tests are presented to assess the performance of the reconstruction method under different practical scenarios of interest such as for varied number of observations, amount of measurement noise, measurement plane locations and spectral composition of the scene. Also, the performance of different regularization choices are comparatively evaluated.

Finally, Chapter 5 concludes this work by commenting on the contributions of this thesis, the results and their implications, as well as the future work.



## CHAPTER 2

### REVIEW OF SPECTRAL IMAGING TECHNIQUES

#### 2.1 Spectral Imaging

Spectral imaging is the process of capturing the spectrum for each spatial location in a radiating scene. Today, application areas of the spectral imaging techniques are growing rapidly since the spectral image data set provides a useful diagnostic information for a wide variety of applications including agriculture, remote sensing, biomedicine and defense.

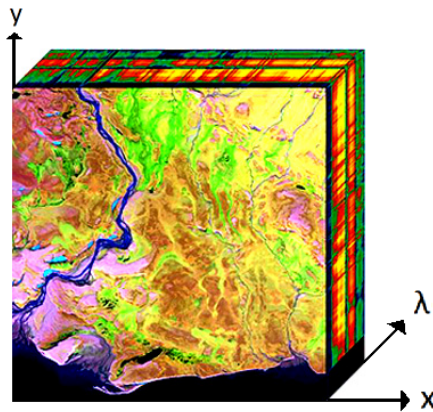


Figure 2.1: A sample spectral image data set. Image retrieved from [1].

Although spectral imagers use detector arrays similar to that of other imaging techniques, spectral imaging devices have more complicated optical systems than the traditional grayscale and red-green-blue (RGB) cameras. While a grayscale imaging device measures the integrated intensity within its detector array's spectral range, an RGB imaging device works similar to its grayscale counterpart but dividing the

spectrum into three overlapping spectral bands. Unlike both, spectral imaging techniques provide the spectrum for each spatial location by dividing it into several non-overlapping narrow bands. This results in forming a 3-D image data set as illustrated in Fig. 2.1.

In this chapter, the terminology used in this thesis will be explained in Section 2.2, the properties and parameters associated with spectral imaging devices will be described in Section 2.3, and the existing spectral imaging techniques will be reviewed in Section 2.4.

## 2.2 Spectral Imaging Terminology

Spectral imaging literature contains different terminologies used by different research groups. To avoid ambiguity, the terminology that is used throughout this document will be defined.

First of all, the name of the field appears in different forms such as hyperspectral imaging, multi-spectral imaging, spectral imaging or imaging spectroscopy. For the sake of simplicity, a device that obtains a 3-D image with more than three spectral bands will be referred to as a spectral imaging system throughout this document. The resulting spectral data set will be mathematically expressed as  $I(x, y, \lambda)$  where  $\lambda$  is the spectral dimension, and  $x$  and  $y$  are the horizontal and vertical spatial dimensions, respectively. Also, a spectral data set will be referred as spectral datacube, with each unit of the datacube called as a "voxel". Spectral datacube and associated voxels are illustrated in Fig. 2.2.

Resolution is another term that may cause ambiguity. Throughout this document, "pixel resolution" is used as the number of measurement elements on the detector along a spatial dimension whereas the terms of "spatial resolution" and "spectral resolution" refer to the ability of imaging system to resolve nearby spatial and spectral components of the scene, respectively.

The terms of "scanning" and "snapshot" are used to refer to the acquisition strategy of the spectral imaging systems. The term "snapshot" is used to describe devices that

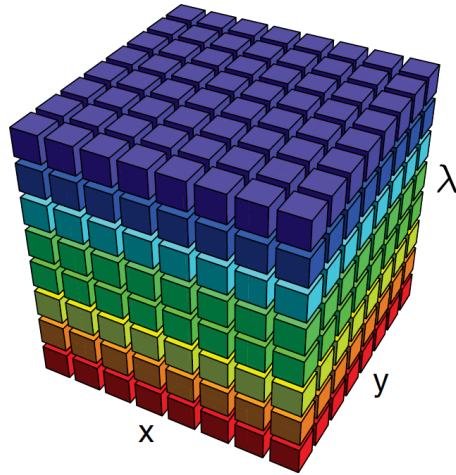


Figure 2.2: A sample spectral datacube where each inner cube represents a voxel. Image retrieved from [2].

construct the spectral datacube using a single exposure interval of detector(s). Note that, the terms "snapshot" and "scanning" do not necessarily give information about the acquisition time of the device.

### 2.3 Spectral Imaging System Parameters

- **Spectral Resolution:** Spectral resolution represents the minimum wavelength difference that is distinguishable by the imaging system. It is related to the resolving power of the system as follows:

$$\Delta\lambda = \frac{\lambda}{\mathbf{R}} \quad (2.1)$$

where  $\Delta\lambda$  denotes the spectral resolution at wavelength  $\lambda$  and  $\mathbf{R}$  is the resolving power of the imaging system [13].

- **Spatial Resolution:** Spatial resolution is the minimum-sized spatial detail distinguishable in an image. It represents the ability of an imaging system to resolve spatial features as illustrated in Fig. 2.3.
- **Pixel Resolution:** Pixel resolution represents the number of voxels along a spatial dimension. A detector array samples the detected continuous input ir-

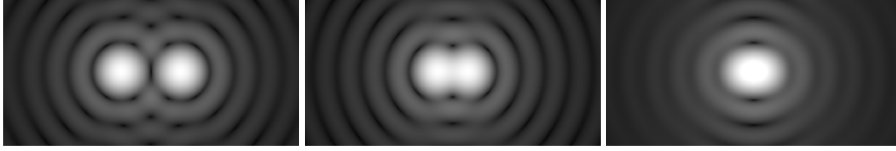


Figure 2.3: Two spatial features become indistinguishable as the spatial spacing between them gets smaller than the spatial resolution of the imaging system. Image retrieved from [3].

radiance over each pixel. Mathematical expression for this sampling process is given in Eqn. 2.2 where  $I[k, l]$  is the sampled image,  $I_c(x, y)$  is the continuous input irradiance, and  $\delta x$  and  $\delta y$  are the pixel widths along  $x$  and  $y$  directions, respectively. Here,  $N_x$  and  $N_y$  denote the pixel resolution along each spatial dimension.

$$I[k, l] = I_c(x, y)|_{x=k\delta x, y=l\delta y} \quad (2.2)$$

where

$$\begin{aligned} -(N_x - 1)/2 &\leq k \leq (N_x - 1)/2, \\ -(N_y - 1)/2 &\leq l \leq (N_y - 1)/2. \end{aligned}$$

- **Total Frame Rate:** Total frame rate is defined in this thesis as the reciprocal of the total acquisition time needed to fully capture the spectral datacube.
- **Number of Spectral Bands:** The number of spectral bands, denoted by  $N_w$ , is the number of narrow-band spectra in the spectral datacube. A sample spectral datacube with  $N_w = 32$  is shown in Fig. 2.4.

## 2.4 Overview of Spectral Imaging Techniques

Research conducted on spectral imaging has led to many different techniques developed for this imaging modality. Architectures addressing a wide variety of different considerations including system cost, time resolution, throughput and manufacturing difficulties resulted in different approaches to tackle the task of forming the 3-D spectral data set. Due to the vast amount of different techniques proposed, a consistent

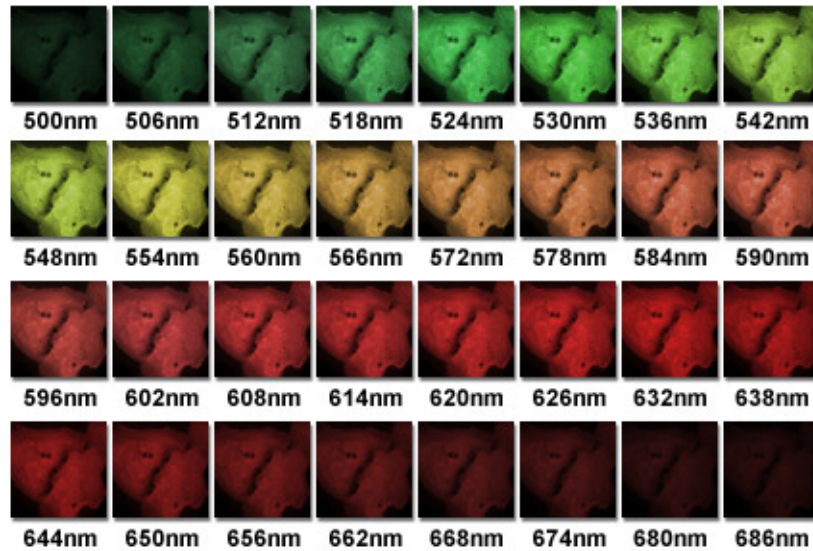


Figure 2.4: A sample spectral datacube with a spectral range of 500nm to 686nm and a spectral resolution of 6nm, hence consisting of a total of 32 spectral bands. Image retrieved from [4].

classification of spectral imaging techniques is necessary. To this end, we propose the classification approach depicted in Fig. 2.5.

## 2.4.1 Optics-based Techniques

Optics-based spectral imaging techniques form the datacube directly from the raw data acquired with the detector array. These techniques optically form the spectral datacube by either scanning, image slicing or dividing where scanning techniques are referred to as conventional techniques in this thesis. Conventional techniques, image slicing and image dividing based techniques are reviewed in Sections 2.4.1.1, 2.4.1.2 and 2.4.1.3, respectively.

### 2.4.1.1 Conventional Techniques

- **Whiskbroom Spectral Imaging**

Whiskbroom spectral imaging performs scanning along both spatial dimensions and uses a 1-D detector array to obtain spectral datacube. The scanning

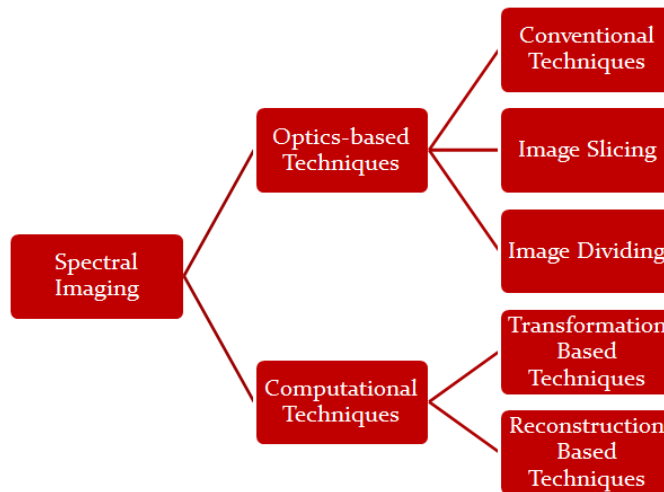


Figure 2.5: Overview of spectral imaging techniques.

is achieved by either mechanically moving the single detector in the measurement plane or by using two galvo mirrors to direct the incident irradiance of different spatial positions onto a fixed detector. The spectrum of each spatial position is obtained dispersing the incoming light from that position onto the linear detector array. An illustration of the whiskbroom approach is shown in Fig. 2.6a.

The whiskbroom approach has advantages such as fast readout rate, wide spectral range, high spectral resolution, and low cost. Conversely, disadvantages associated with this approach are low total frame rate and high hardware complexity [5].

- **Pushbroom Spectral Imaging**

Pushbroom spectral imaging approach performs scanning along one spatial dimension and uses a 2-D detector to capture the 3-D spectral information. For each integration duration of the detector matrix, pushbroom spectral imagers limit the incident scene irradiance by a long slit and then disperses the corresponding 1-D spatial region onto the 2-D detector. This acquisition approach is shown in Fig. 2.6b.

Pushbroom approach is one of the most widely-used approaches for spectral imaging due to its convenience for airborne and spaceborne applications. This class of imagers can be mounted on a moving platform and thus the mechanical-



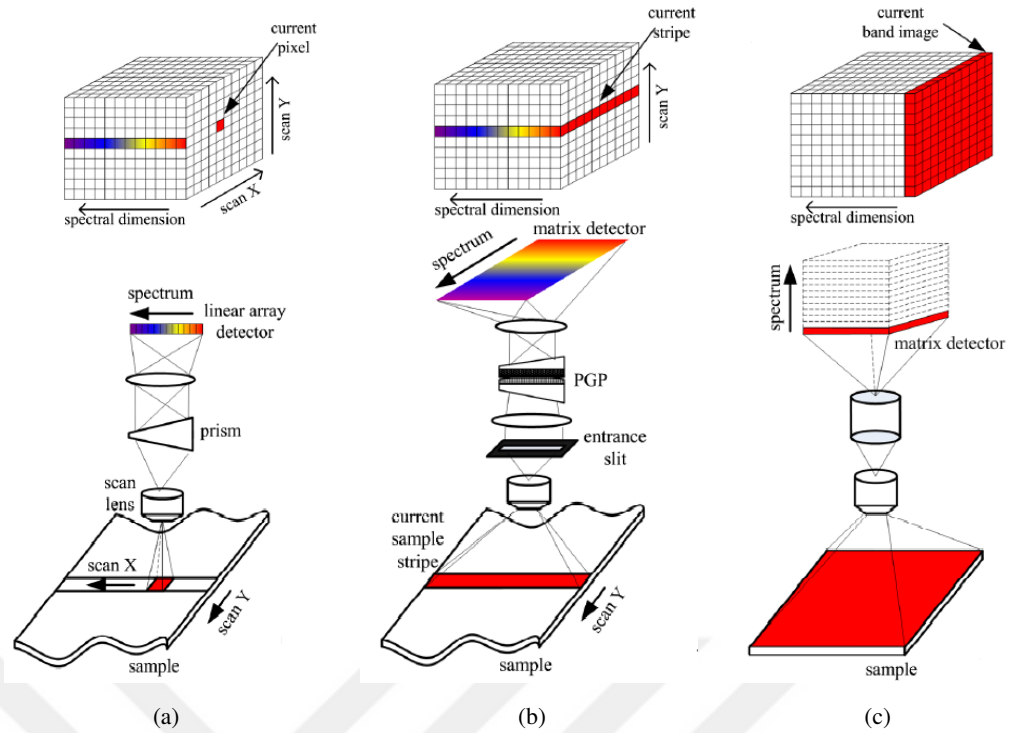


Figure 2.6: (a) Whiskbroom approach. (b) Pushbroom approach. (c) Tunable filter approach. Image retrieved from [5].

optical scanning of the scene can be avoided by using the motion of platform itself. Different than the whiskbroom spectral imagers, this technique provides higher throughput (hence higher signal-to-noise ratio (SNR)) and higher total frame rate while maintaining the high spectral resolution, but with increased calibration difficulty [14].

- **Tunable Filter Spectral Imaging**

This class of spectral imaging devices use multiple narrow-band spectral filters to apply wavelength filtering on the incident light, thus forming a stack of images associated with the spectral bands allowed through each filter. In this approach, the datacube is constructed by repeating the imaging procedure by performing scanning along the spectral dimension with the utilization of different filters.

Spectral imaging using tunable filters provides medium spectral range and spectral resolution with low throughput, high cost and low hardware complexity [5]. In addition, total frame rate depends on the switching duration of the tunable fil-

ter technology used. For example, wavelength switching time for filter wheel, liquid crystal tunable filter (LCTF) and acousto-optical tunable filter (AOTF) are reported to be of order of 1 s, 50 to 500 ms and 10 to 50  $\mu$ s, respectively [2].

#### 2.4.1.2 Image Slicing based Techniques

Main challenge of spectral imaging arises from the fact that the desired data is of three dimensions while the detectors are inherently of two dimensions. Image slicing based techniques approach this difficulty by reformatting the 2-D incident irradiance into 1-D shape by optical means and then dispersing the resulting 1-D data onto a detector.

- **Integral Field Spectral Imaging using Reflection**

This class of spectral imagers use reflective optical elements to reshape the observed 2-D beam before dispersing it onto the detector. First example of this approach is introduced by Bowen in [15] and uses a stack of mirrors to direct vertical lines of the input scene and vertically concatenate them to form a single line.

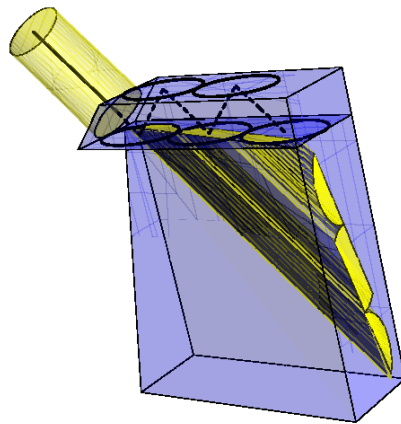


Figure 2.7: Bowen-Walraven image slicer. Image retrieved from [2].

Due to the fact that Bowen's device was large, bulky [16] and hard to manufacture [2], a design by Walraven that relies on the same principle as Bowen's approach is developed [17] in 1972. Walraven's image slicer, more commonly

referred to as Bowen-Walraven image slicer, uses total internal reflection inside a prism to serialize the incident irradiance as depicted in Fig. 2.7. The Bowen-Walraven image slicer is reported to provide high throughput [18] and low spatial resolution [19] with high device cost but it is yet one of the most widely used image slicers [20].

- **Integral Field Spectral Imaging using Fiber Bundles**

Another integral field spectral imaging approach is based on fiber bundles [21]. The idea is to construct a fiber bundle with the shape of the FOV in one end and a linear shape on the other thus effectively serializing the FOV.

Although the initial idea of using fiber bundles as an integral field unit (IFU) was proposed early on 1956 [22], its practical realizations came a lot later because of the manufacturing difficulties associated with fiber-optics technology [23]. Spectral imaging using fiber bundles is reported to have low spatial resolution and be susceptible to noise induced by varying mechanical vibration [24] and devices built on this principle have relatively low pixel resolution of order few tens of voxels in each spatial dimension [25, 26].

- **Integral Field Spectral Imaging using Lenslet Arrays**

Another approach to integral field spectral imaging is to use lenslet arrays. The idea of using lenslet arrays as an IFU to achieve spectral imaging is proposed in 1960 by Courtes [27]. A lenslet array placed in the aperture of the imaging system focuses individual wavefronts incident on each lenslet, and then each of the focused spots are dispersed onto a different position on the 2-D detector. It is reported that spectral imagers with large number of spectral bands such as 400 and 580 bands [28, 29] are realized with this approach.

- **Image Mapping Spectrometry (IMS)**

Integral field spectral imaging is shown to provide the spectral datacube with a single snapshot and high number of spectral bands but with low pixel resolution. On the other hand, IMS approach provides high pixel resolution by using an image slicing methodology similar to that of Bowen's. Introduced in 2009 by Gao et. al. [30], IMS maps each horizontal or vertical line of the incident beam on the input aperture to different spatial locations using an image

mapping mirror with proper spacing. Then, empty space between horizontal or vertical lines are filled by dispersion.

### 2.4.1.3 Image Dividing based Techniques

The main idea in image dividing based optical techniques is to divide the input wavefront into multiple replicas and then individually process these replicas to obtain the datacube. Each of these techniques uses a different optical approach to divide and process the incident radiation from the scene as will be described below.

- **Beamsplitting Spectral Imaging**

In beamsplitting spectral imaging, incident input radiation is divided into several replicas and a different narrow bandpass filter is applied to each replica to obtain a 2-D image of the scene at a particular spectral band. Beamsplitting and filtering can be achieved by using different optical elements such as color splitting prisms [31, 32, 33], spectral filtering beamsplitters [34] and filter stacks [35]. Main advantage of this snapshot spectral imaging approach is its ability to provide high pixel resolution, but it has the drawback of low number of spectral bands which is limited to  $N_w < 6$  [2].

- **Spectrally Resolving Detector Arrays (SRDA)**

Another image dividing based approach relies on spectrally resolving detector arrays. In this approach, the image of the scene is recorded using filters placed on top of each detector, instead of dividing the beam beforehand. Each pair of filter and detector element provides a single voxel of the datacube. Therefore, this approach to spectral imaging can be understood as an extended version of the traditional RGB imagery. The technique is illustrated in Fig. 2.8.

- **Image Replicating Imaging Spectrometer (IRIS)**

Developed in 2002 [36], this technique relies on the use of Wollaston beamsplitting polarizer. A Wollaston beamsplitting polarizer consists of two triangular birefringent prisms glued to each other to divide incident polarized light into two with the angle between splitted beams depending on the wavelength. After

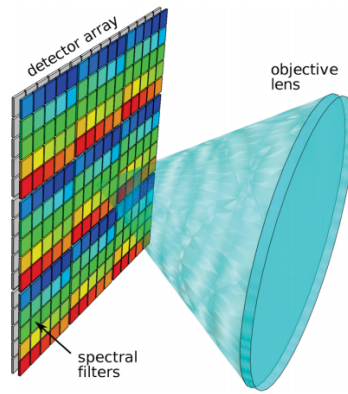


Figure 2.8: Illustration of SRDA approach to spectral imaging. Image retrieved from [2].

splitting the input beam, the device simultaneously applies wavelength filtering to each beam. By using  $N$  Wollaston prisms sequentially, IRIS can form  $2^N$  spectrally filtered replicas of the incident radiation and then optically projects them onto the detector array to form the datacube.

The IRIS system is reported to provide a modest number of spectral bands ( $N_w = 8$  in [37]), modest field of view (FOV) and high SNR [38]. Main disadvantages associated with this technique are its polarization dependent behaviour and the trade-off between FOV width and number of spectral bands.

- **Tunable Echelle Imager (TEI)**

Introduced in 2000 [39], TEI utilizes a Fabry-Pérot filter, an optical device with a periodic bandpass spectral transmission pattern, to apply filtering in the spectral domain. This filtering process leaves only the narrow bands of interest. Then, resulting beam is directed onto the detector array after each wavelength is mapped to a different pixel location.

Practical realization of TEI is shown to provide high spectral resolution [40] but the main disadvantage is its low throughput caused by the use of Fabry-Pérot filter [2].

## 2.4.2 Computational Imaging Techniques

In the computational imaging approaches, transformation or reconstruction is performed on the raw data acquired with the detectors to form the spectral datacube. Here we review such spectral imaging modalities that involve either transformation or reconstruction in Sections 2.4.2.1 and 2.4.2.2 respectively.

### 2.4.2.1 Transformation based Techniques

Transformation based computational imaging techniques perform a transformation on the detector-captured raw data, which simply corresponds to representing the data in a different basis. Interferometric devices belong to this class of spectral imagers and they exploit the fact that the Fourier transform of the interferogram of an incident radiation is equal to its spectrum [41]. Another approach in this class is multi-aperture filtered camera (MAFC) which uses a linear transformation to correct for the off axis data acquisition of multiple detector arrays and thus is classified here as a transformation based approach.

- **Imaging Fourier Transform Spectrometer (IFTS)**

This scanning-based interferometric approach splits the incident radiation into two by using a beamsplitter and then introduces varying optical path difference (OPD) to the splitted beams before combining them on the detector. Amount of OPD introduced to the beams causes a phase shift and the device sequentially collects data for different phase shifts between splitted beams, thus constructing an interferogram. Interferogram is a 3-D data that consists of 2-D interference patterns associated with each phase shift. The spectral datacube is then constructed by computing the Fourier transform of the interferogram.

The IFTS is most commonly used in the far-infrared region, and it is reported to provide a high SNR and large number of spectral bands [13] but with the disadvantage of sensitivity to mechanical vibrations [2].

- **Snapshot Hyperspectral Imaging Fourier Transform Spectrometer (SHIFT)**

SHIFT spectral imager is a snapshot interferometric device developed in 2010 [42].

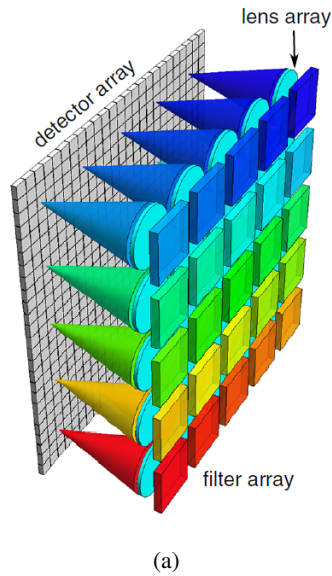


Figure 2.9: An MAFC implementation where each filter - detector array pair is given. Image retrieved from [2].

This spectral imager first forms multiple images of the scene by using a lenslet array. Then a spatially varying optical path difference is introduced to each formed image by using a Wollaston prism. The result is projected onto a detector where replicas of the scene with different OPDs appear to be tiled. The datacube is then constructed from the imaged interferogram.

The main disadvantage of this approach is its low optical throughput caused by the use of polarizers [43] and parallax problem caused by the use of the lenslet array [44]. On the other hand, its advantages are its compactness and insensitivity to mechanical vibrations.

- **Multi-Aperture Filtered Camera (MAFC)**

MAFC approach is a simple, snapshot approach developed in 2004 [45]. In this approach, a filter - detector array pair is used to image the scene at different spectral bands. Given that each optical assembly for each different spectral band is placed close to each other, MAFC approach assumes that individual detector arrays capture the same scene with nearly same angle of incidence. Unwanted parallax effects are then reduced with a computational method. For example, the computational method proposed in [45] applies pixel remapping to the acquired raw data such that parallax induced projection angle of each

pixel is estimated and then compensated. An illustration of this approach is given in Fig. 2.9a.

Advantages of this technique is its simple and compact hardware whereas its main disadvantage is caused by the limiting assumption of near-uniform angle of incidence from the scene for all filter-detector array pairs.

### 2.4.2.2 Reconstruction based Techniques

As a result of the limitations of the optics-based techniques and the advancements in computing power, computational imaging approaches to spectral imaging have emerged. This has led to the development of novel spectral imagers with new capabilities that would not otherwise be possible. In this section, we review reconstruction-based computational spectral imaging approaches which include computed tomography imaging spectrometer, coded aperture snapshot spectral imager and photon sieve spectral imager.

- **Computed Tomography Imaging Spectrometer (CTIS)**

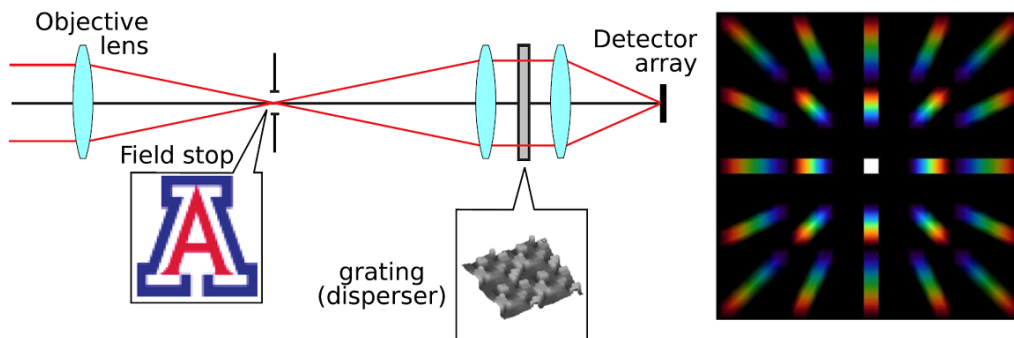


Figure 2.10: Left: Depiction of the Computed Tomography Imaging Spectrometer (CTIS), right: An illustration of 5x5 diffraction pattern on the detector array. Image retrieved from [2].

First proposed in 1991, CTIS is a computational spectral imaging system that reconstructs the datacube from several dispersed images of the scene [46, 47]. In this approach, the radiation from the scene is passed through a 2-D grating



to construct dispersed images at multiple diffraction orders. Each diffraction order corresponds to a different amount of dispersion (chromatic aberration), and each dispersed image corresponds to a 2-D oblique projection of the spectral datacube with a different projection angle. The 3-D datacube is then reconstructed from its projections by using a computational routine inspired from the tomographic reconstruction. A depiction of the CTIS is shown in 2.10 along with a sample set of projections on the detector array for a  $5 \times 5$  diffraction pattern.

There are both snapshot and scanning realizations of the CTIS instrument. As for the scanning case, study in [48] utilizes a rotatable direct vision prism to obtain different projections. In this approach, a sequence of images is captured for each amount of rotation on the prism which corresponds to a different projection angle for the projection of the datacube. The resulting images are then combined with a reconstruction method that solves the underlying linear inverse problem by a simple direct inversion of the sensing matrix. On the other hand, the snapshot realizations of the CTIS instrument use 2-D grating to directly obtain the 2-D projections of the 3-D spectral datacube on the detector. Then, similar to their scanning counterpart, the 3-D datacube is formed by numerical reconstruction. In [46], the reconstruction of the datacube is performed with the multiplicative algebraic reconstruction technique (MART). MART algorithm operates by iteratively minimizing the entropy of the estimate for reconstruction [49]. In another implementation of CTIS in [50], expectation maximization algorithm in [51] is used to obtain the reconstruction by iteratively minimizing the norm of the residual.

One important limitation of the CTIS approach arises from the missing cone problem first pointed out in [50]. The missing cone problem is due to the limited projection angle caused by the use of finite-sized detector arrays and the decreased diffraction efficiency associated with higher diffraction orders. Based on the projection-slice theorem [52], the problem can be viewed as the absence of data for the conic regions in both upper and lower portions of the frequency domain representation of the datacube.

There are advantages and disadvantages associated with the CTIS approach.

Compactness of the system, not requiring mechanically moving parts and availability of the snapshot form are the advantages. On the other hand, the disadvantages include manufacturing difficulties associated with the 2-D dispersing element, reconstruction artifacts arising from the missing cone problem, and the high computational complexity of the reconstruction scheme.

- **Coded Aperture Snapshot Spectral Imager (CASSI)**

CASSI is a computational imaging instrument that takes advantage of the compressive sensing (CS) theory for snapshot spectral imaging [53]. It involves an optical system similar to CTIS; but, here a single projection of the spectral datacube is obtained after applying a coded aperture to the imaged scene. As a result, the captured data corresponds to the projection of the spatially coded datacube, which contains both spatial and spectral information in a multiplexed fashion. The known binary aperture mask allows the measurement to be decomposed into its spectral components and the absent spatial data corresponding to the blocking regions of the coded aperture is reconstructed under the assumption that an accurate sparse representation of the datacube is available. An illustration of the single disperser version of the CASSI instrument is shown in Fig. 2.11.

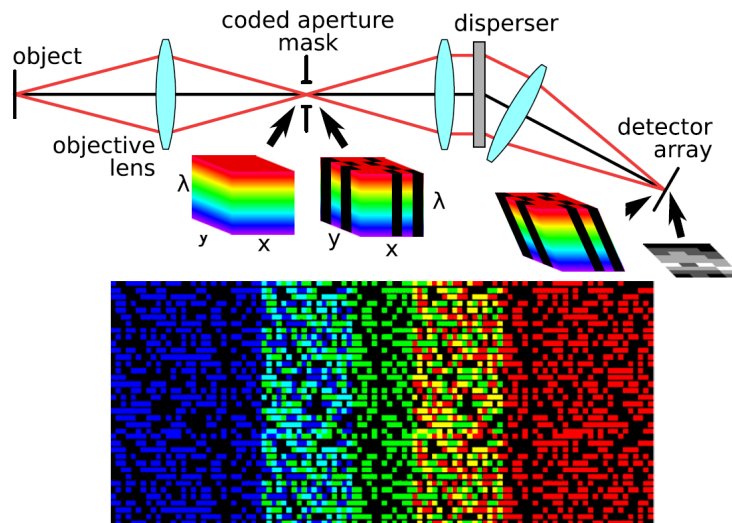


Figure 2.11: Illustration of coded aperture snapshot spectral imager. Image retrieved from [2].

CASSI differs from the previously developed coded aperture spectral imaging techniques [54, 55, 56] by its snapshot ability. There are several variants of the CASSI approach for snapshot spectral imaging. The first realization of the CASSI approach is DD-CASSI [57]. Developed in 2007, this technique involves a dual-disperser architecture where the input scene is dispersed twice with the coded aperture lying between the two dispersers and the second dispersion cancelling the effect of the first one. Then, the resulting wave is directed to the detector that captures superimposed 2-D spatial information for each spectral band of datacube. Yet, since a space-shifted binary code is applied to each 2-D spatial information component, the reconstruction of the datacube is still possible. On the other hand, different than the DD-CASSI, SD-CASSI uses a single disperser for multiplexing the spatial and spectral information. Capturing the spectral data in a less compressed manner, SD-CASSI offers images with higher spectral and lower spatial resolution compared to DD-CASSI.

The reconstruction method employed in CASSI is a compressive sensing approach that assumes a sparse representation for the datacube. This reconstruction method aims to undo the effects of the underlying optics, coded aperture and dispersion by minimizing a data fidelity term with  $\ell_1$  norm regularization that imposes sparsity in some transform domain. This minimization problem is given as follows for the SD-CASSI:

$$\hat{f} = \mathbf{W} \left( \underset{\theta'}{\operatorname{argmin}} \{ \|g - \mathbf{H}\mathbf{W}\theta'\|_2^2 + \tau \|\theta'\|_1 \} \right) \quad (2.3)$$

where  $\hat{f}$ ,  $\mathbf{W}$ ,  $\mathbf{H}$ ,  $\tau$  and  $\theta'$  are respectively the solution, sparsifying transformation operator, sensing matrix of the system, regularization parameter and sparse transform coefficients. The above problem enforces the minimization of the residual between the model and the measured data along with the sparsity of the transform coefficients for the solution. The sparsifying transform matrix,  $\mathbf{W}$ , used is the Kronecker product of 2-D Symmlet-8 wavelet basis with the cosine basis.

Although CASSI is a novel spectral imaging system that introduces a new and exciting approach to the field, the practical performance of the CASSI instrument are not as good as expected [2]. Its compact architecture, simple optical

assembly and large datacube size are advantageous. Yet, the reconstruction method that is reported to have an algorithm complexity of  $O(KN^4L)$  for  $K$  focal-plane array (FPA) measurements and a datacube size of  $N \times N \times L$  yields a considerably long acquisition time despite the snapshot architecture of the instrument. Furthermore, the CASSI approach is reported to provide good reconstruction results only for the non-snapshot case [58].

- **Photon Sieve Spectral Imager**

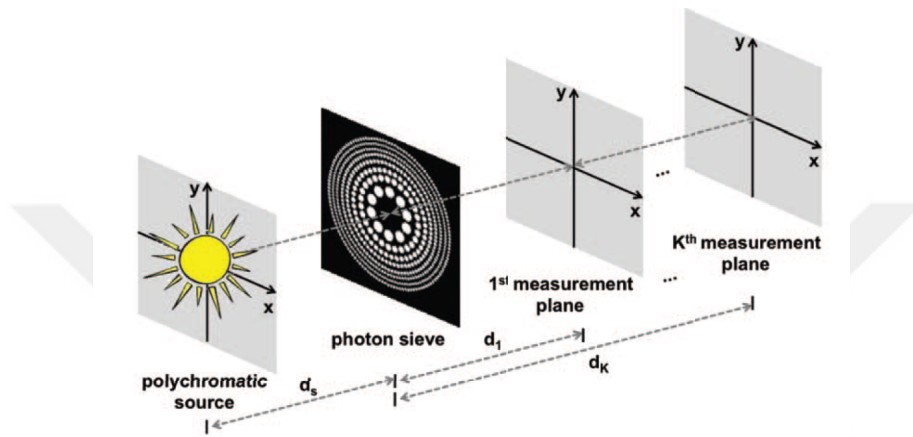


Figure 2.12: Illustration of photon sieve based spectral imaging approach. Image retrieved from [6]. © 2014 IEEE.

This reconstruction based computational spectral imaging technique relies on the use of a diffractive imaging element called photon sieve [59, 6]. Photon sieve is a modification of a Fresnel zone plate, both of which are diffractive lenses that provide wavelength dependent focusing. In other words, these optical elements focus spectral components of different wavelengths to different focal planes. For traditional imaging, this behavior causes an undesired effect called chromatic aberration which implies the presence of a different system response for each spectral component. This traditionally undesired behavior is exploited in this approach for spectral imaging.

This spectral imaging technique is primarily developed for high-resolution imaging of scenes with discrete spectrum. It works by distributing the image formation task between a photon sieve system and a reconstruction method. The photon sieve system, as illustrated in Fig. 2.12, takes multiple measurements with each measurement consisting of focused or defocused images of different

spectral components. For instance,  $K$  measurements can be obtained for  $K$  different spectral components, with each measurement taken on the corresponding center wavelength's focus. Then, by using a reconstruction method, the individual spectral images are reconstructed from their superimposed and blurred measurements. In other words, for each measurement, this method eliminates the contributions from all other unwanted bands.

Photon sieve based spectral imaging approach is reported to offer higher spectral resolution than the conventional tunable filter spectral imaging techniques and enable diffraction-limited high spatial resolution, while requiring only a light-weight and low-cost imaging system [60, 6, 61]. This technique is of utmost importance at short wavelengths such as extreme ultra-violet (EUV) and x-rays where radiations with discrete spectrum are common. This is because alternative spectral imaging techniques suffer from strong absorption of materials or manufacturing difficulties at these short wavelengths.

This spectral imaging technique is the main focus of this study. We will demonstrate the performance of the technique for various scenarios of practical importance through both numerical and experimental analysis.



## CHAPTER 3

# POINT-SPREAD FUNCTIONS OF DIFFRACTIVE IMAGING ELEMENTS

### 3.1 Diffractive Imaging

There are several ways to model the behavior of electromagnetic waves as they propagate through space. Geometrical optics attempt to characterize electromagnetic waves by treating them as rays where rays can be interpreted as bundles of massless particles that move through space with highly correlated physical motion patterns. Such motion patterns can be understood and predicted by utilizing geometrical identities. For instance, the law of reflection and the law of refraction in geometrical optics aim to model the behavior of light as it encounters reflective surfaces and transitions between materials of different refractive indices. Although modelling light as rays yields accurate results when the size of the structures that the light encounters is large compared to the wavelength, wave behavior of light should be considered in all other cases. One of such cases that require wave interpretation of light is diffraction. In its simplest form, diffraction is defined as any deviation from geometrical optics when a light wavefront confronts an obstruction [62].

According to a more precise definition, diffraction is the behavior of light to bend around corners of obstacles [63]. It can be understood through the Huygens' principle which states that each point on a wavefront can be interpreted as a source of a spherical radiation [64]. One way to illustrate the diffraction phenomena is through the single-slit experiment depicted in Fig. 3.1. In the single-slit experiment, a plane wave is blocked everywhere except the slit on the slit plane. However, as the wave

propagates from the slit plane, it does not remain limited to the width of the slit but does also propagate towards regions that are blocked by the slit, following a spherical distribution, as stated by the Huygens' principle.

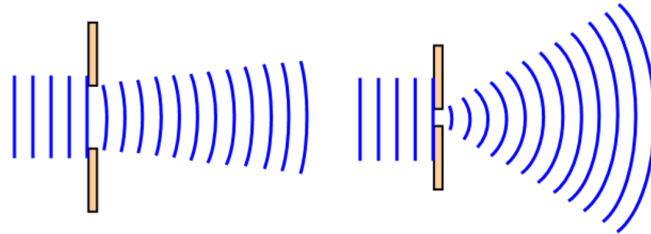


Figure 3.1: Single-slit experiment that illustrates the diffraction phenomena for a wider and a narrower slit.

Many optical imaging elements such as lenses and mirrors exploit the refraction and reflection phenomena to focus light. Although such imaging elements are commonly used in the visible portion of the electromagnetic spectrum, they can turn out to be impractical at shorter wavelengths such as extreme-ultraviolet (EUV) and x-rays. This is because for reflective imaging elements, manufacturing inaccuracies significantly degrade the imaging performance and hinder from achieving diffraction-limited spatial resolution. Similarly, at these shorter wavelengths, a significant refraction cannot be obtained to make refractive imaging elements due to the strong absorption of materials [65]. On the other hand, diffractive imaging elements can still offer diffraction-limited imaging performance even at these shorter wavelengths. In this chapter, point-spread functions of diffractive imaging elements will be investigated using both theoretical, numerical, and experimental tools.

### 3.1.1 Fresnel Zone Plate

Fresnel zone plates (FZPs) are most commonly used diffractive imaging elements. The binary Fresnel zone plate consists of alternating opaque and transparent zones as illustrated in Fig. 3.2a. The transparent zones are placed such that only the constructive interference is allowed at the focus of a certain wavelength. It is important to note here that the focal length of a Fresnel lens depends on wavelength.



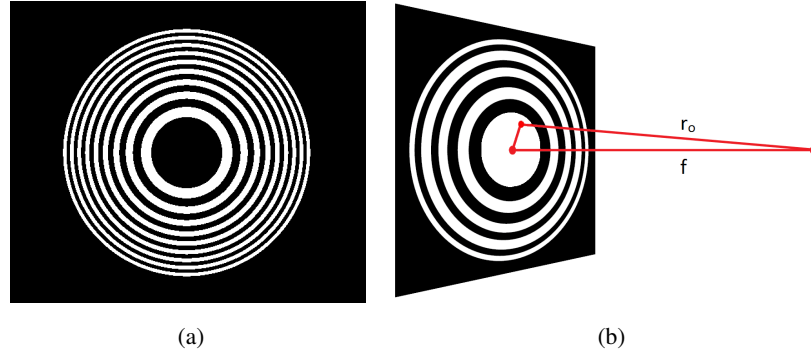


Figure 3.2: (a) Aperture transmission (transmittance) function of a Fresnel zone plate with 9 transparent zones as shown with white rings. (b) A Fresnel zone plate shown along with its focus at a distance of  $f$ .

To arrange transparent zones to constructively interfere at the focus, the optical path length from the focus to a transparent point on the FZP for a specific wavelength, for example  $r_0$ , should not differ more than  $\lambda/2$ . Let us define the first zone of a binary FZP as follows:

$$A_1(x, y) = \begin{cases} 1 & \text{if } \sqrt{x^2 + y^2 + f^2} - f < \lambda/2 \\ 0 & \text{otherwise.} \end{cases}$$

where  $f$  denotes the focal length at wavelength  $\lambda$ . Similarly, the  $n^{\text{th}}$  zone of the FZP, corresponding to a path length difference between  $(n - 1)\lambda/2$  and  $n\lambda/2$  with the focus, can be written as

$$A_n(x, y) = \begin{cases} 1 & \text{if } \frac{(n - 1)\lambda}{2} < \sqrt{x^2 + y^2 + f^2} - f < \frac{n\lambda}{2} \text{ for positive integer } n \\ 0 & \text{otherwise.} \end{cases}$$

The complete aperture transmission function of the FZP can be obtained by combining all the zones with positive constructive interference which only include either even-numbered or odd-numbered zones. Hence the aperture transmission function of the binary FZP can be mathematically expressed as

$$A(x, y) = \sum_{n=1}^{\infty} A_{2n}(x, y)$$

or

$$A(x, y) = \sum_{n=1}^{\infty} A_{2n-1}(x, y).$$

The Fresnel zone plates shown in Figures 3.2a and 3.2b respectively illustrates these two aperture functions. Note also that the above sum is to infinity. A practical zone plate however, includes a finite number of transparent zones which then determines the width of the outermost zone and consequently the spatial resolution.

### 3.1.2 Photon Sieves

A photon sieve is a modification of a Fresnel zone plate which consists of a large number of holes distributed over Fresnel zones. It has been proposed as a superior diffractive imaging device than the Fresnel zone plate [66], to be especially used at UV and x-ray wavelengths to achieve diffraction-limited resolution. Advantages over Fresnel zone plates are improved spatial resolution for a given smallest fabricable structure, suppression of higher diffraction orders through quasi-random variations in the distribution and diameter of the holes, and self-supporting structure [66]. An exemplary photon sieve aperture is shown in Fig. 3.3b along with the Fresnel zone plate of similar properties in Fig. 3.3a.

Photon sieves open up new possibilities for high resolution imaging and spectroscopy. Many such photon sieve imaging systems are developed, some of which are also built and tested to illustrate diffraction-limited imaging performance [6, 60, 67, 68, 69].

## 3.2 Fast PSF Computation Method for Diffractive Imaging

Here, a fast and accurate method is developed for the numerical computation of two-dimensional point-spread functions (PSFs) of photon sieves. This method is based on the closed-form Fresnel imaging formulas and PSFs derived in [70], which are

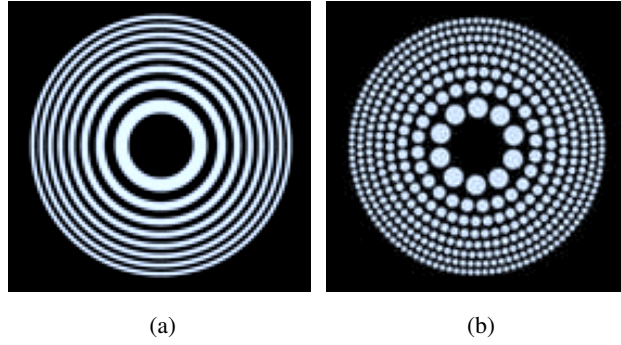


Figure 3.3: (a) Aperture function of a Fresnel zone plate. (b) Aperture function of a photon sieve that is formed by replacing Fresnel zones in (a) with pinholes.

given in terms of convolutions and Fourier transforms. Here, this form is exploited to develop a fast computation method for the 2-D PSF by using fast Fourier transform (FFT). This fast computation method is important for effectively developing and analyzing new imaging modalities enabled by photon sieves.

In the earlier works, the focusing properties of photon sieves and the design procedure have been analyzed through the calculation of Fresnel-Kirchoff diffraction integrals [66] and approximate Fresnel integrals [71]. The PSF computation based on [71] is only for photon sieves with circular-shaped holes, and also requires numerical integration and evaluation of Bessel functions for each individual hole. The computation method presented here instead utilizes FFT and makes use of the 2D aperture function of the photon sieve at once. Furthermore, unlike [71], our method is general enough that it can be used for any photon sieve configuration, not necessarily for those with circular holes. In fact, the developed method is powerful that it can be used to effectively analyze any other diffractive imaging element, such as Fresnel lenses and their modifications, and any other mask-like patterns including coded apertures.

Developed two-dimensional PSF computation method is presented in Sect. 3.2.3 along with the evaluation of its accuracy and computational cost in Sect. 3.2.4. In addition, to illustrate its use, numerical simulations are performed to analyze the imaging properties of the photon sieves under different design scenarios and results are presented in Sect. 3.2.5. This work has been recently presented in [7].

### 3.2.1 Point-Spread Function (PSF)

Point-spread function (PSF) is the response of an optical system to a unit point source [72]. Similar to its one-dimensional analogous, the impulse response, the point spread function completely characterizes an optical system that satisfies space-invariance and linearity properties. Because of this, it is an important tool for analyzing such optical systems.

In contrast to an intuitive approach derived from the geometrical optics, a point source input to an optical imaging system with a finite-sized aperture does not produce a point-like output. This is due to the fact that the finite-sized aperture introduces diffraction and “spreads” the energy of input point source to a larger spatial extent. For instance, optical systems that are referred as “diffraction-limited” are the optical systems whose PSFs only include the effect of the unavoidable diffraction caused by the finite-sized aperture and thus can be considered desirable.

Like the impulse response, the PSF can be used to determine the output of a linear space-invariant (LSI) optical system to an arbitrary input by utilizing the superposition principle. The superposition principle in this context corresponds to a 2-D convolution operation and is mathematically expressed in the continuous case as follows:

$$o(x, y) = i(x, y) * g(x, y) = \iint i(u, v)g(x - u, y - v)dudv \quad (3.1)$$

where  $*$  denotes 2-D convolution and 2-D functions  $o$ ,  $i$  and  $g$  are the output, input and PSF of the optical system, respectively. Also note that the optical transfer function, optical system analogous of the transfer function, is the Fourier transform of the PSF.

### 3.2.2 Closed-Form PSF Formula

The aperture (transmission) function,  $a(x, y)$ , of the photon sieve is defined as the ratio of the transmitted field amplitude to the incident field amplitude at every point  $(x, y)$  on the photon sieve. Although, for a photon sieve or in general for a coded aperture,  $a(x, y)$  is commonly binary (taking value 1 over the transparent regions),

$a(x, y)$  is treated as any complex function here to keep the developed method general and applicable to other diffractive imaging elements as well.

For example, for the classical photon sieve configuration consisting of large number of circular holes, the aperture function can be expressed as

$$a(x, y) = \sum_{n=1}^N a_n(x, y) = \sum_{n=1}^N \text{circ} \left( \frac{x - x_n}{d_n}, \frac{y - y_n}{d_n} \right) \quad (3.2)$$

where  $N$  is the total number of holes, and  $a_n(x, y)$  is the aperture function of the  $n^{\text{th}}$  pinhole whose diameter is denoted by  $d_n$  and central location by  $(x_n, y_n)$ . The aperture function  $a_n(x, y)$ , taking value 1 inside the circular pinhole, is expressed in terms of a circle function where the circle function defined as [52]

$$\text{circ}(x, y) = \begin{cases} 1 & \text{if } \sqrt{x^2 + y^2} \leq \frac{1}{2} \\ 0 & \text{otherwise.} \end{cases}$$

Note that the effect of apodization can also be included to  $a(x, y)$  through multiplication with the apodization function.

The PSF of a photon sieve imaging system with aperture function  $a(x, y)$  has the following closed-form expression [70]:

$$g_{\lambda, d_i}(x, y) = j \frac{\lambda}{\Delta} e^{-j\pi \frac{x^2 + y^2}{\Delta \lambda d_i^2}} * A \left( \frac{x}{\lambda d_i}, \frac{y}{\lambda d_i} \right) \quad (3.3)$$

where  $*$  denotes 2-D convolution,  $A(f_x, f_y)$  is the 2-D Fourier transform of  $a(x, y)$ ,  $\Delta = 1/d_i + 1/d_s$  with  $d_s$  and  $d_i$  respectively denoting the distances from the source and image planes to the plane where the photon sieve resides.

### 3.2.3 Developed Fast PSF Computation Method

Because the computation will be performed on a digital computer, the goal here is to compute the samples of PSF  $g_{\lambda, d_i}(x, y)$ . Suppose the separation between the samples are chosen as  $\delta x$  and the total number of samples as  $N$ . Then the PSF computation

will cover the range of  $x$  and  $y$  values from  $[-(N-1)\delta x/2, (N-1)\delta x/2]$ . Here  $N$  is taken to be odd without loss of generality.

The PSF formula in (3.3) is given in terms of a convolution. This form is exploited to develop the fast PSF computation method using FFT since the computational complexity of FFT is much less compared to that of convolution. Proposed method computes the discrete PSF by first sampling the optical transfer function (OTF) in the frequency domain and then performing an inverse FFT. The OTF of the photon sieve, i.e. the 2-D Fourier transform of the PSF, is given by

$$G_{\lambda, d_i}(f_x, f_y) = (\lambda d_i)^4 a(\lambda d_i f_x, \lambda d_i f_y) e^{j\pi(\Delta \lambda d_i^2)(f_x^2 + f_y^2)} \quad (3.4)$$

This OTF is discretized by taking its samples uniformly with a separation of  $1/(N\delta x)$ :

$$G_{\lambda, d_i}[k, l] = G_{\lambda, d_i}(f_x, f_y) \Big|_{f_x = \frac{k}{N\delta x}, f_y = \frac{l}{N\delta x}} \quad (3.5)$$

for  $-(N-1)/2 \leq k, l \leq (N-1)/2$ . Note that the OTF in (3.4) has a finite support determined by the scaled aperture function  $a(\lambda d_i f_x, \lambda d_i f_y)$ . In particular, if the finite size of the aperture is  $D$  along both spatial directions, OTF is nonzero only for a frequency band of length  $D/(\lambda d_i)$  along both spatial frequencies. As a result of this, OTF needs to be sampled only for a finite range of  $k$  and  $l$ .

Related to the finite support of the OTF, or equivalently the bandlimitedness of the PSF, there is also an important constraint on  $\delta x$  dictated by the Nyquist-Shannon sampling theorem:

$$\delta x < 1/(D/(\lambda d_i)) = \lambda d_i/D. \quad (3.6)$$

Hence for the computation method to work accurately, this sampling criterion must be satisfied.

Another issue that should be handled carefully is the selection of the number of samples. Because the PSF is not space-limited and sampling the OTF in the frequency-domain as in (3.5) causes periodic replication of the PSF in the space-domain, the number of samples  $N$  should be chosen sufficiently large to contain a significant amount of total energy of the PSF so that the error introduced by periodic replication is negligible. Provided that the sampling criterion is satisfied and  $N$  is sufficiently

large, the discretized PSF,  $g_{\lambda,d_i}[m, n] = g_{\lambda,d_i}(m\delta x, n\delta x)$  can be obtained by computing the inverse discrete Fourier transform (DFT) of  $G_{\lambda,d_i}[k, l]$ :

$$g_{\lambda,d_i}[m, n] \approx \mathcal{F}_{N \times N}^{-1}\{\mathbf{G}_{\lambda,d_i}[k, l]\}[m, n], \quad (3.7)$$

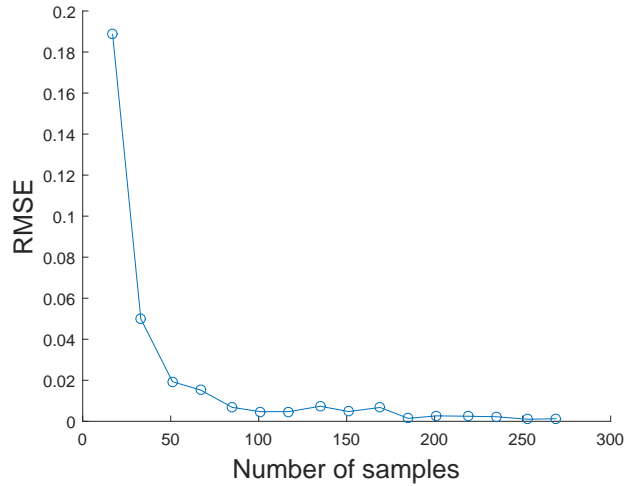
where  $\mathcal{F}_{N \times N}^{-1}$  denotes the N-point inverse FFT. This gives us the 2-D discretized PSF obtained through a single FFT.

### 3.2.4 Computational Efficiency and Accuracy of Method

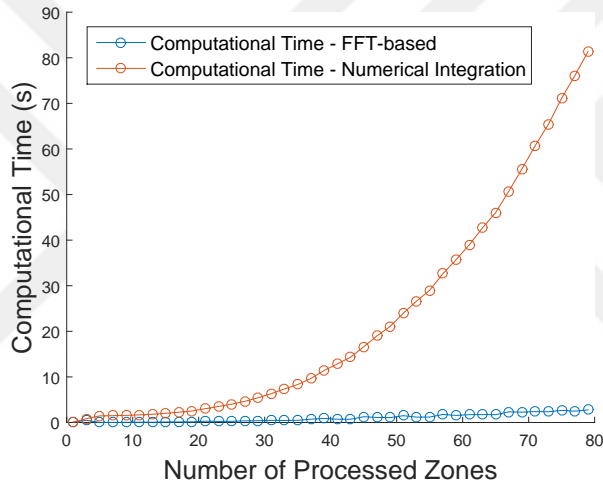
For further analysis, the accuracy and computational efficiency of the developed fast method is compared to that of numerical integration based method in [71]. Fig.3.4a shows the root-mean-square error (RMSE) between the PSFs computed with the two methods as the number of samples,  $N$ , used in the fast method is increased. As mentioned,  $N$  should be chosen sufficiently large to contain a significant portion of the total energy of the PSF in the support of its discretized version. As a result of this, the accuracy of the computation method is improved as we increase  $N$  up to the point that nearly %99.9 of the total energy is contained in the discretized range. However, note that further increase in  $N$  is not needed after this point. Fig.3.4b also shows the computation time needed for each method as the number of zones in the photon sieve is increased. This illustrates the computational efficiency of the developed method. Note that since the PSF computation method in [71] computes the contribution from each individual hole separately, its computation time has strong dependence to the number of holes (or, equivalently, the number of zones). In these simulations, a photon sieve design for EUV solar imaging [60] is used, which contains 125 zones with 64,509 holes, an outer diameter of 50 mm and smallest hole diameter of 50  $\mu\text{m}$ .

### 3.2.5 Numerical Simulations for Photon Sieves

To illustrate the use of the fast PSF computation method, numerical simulations are performed to analyze the imaging properties of the photon sieves under different de-



(a)



(b)

Figure 3.4: (a) RMSE between the PSFs obtained with the two methods for increasing number of samples used in the fast method. (b) Computation time versus number of processed zones for the two methods [7].

sign scenarios involving different shapes of holes and random variations in the hole distributions.

To illustrate that the method is applicable to any diffractive imaging device with given aperture function, two identical photon sieve designs are considered: One with circular holes and the other with square holes. Fig. 3.5(a)-(b) shows the corresponding 2-D PSFs and their 1D cross-sections. As shown, the resulting PSFs are very similar;



only the one with square holes has slightly larger secondary sidelobes.

The effectiveness of different design approaches can also efficiently be analyzed by computing the corresponding 2-D PSFs with the presented fast method. Here this is illustrated by analyzing how the focusing performance of photon sieves are affected from random variations in their hole distributions. It has been proposed that quasi-random spatial distribution of pinholes can help to suppress secondary maxima [66]. Here, the effects of randomizing the existence of pinholes is analyzed and the peak-to-sidelobe-ratio (PSLR) of the PSF is calculated for varying hole existence probabilities (Hole existence probability of 0.5 means that each hole in the original design will exist in the final design with a probability of 0.5). Fig.3.5(c) suggests that the suppression of the secondary maxima is not improved with such randomization.

### **3.3 Experimental Validation of Theoretical PSFs**

The aim of the experimental work of this thesis is to validate the theoretical PSFs of photon sieves. For this aim, an experimental setup is constructed. Traditional experimental approaches to analyze diffractive imaging elements rely on lithographic techniques to physically construct the diffractive device. However, there are two main disadvantages associated with such approaches. Firstly, lithographic fabrication is a costly and time-consuming process. Secondly, a diffractive element constructed using lithographic techniques cannot be changed after fabrication. To overcome these difficulties, a programmable digital micro-mirror device (DMD) is utilized in this experimental setup to construct photon sieves. In this section, the details of this experimental setup will be presented in Section 3.3.1 and the experimental results will be presented in Section 3.3.2.

#### **3.3.1 Experimental Setup**

To justify the design choices for the experimental setup, each component will be described in this section. The experimental setup consists of four main parts: Source, source modifying optics, DMD and charge-coupled device (CCD) camera. An image of the experimental setup is shown in Fig. 3.6.

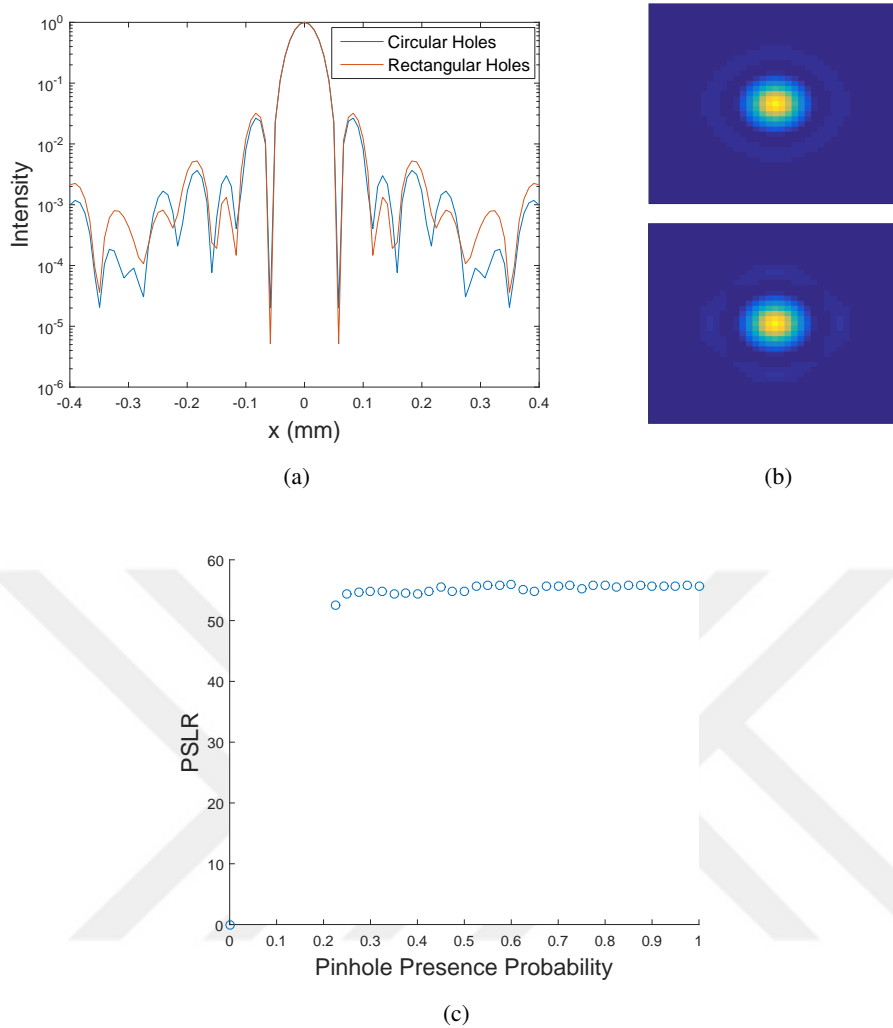


Figure 3.5: (a) Cross-sections of 2-D PSFs for photon sieves with circular and square holes. (b) From top to bottom, the corresponding 2-D PSFs. (c) PSLR of the PSF versus pinhole existence probability [7].

- Source:** Given that the aim of the experimental study is to measure the PSF of a photon sieve, a collimated monochromatic laser source with a narrow spectral band-pass is used. More specifically, the used light source is LLL-2 He-Ne laser of Lambda Scientific with wavelength of 632.8 nm, beam diameter of 1.2 mm and rated output power of 1.0 to 1.5 mW.
- Source Modifying Optics:** The point-spread function is the response of an optical system to a point source as described in Section 3.2.1. In this experimental setup, a collimated laser beam which acts as a point source at infinity, is

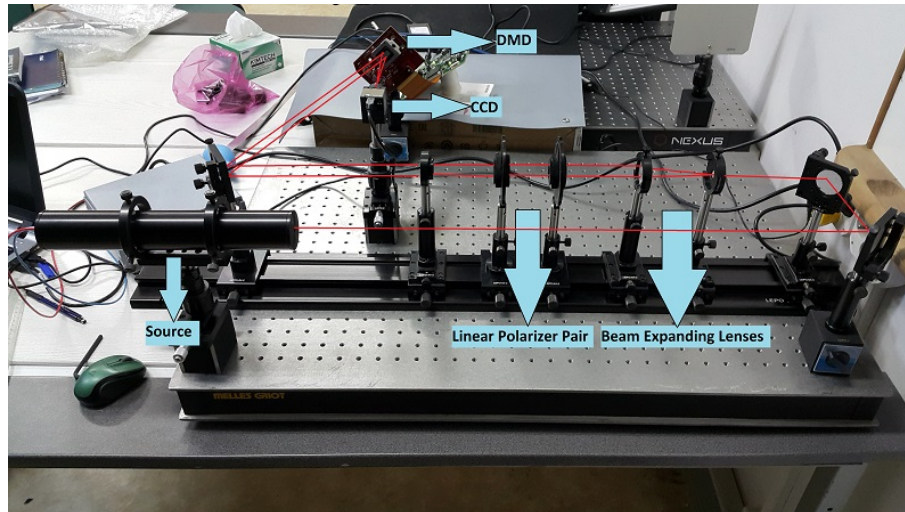


Figure 3.6: A view of the experimental setup where the optical path is depicted with a red line.

used to measure the PSF. As a result, the image of the point source at infinity is captured by the CCD camera as the PSF of the imaging system. Yet, there are practical difficulties associated with this PSF measurement caused by the source beam diameter and output power.

To overcome these practical difficulties and increase the versatility of the system, a set of source-modifying optics is used. The first difficulty addressed arises from the input beam diameter. Without source-modifying optics, the largest diameter of the analyzed diffractive imaging element is limited by the beam diameter of the collimated source, which has a beam diameter of 1.2 mm. On the other hand, the DMD, which is used for generating the pattern of the diffractive imaging element, has an active area of 14.5 mm by 8.2 mm. To be able to effectively use the active area of the DMD, a pair of beam expanding lenses is used.

The second practical difficulty faced when constructing the experimental setup is the input source power. Despite the laser source being used has a relatively low power output, the measured intensity at the focus of some tested diffractive imaging devices is high enough to saturate the pixels of the CCD camera and cause blooming. Moreover, to be able to measure the PSF for the out-of-focus case along with the focused case for the same imaging element, ability of dy-

ynamically adjusting the source power is necessary since the peak intensity for these cases can vary significantly. For these reasons, the experimental setup contains a pair of linear polarizers. By keeping the degree of polarization of one of the linear polarizers fixed, the source power can be adjusted to fit the experiment by varying the degree of polarization of the other polarizer. By using this approach, the experimental setup is able to provide well-adjusted PSFs that fits the dynamic range of the CCD camera.

- **Digital Micro-mirror Device (DMD):** A DMD is a reflective spatial light modulator that modulates the amplitude, direction, and phase of incoming light. It consists of micro-mirrors whose tilt directions can be controlled individually. In this experimental setup, DLP6500 device of Texas Instruments is used to realize the diffractive imaging elements.

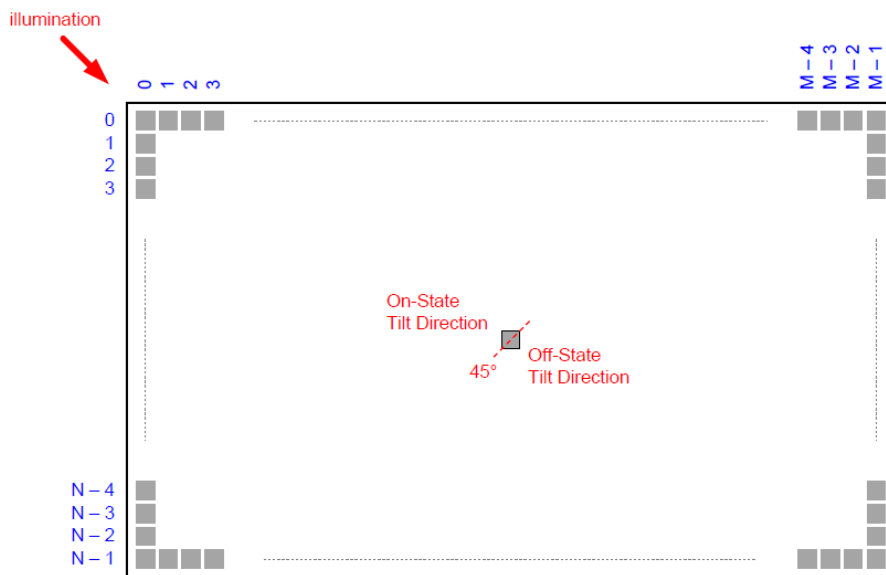


Figure 3.7: A depiction of the DMD chip with  $M \times N$  micro-mirrors. The tilt direction of micro-mirrors is 45 degrees as shown. Image retrieved from [8].

The utilized DMD chip contains more than 2 million micro-mirrors that are placed orthogonally to form a 2-D array of dimensions 1920 by 1080 with a pixel pitch of  $7.56 \mu\text{m}$ . The discrete tilt angles for each micro-mirror are  $\pm 12$  and 0 degrees, corresponding to on, off and neutral states, respectively. The tilt direction for each micro-mirror is perpendicular to its diagonal. A depiction of

the DMD chip is shown in Fig. 3.7.

There are several points that should be considered when using DMDs. Firstly, the DMD surface should be illuminated with an angle of incidence of  $-24^\circ$  as illustrated in Fig. 3.8. This is due to the fact that the on state tilt of each micro-mirror has a magnitude of 12 degrees. Hence, for the detector aperture to be co-axial with the on-state output aperture of DMD, the angle of incidence of the illumination source should be  $-24^\circ$ .

Secondly, because of its pixelated structure, the DMD behaves like a 2-D grating and produces several diffraction orders when illuminated with coherent sources [9]. Careful alignment of the DMD chip considering the angle of incidence of the input beam and the location of the DMD output aperture can lead to a properly aligned system where most of the energy is contained within the  $0^{th}$  order. Such a state leads to the "blaze" condition. If instead the illumination source is not properly aligned, the energy is distributed among the four brightest orders resulting in an "anti-blaze" condition and decreased throughput. In Fig. 3.9a, theoretical diffraction orders for blaze and anti-blaze conditions are depicted along with their experimental verifications in 3.9b and 3.9c, respectively.

- **CCD Camera:** In this experimental setup, DCU223M CCD camera by Thor-Labs is used. There are advantages associated with CCD cameras compared to complementary metal-oxide-semiconductor (CMOS) cameras. Firstly, high uniformity enabled by the use of same charge-to-voltage converter for each pixel leads to reduced fixed-pattern noise for the CCD. Secondly, its higher quantum efficiency allows improved SNR. On the other hand, the blooming effect associated to the CCD technology is a disadvantage. To overcome this disadvantage, a careful adjustment of the input power per unit area is required. The pixel size and dynamic range of the utilized camera are also important. Pixel size affects the spatial resolution of the device and should be small enough to resolve the details of the PSF. The dynamic range is also important when measuring the PSF of a photon sieve since the PSF has a high peak-to-sidelobe ratio for practical designs. In fact, capturing a detailed PSF with sidelobes and an unsaturated main lobe requires a high dynamic range. For our purposes, a dy-

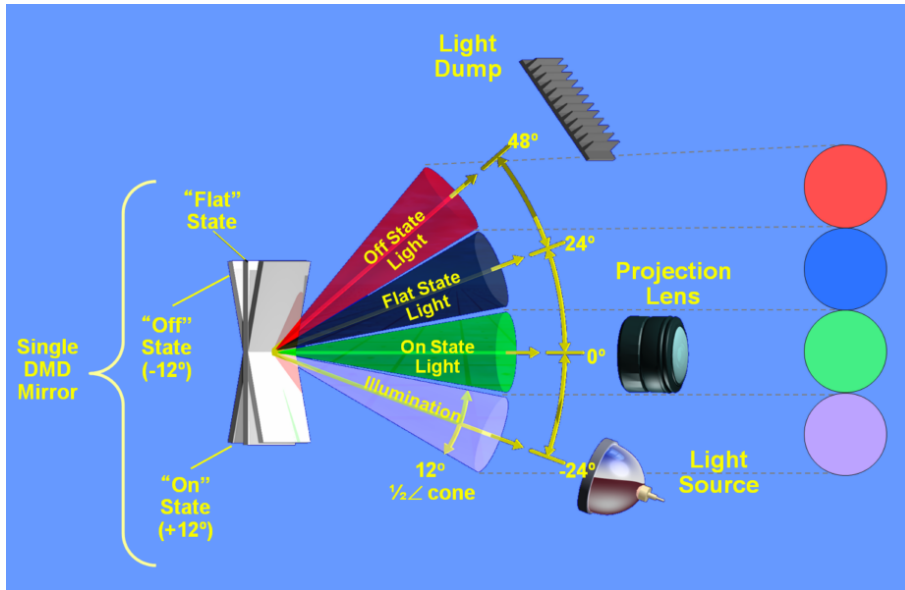
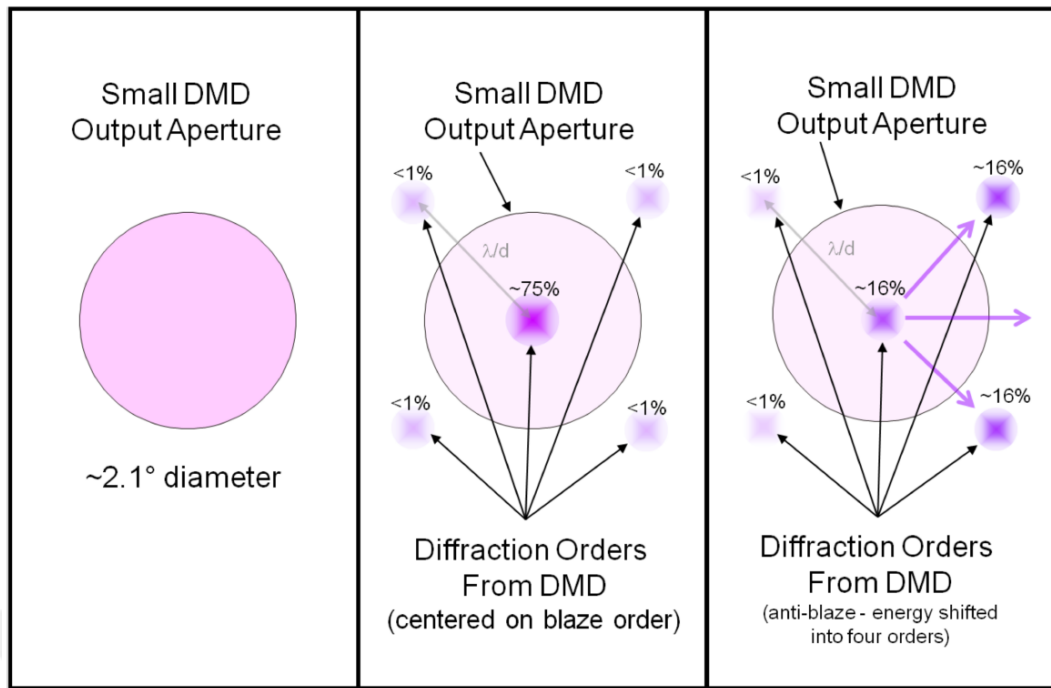


Figure 3.8: A depiction of DMD chip illumination angle and micro-mirror tilt axis. Image retrieved from [8].

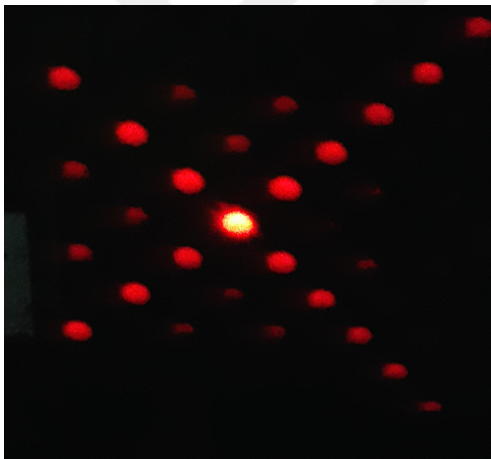
numeric range of 0 – 255 is sufficient for measuring the PSF of a photon sieve having a small number of white zones.

### 3.3.2 PSF Measurements and Comparisons

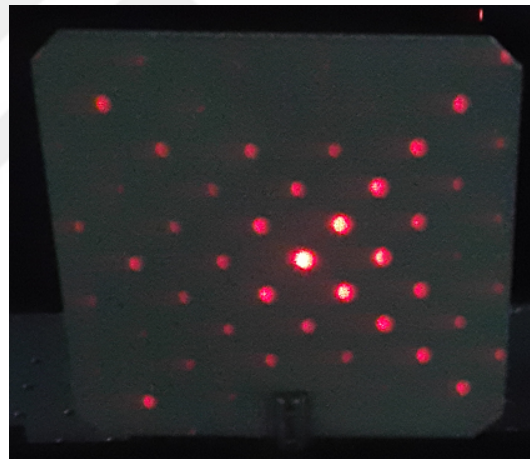
Using the experimental setup described in Sect. 3.3.1, PSF is measured at different distances from the photon sieve and the experimental results are compared to that of theoretical PSFs computed using the fast method in Sect. 3.2. To obtain verifiable and conclusive results that serve as a proof of concept for both the DMD-based photon sieve system and the fast PSF computation method, the experimental setup is tested with a photon sieve design that has relatively low peak-to-sidelobe ratio and a wide main lobe. There are two main reasons for this choice. First, increasing the number of zones leads to smaller holes on the outermost white zone and thus a sharper PSF. Given that the spatial resolution of the constructed imaging system is limited by the pixel pitch of the detector, a sharper peak would be captured with a smaller number of detector pixels. For this reason, a photon sieve having a PSF with wider main lobe is chosen. Second, the relative intensity value of the first sidelobe of the PSF compared



(a)



(b)



(c)

Figure 3.9: (a) Theoretical demonstration of the "blaze" and "anti-blaze" conditions. Retrieved from [9]. (b) - (c) Experimental diffraction patterns for "blaze" and "anti-blaze" conditions, respectively. Note that in (b), most of the energy is contained within the  $0^{th}$  diffraction order at the center, and in (c), most of the energy is distributed between four brightest orders.

to its main lobe depends on the number of white zones in the design. Because the dynamic range of the utilized detector is 0 – 255, a photon sieve with small number

of white zones is used to decisively measure the intensity of the sidelobes.

Properties of the utilized photon sieve design for the experimental tests are given in Table 3.1, where  $\Delta$  is diameter of the holes in outermost zone and  $d/w$  ratio is the ratio of diameter of a pinhole to the width of its underlying Fresnel zone. Also, corresponding aperture transmission function of the photon sieve sampled according to the pixel pitch of the DMD is shown in Fig. 3.10.

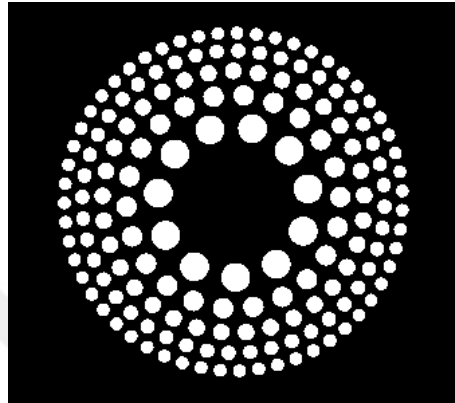


Figure 3.10: Aperture transmission function of the tested photon sieve.

Sieve Properties						
D (mm)	$\lambda$ (nm)	f (m)	$\Delta$ ( $\mu$ m)	$N_{zones}$	DOF (mm)	d/w ratio
2.00	632.80	0.14	45.36	5	$\pm 6.50$	1.53

Table 3.1: Properties of the tested photon sieve.

PSF measurements are obtained at different measurement planes, each with a different amount of depth of focus (DOF). Note that the depth of focus for a photon sieve design is given as  $DOF = \pm 2\Delta^2/\lambda$  where  $\lambda$  is the wavelength of interest and  $\Delta$  is the diameter of holes in the outermost zone of the photon sieve. Experimental results obtained with the setup are summarized in Fig. 3.11. In Figures 3.11b, 3.11d and 3.11f, 2-D theoretical and measured PSFs are shown for measurement planes located at 0, +1 and +3 depth of focus away from the focus. Note that each upper sub-figure is for the theoretical PSF, whereas the lower sub-figure is for the experimental PSF. Also in Figures 3.11a, 3.11c, 3.11e, the cross-sectional views of the corresponding PSFs are shown.



Results show strong agreement between the theoretical and experimental cases especially in terms of the width of the main lobes and the location of the minima. Slight deviations from the theoretical ones are observed in the measured PSFs due to off-axis illumination effects, which cause some stretching as explained in [73]. However, although the photon sieve aperture is constructed using DMD which suffers from errors due to pixelation and null zones between the DMD micro-mirrors, there is still good agreement between theoretical and experimental PSFs which suggests that such errors in the generated aperture function do not significantly distort the PSF.



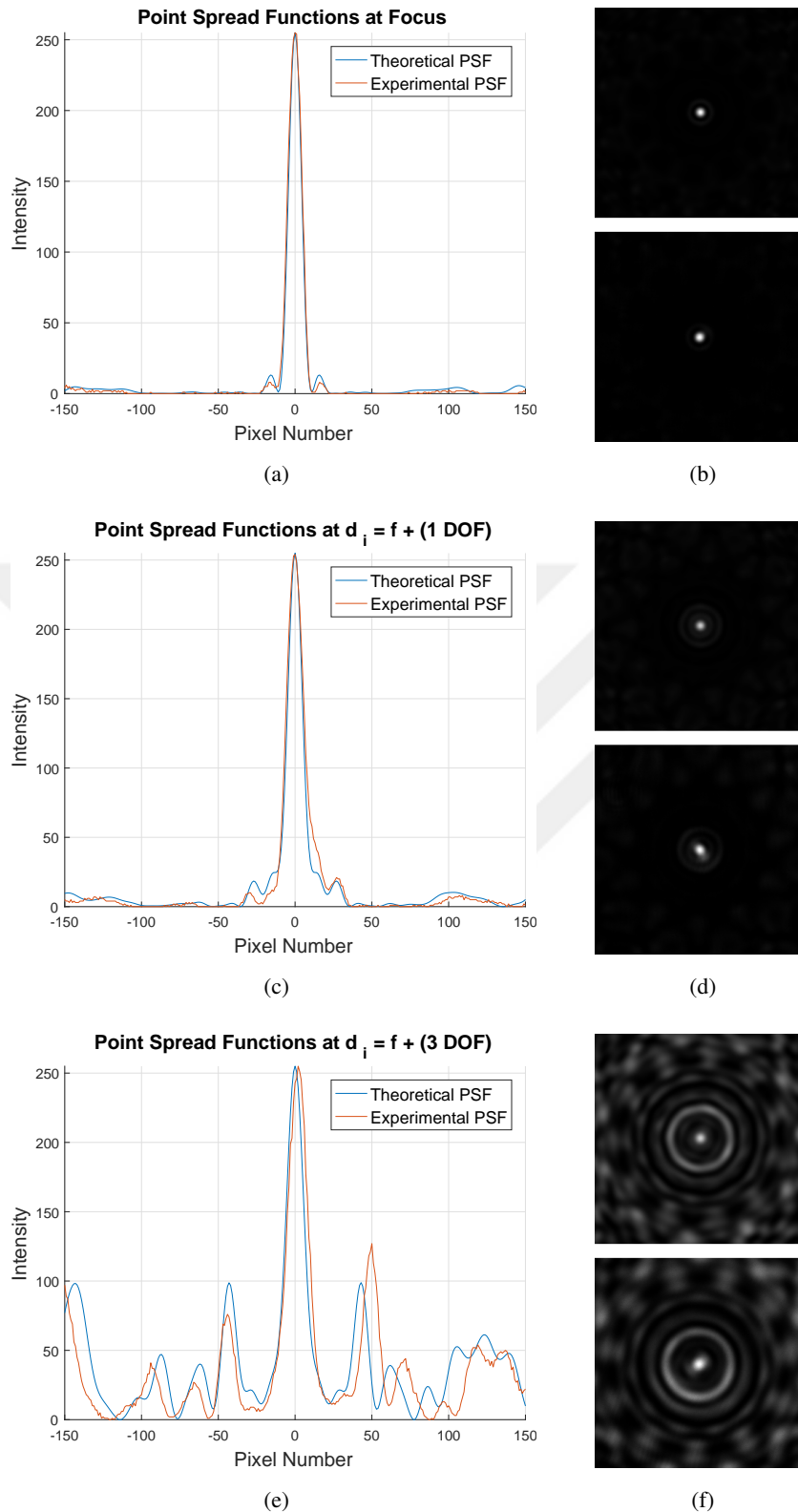


Figure 3.11: (a),(c), and (e): The cross-sectional views of the theoretical and experimental PSFs, respectively, at the focus, +1 and +3 depth of focus away from the focus. (b), (d), and (f): The corresponding 2D PSFs (top: theoretical, bottom: experimental).

## CHAPTER 4

# PERFORMANCE ANALYSIS OF PHOTON SIEVE SPECTRAL IMAGING

The photon sieve based spectral imaging modality developed in [59] uses a computational image formation approach for spectral imaging. In this section, performance of the image reconstruction method used in this modality will be analysed. The imaging system, forward problem and the corresponding inverse problem will be described briefly in Sect. 4.1. The reconstruction algorithm that provides a numerical solution to the inverse problem is then presented in Sect. 4.2. Finally, the reconstruction performance for different observing scenarios will be investigated in Sect. 4.3 along with different regularization choices.

### 4.1 Computational Spectral Imaging with Photon Sieves

The photon sieve based spectral imaging technique relies on the wavelength dependent focusing property of the photon sieve described in Sect. 3.1.2. In this technique, a photon sieve imaging system is used together with an image reconstruction method. In the image reconstruction method, mathematical model of the imaging system is used in an inverse problem framework to separate the contributions from each discrete spectral component and form their corresponding spectral images. The imaging system for which the reconstruction method is developed is depicted in Fig. 4.1.

In the imaging system shown in Fig. 4.1, the input light field consists of illumination from incoherent sources with different wavelengths  $\lambda_p$  for  $p = 1, 2, \dots, P$ . The source is located before the photon sieve with a spacing of  $d_s$ . A total of  $K$  measurements

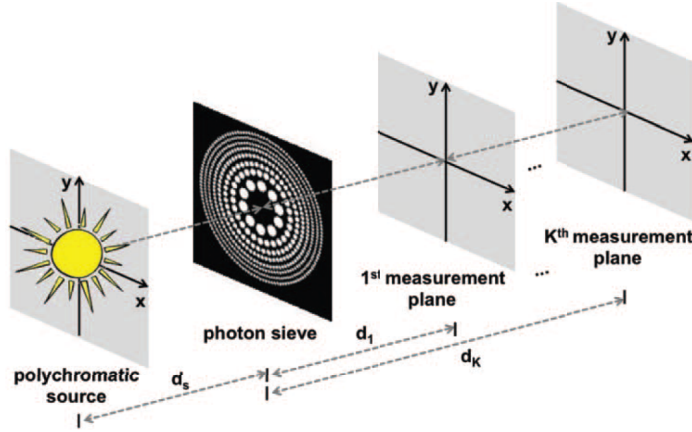


Figure 4.1: Imaging system used in photon sieve based spectral imaging technique. Image retrieved from [6]. © 2014 IEEE.

are assumed to be taken, each at a different distance,  $d_k$ , from the photon sieve plane where  $k = 1, 2, \dots, K$ . Sample observations are shown in Fig. 4.2 simulated for the case with two monochromatic sources and two observations taken at the focus of each wavelength of interest. Contributions of the two monochromatic sources to each observation are also shown along with a set of sample reconstructed images. The method used to obtain these reconstructed images are explained below.

As described in 3.2.1, the point-spread function relates the input of an imaging system to its output at a plane of measurement, and the output can be obtained by convolving the corresponding PSF with the input. Thus, for the photon sieve imaging system, the formed image in the  $k^{th}$  measurement plane,  $t_k[m, n]$ , can be expressed in discrete form as

$$t_k[m, n] = \sum_{p=1}^P \tilde{s}_p[m, n] * g_{\lambda_p, d_k}[m, n] \quad (4.1)$$

where  $\tilde{s}_p[m, n]$  is the diffraction-limited discrete intensity function of the  $p^{th}$  source with a wavelength of  $\lambda_p$  and  $g_{\lambda_p, d_k}[m, n]$  is the discrete point-spread function for a measurement plane separation of  $d_k$  and for the associated wavelength of  $\lambda_p$ . Here the discretization corresponds to sampling on the detector with a pixel size that satisfies

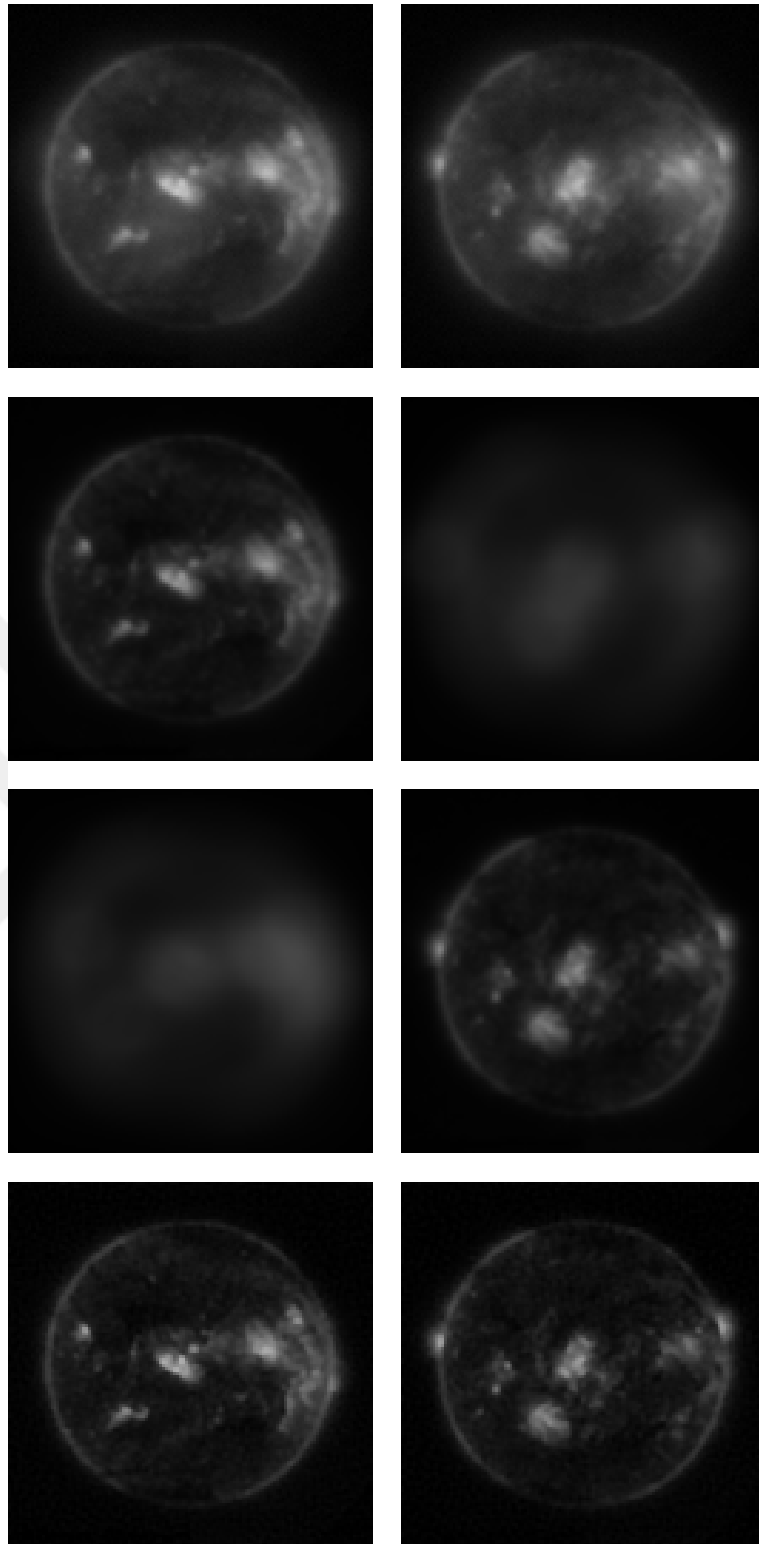


Figure 4.2: Top row: Obtained observations at the focus of each wavelength of interest. Second row: Contributions of the first and second sources to the observation at the focus of  $\lambda_1$ . Third row: Contributions of the first and second sources to the observation at the focus of  $\lambda_2$ . Bottom row: Reconstructed images for both sources.

the Nyquist criteria. Putting Eqn. 4.1 into matrix-vector form yields

$$\mathbf{t}_k = \sum_{p=1}^P \mathbf{H}_{k,p} \tilde{\mathbf{s}}_p \quad (4.2)$$

where  $\tilde{\mathbf{s}}_p$  is the  $N^2 \times 1$  lexicographically reordered vector form of the matrix that contains  $N \times N$  samples of  $\tilde{s}_p[m, n]$ , and  $\mathbf{H}_{k,p}$  is  $N^2 \times N^2$  convolution operator that performs the convolution of  $\tilde{s}_p[m, n]$  with its corresponding PSF,  $g_{\lambda_p, d_k}[m, n]$ . Then, by combining observations from all measurement planes into a single vector,  $\mathbf{t}'$ , and intensity images of all sources into a single vector,  $\tilde{\mathbf{s}}$ , the problem converts to the form of  $\mathbf{t}' = \mathbf{H}\tilde{\mathbf{s}}$  where

$$\mathbf{H} = \begin{bmatrix} \mathbf{H}_{1,1} & \cdots & \mathbf{H}_{1,P} \\ \vdots & \ddots & \vdots \\ \mathbf{H}_{K,1} & \cdots & \mathbf{H}_{K,P} \end{bmatrix} \quad (4.3)$$

$$\tilde{\mathbf{s}} = \begin{bmatrix} \tilde{\mathbf{s}}_1 \\ \tilde{\mathbf{s}}_2 \\ \vdots \\ \tilde{\mathbf{s}}_P \end{bmatrix} \quad (4.4)$$

$$\mathbf{t}' = \begin{bmatrix} \mathbf{t}_1 \\ \mathbf{t}_2 \\ \vdots \\ \mathbf{t}_K \end{bmatrix} \quad (4.5)$$

Note that, the  $KN^2 \times PN^2$  matrix  $\mathbf{H}$  is formed by combining matrices  $\mathbf{H}_{k,p}$  as in above and  $KN^2 \times 1$  vector  $\mathbf{t}'$  and  $PN^2 \times 1$  vector  $\tilde{\mathbf{s}}$  are formed by vertically concatenating lexicographically reordered measurements and intensity images. Then, a complete mathematical expression for the combined observation vector,  $\mathbf{t}$ , can be obtained by including an additive noise to the model as the measurement noise. Thus, the final

mathematical expression for the forward problem is

$$\mathbf{t} = \mathbf{H}\tilde{\mathbf{s}} + \mathbf{w} \quad (4.6)$$

where  $\mathbf{w}$  is assumed to be white Gaussian that is uncorrelated across different measurement planes and spatial pixels. The problem of recovering  $\tilde{\mathbf{s}}$  from  $\mathbf{t}$  is the inverse problem to be solved to reconstruct the spectral images.

Solving inverse problems is a well-studied subject [74]. In [6], the inverse problem in photon sieve based spectral imaging is formulated as a least-squares minimization problem with  $\ell_p$ -norm regularization given as

$$\underset{\tilde{\mathbf{s}}}{\operatorname{argmin}} \|\mathbf{t} - \mathbf{H}\tilde{\mathbf{s}}\|_{W_H}^2 + \alpha^2 \|\mathbf{L}\tilde{\mathbf{s}}\|_p^p. \quad (4.7)$$

Here, the operator  $\mathbf{L}$  is the regularization operator chosen to be the discrete derivative operator in [6],  $W_H$  is a weighting matrix that incorporates varying SNR levels over different measurement planes,  $\alpha$  is the regularization parameter that controls the contribution of the regularization term and  $\mathbf{t}$  is the vector formed by concatenating lexicographically reordered noisy measurements. Optimization problem in Eqn. 4.7 yields a solution for  $\tilde{\mathbf{s}}$  by minimizing the difference between the measurements and the model with the regularization term allowing prior information about  $\tilde{\mathbf{s}}$  to be imposed on the solution.

## 4.2 Image Reconstruction Algorithm

Numerical solution of the minimization problem in Eqn. 4.7 requires careful attention. First consider the case  $p = 2$ . In this case, the solution can be obtained by differentiating the objective function with respect to  $\tilde{\mathbf{s}}$  and equating it to zero. This results in the following equation:

$$(\mathbf{H}^T \mathbf{W}_H \mathbf{H} + \alpha^2 \mathbf{L}^T \mathbf{W}_L \mathbf{L}) \tilde{\mathbf{s}} = \mathbf{H}^T \mathbf{W}_H \mathbf{t} \quad (4.8)$$

where  $\mathbf{W}_L$  is a general weighting matrix for the  $\ell_2$ -norm regularization term, which is identity for the case in Eqn. 4.7. One can obtain the solution,  $\tilde{\mathbf{s}}_{\text{est}}$ , to this linear equation by setting

$$\mathbf{A} = \mathbf{H}^T \mathbf{W}_H \mathbf{H} + \alpha^2 \mathbf{L}^T \mathbf{W}_L \mathbf{L} \quad (4.9)$$

$$\mathbf{b} = \mathbf{H}^T \mathbf{W}_H \mathbf{t} \quad (4.10)$$

$$\tilde{\mathbf{s}}_{\text{est}} = \mathbf{A}^{-1} \mathbf{b}. \quad (4.11)$$

---

```

1 :   Compute  $r^{(0)} = b - Ax^{(0)}$  for some initial guess  $x^{(0)}$ 
2 :   for  $i = 1, 2, \dots$ 
3 :       solve  $Mz^{(i-1)} = r^{(i-1)}$ 
4 :        $\rho_{i-1} = r^{(i-1)T} z^{(i-1)}$ 
5 :       if  $i = 1$ 
6 :            $p^{(1)} = z^{(0)}$ 
7 :       else
8 :            $\beta_{i-1} = \rho_{i-1} / \rho_i - 2$ 
9 :            $p^{(i)} = z^{(i-1)} + \beta_{i-1} p^{i-1}$ 
10 :      endif
11 :       $q^{(i)} = Ap^{(i)}$ 
12 :       $\alpha_i = \rho_{i-1} / p^{(i)T} q^{(i)}$ 
13 :       $x^{(i)} = x^{(i-1)} + \alpha_i p^{(i)}$ 
14 :       $r^{(i)} = r^{(i-1)} - \alpha_i q^{(i)}$ 
15 :      Check convergence; continue if necessary.
16 :   end

```

---

Figure 4.3: Pseudo-code for the preconditioned conjugate gradient algorithm.

Yet, given that the matrix  $\mathbf{A}$  is of dimensions  $PN^2 \times PN^2$ , it is not practical to compute the inverse of  $\mathbf{A}$  or even to explicitly form  $\mathbf{A}$  due to memory limitations. To overcome this problem, an optimization algorithm such as preconditioned conjugate gradient (PCG) algorithm can be used to iteratively obtain the solution. Such an algorithm eliminates the need to explicitly form  $\mathbf{A}^{-1}$  or  $\mathbf{A}$ , and instead computes the



forward problem and updates the guess for the solution in each iteration. Pseudo-code for the PCG algorithm applied to a general linear problem of the form  $\mathbf{Ax} = \mathbf{b}$  is given in Fig. 4.3.

Although using PCG successfully avoids the inversion of the matrix  $\mathbf{A}$  and saves a significant amount of computational time, it still requires forming the matrix  $\mathbf{A}$  explicitly, as it is needed in lines 1 and 11 of the pseudo-code in Fig. 4.3. To avoid explicitly forming of  $\mathbf{A}$ , a modified version of the PCG algorithm can be used. By expressing  $\mathbf{A}$  as in Eqn. 4.9, 1<sup>st</sup> and 11<sup>th</sup> lines of the pseudo-code can be expressed as in the modified pseudo-code shown in Fig. 4.4.

---

```

1 :   Compute  $r^{(0)} = (H^T W_H t) - H^T [W_H (Hx^{(0)})] - \alpha^2 L^T [W_L (Lx^{(0)})]$  for  $x^{(0)}$ 
2 :   for  $i = 1, 2, \dots$ 
3 :       solve  $Mz^{(i-1)} = r^{(i-1)}$ 
4 :        $\rho_{i-1} = r^{(i-1)T} z^{(i-1)}$ 
5 :       if  $i = 1$ 
6 :            $p^{(1)} = z^{(0)}$ 
7 :       else
8 :            $\beta_{i-1} = \rho_{i-1} / \rho_i - 2$ 
9 :            $p^{(i)} = z^{(i-1)} + \beta_{i-1} p^{i-1}$ 
10 :      endif
11 :       $q^{(i)} = H^T [W_H (Hp^{(i)})] + \alpha^2 L^T [W_L (Lp^{(i)})]$ 
12 :       $\alpha_i = \rho_{i-1} / p^{(i)T} q^{(i)}$ 
13 :       $x^{(i)} = x^{(i-1)} + \alpha_i p^{(i)}$ 
14 :       $r^{(i)} = r^{(i-1)} - \alpha_i q^{(i)}$ 
15 :      Check convergence; continue if necessary.
16 :   end

```

---

Figure 4.4: Pseudo-code for the modified preconditioned conjugate gradient algorithm.

Because  $\mathbf{H}$  and  $\mathbf{L}$  are real-valued matrices in this problem,  $\mathbf{H}^T$  and  $\mathbf{L}^T$  correspond to the adjoint of the operators  $\mathbf{H}$  and  $\mathbf{L}$  where adjoint in this case is simply the Hermitian transpose of a matrix. The advantage of replacing  $\mathbf{A}$  with its expanded form can be

understood by considering the operators  $\mathbf{H}$  and  $\mathbf{L}$  along with their adjoints. Given that the matrix  $\mathbf{H}$  corresponds to the operator form of the superimposed convolutions with the PSFs of the imaging system, multiplication of  $\mathbf{H}$  with a vector is simply equivalent to computing these superimposed convolutions. Similarly, suppose that the matrix  $\mathbf{L}$  is taken as the discrete derivative operator. Then, multiplication with  $\mathbf{L}$  can simply be carried out by convolving the operand with the corresponding derivative kernel. As a result, explicitly forming the matrices  $\mathbf{H}$  and  $\mathbf{L}$  is not required. Also, because the matrix multiplication with  $\mathbf{H}^T$  and  $\mathbf{L}^T$  corresponds to convolution with the time-reversed versions of the kernels  $\mathbf{H}$  and  $\mathbf{L}$ , explicitly forming these adjoint matrices is not necessary either.

Described numerical approach is intended to be used for the special case when  $p = 2$ . For  $p \neq 2$ , obtaining the solution of the minimization problem in Eqn. 4.7 requires a different approach. The regularization term with  $\ell_p$ -norm is given by

$$\|\mathbf{L}\tilde{\mathbf{s}}\|_p^p = \sum_{i=1}^n |[\mathbf{L}\tilde{\mathbf{s}}]_i|^p. \quad (4.12)$$

This equation is not differentiable at 0 because it contains the absolute value of each element in the vector  $\mathbf{L}\tilde{\mathbf{s}}$  and the absolute value function is not differentiable at the origin. To be able to differentiate the regularization term in the minimization problem, a smooth approximation to the  $\ell_p$ -norm regularization can be used [75]. After smooth approximation, the minimization problem becomes

$$\underset{\tilde{\mathbf{s}}}{\operatorname{argmin}} \|\mathbf{t} - \mathbf{H}\tilde{\mathbf{s}}\|_{W_H}^2 + \alpha^2 \sum_{i=1}^n ([\mathbf{L}\tilde{\mathbf{s}}]_i^2 + \beta)^{p/2} \quad (4.13)$$

where  $\beta$  is the smoothing parameter. Note that when  $\beta = 0$  the above equation turns into the original minimization problem. For a sufficiently small  $\beta$  value, the above equation provides a differentiable approximation to the original problem.

Differentiating the new objective function in Eqn. 4.13 with respect to  $\tilde{\mathbf{s}}$  and equating

it to zero gives

$$-2\mathbf{H}^T\mathbf{W}_H\mathbf{t} + 2\mathbf{H}^T\mathbf{W}_H\mathbf{H}\tilde{\mathbf{s}} + 2\alpha^2\sum_{i=1}^n[\mathbf{L}^T]_i\frac{p/2}{([\mathbf{L}\tilde{\mathbf{s}}]_i^2 + \beta)^{1-p/2}}[\mathbf{L}\tilde{\mathbf{s}}]_i = 0 \quad (4.14)$$

this can be rewritten as

$$-2\mathbf{H}^T\mathbf{W}_H\mathbf{t} + 2\mathbf{H}^T\mathbf{W}_H\mathbf{H}\tilde{\mathbf{s}} + 2\alpha^2\mathbf{L}^T\mathit{diag}\left(\frac{p/2}{([\mathbf{L}\tilde{\mathbf{s}}]_i^2 + \beta)^{1-p/2}}\right)\mathbf{L}\tilde{\mathbf{s}} = 0 \quad (4.15)$$

$$\left(\mathbf{H}^T\mathbf{W}_H\mathbf{H} + \alpha^2\mathbf{L}^T\mathit{diag}\left(\frac{p/2}{([\mathbf{L}\tilde{\mathbf{s}}]_i^2 + \beta)^{1-p/2}}\right)\mathbf{L}\right)\tilde{\mathbf{s}} = \mathbf{H}^T\mathbf{W}_H\mathbf{t}. \quad (4.16)$$

Note the resemblance of Eqn. 4.16 to the closed-form solution of  $\ell_2$ -norm regularization given in Eqn. 4.8. This can be visualized by setting

$$\mathbf{W}_L = \mathit{diag}\left(\frac{p/2}{([\mathbf{L}\tilde{\mathbf{s}}]_i^2 + \beta)^{1-p/2}}\right). \quad (4.17)$$

Despite the fact that the Eqns. 4.16 and 4.8 appears to be of the same form, there is an important difference. In Eqn. 4.16, the weighting matrix,  $\mathbf{W}_L$ , depends on  $\tilde{\mathbf{s}}$ . As a result, the equation 4.16 does not have a closed-form solution, hence cannot be directly solved by using the PCG algorithm as in  $p = 2$  case. However, a simple iterative fixed-point algorithm can be used to obtain its solution. For this, one can first hold  $\mathbf{W}_L$  fixed and solve the resulting set of linear equations for  $\tilde{\mathbf{s}}$  using PCG, then hold  $\tilde{\mathbf{s}}$  fixed and update the weighting matrix  $\mathbf{W}_L$ , and repeat this process until convergence. This will give a numerical solution to the problem for the case  $p \neq 2$ .

### 4.3 Performance Analysis

To assess the performance of the reconstruction method, a comprehensive set of numerical simulations are performed. In this section, information about the utilized image quality metrics, dataset and regularization choices will be given in Sections 4.3.1,

4.3.2 and 4.3.3, respectively. Then, the performance of the reconstruction method will be numerically investigated in Sect. 4.4 by considering different practical scenarios of interest such as for varied number of observations, amount of measurement noise, measurement plane locations and spectral composition of the scene.

### 4.3.1 Reconstruction Performance Metrics

Throughout the numerical experiments, the image reconstruction fidelity is measured by numerically comparing the reconstructed images with the diffraction-limited true intensity images where the diffraction-limit is the result of the finite-sized aperture of the photon sieve. For this purpose, two image quality metrics are used: Peak signal-to-noise ratio (PSNR) and structural similarity index (SSIM). Note that results that will be presented here are the average success for all reconstructed images, where the reconstruction performance corresponding to the wavelength with a smaller focal length is found to be slightly better for all cases.

- **Peak Signal-to-Noise Ratio:** PSNR is ratio of the maximum possible intensity value for the reference image to the mean squared error (MSE) between the reference and distorted images. Given the reference and reconstructed images in the vector form as  $x = \{x_i | i = 1, \dots, N\}$  and  $y = \{y_i | i = 1, \dots, N\}$ , respectively, then PSNR in dB is defined as [76]

$$PSNR(x, y) = 10 \log_{10} \left( \frac{I_{max}^2}{\frac{1}{N} \sum_{i=1}^N (x_i - y_i)^2} \right) \quad (4.18)$$

where  $I_{max}$  is the maximum value allowed in the reference image (i.e. image dynamic range),  $N$  is the total number of pixels, and  $x_i$  and  $y_i$  are the  $i^{th}$  element of the reference and reconstructed images, respectively.

- **Structural Similarity Index:** SSIM is an image quality metric that compares a reconstructed image to a reference image in terms of the similarity of luminance, contrast and structure [77]. Formal definition for SSIM is given as

$$SSIM(x, y) = [l(x, y)]^\alpha [c(x, y)]^\beta [s(x, y)]^\gamma \quad (4.19)$$

where

$$l(x, y) = \frac{2\mu_x\mu_y + c_1}{\mu_x^2 + \mu_y^2 + c_1}, \quad (4.20)$$

$$c(x, y) = \frac{2\sigma_x\sigma_y + c_2}{\sigma_x^2 + \sigma_y^2 + c_2}, \quad (4.21)$$

$$s(x, y) = \frac{\sigma_{xy} + c_3}{\sigma_x\sigma_y + c_3}. \quad (4.22)$$

Parameters  $\mu_x$ ,  $\mu_y$ ,  $\sigma_x$ ,  $\sigma_y$  and  $\sigma_{xy}$  are local sample means, standard deviations and correlation coefficient of  $x$  and  $y$ . Also,  $\alpha$ ,  $\beta$ ,  $\gamma$  are the weight parameters that determine the relative importance of the three components, and  $c_1$ ,  $c_2$  and  $c_3$  are small constants used to stabilize each expression when the denominator is small. SSIM index is obtained using a sliding window over the entire images, calculating the SSIM index within each local window, and then averaging all of these SSIM values to obtain a single SSIM value.

### 4.3.2 Utilized Images for Performance Analysis

It is important to use images with different characteristics to be able to objectively evaluate the performance of reconstruction. For this purpose, four different pairs of images with size 128x128 are used in the numerical simulations as the intensity images of two sources with wavelengths 33.4 nm and 33.5 nm. These four pairs are as follows: Two pairs of solar spectral images, a pair consisting of different bands of Indian pines spectral image data set and another pair consisting of completely different natural images.

- **Solar Images:** One of the important contributions of the spectral imaging technique with photon sieves is the improved spectral resolution. One application area where this contribution is prominent is EUV solar imaging since the spectrum in this application contains discrete wavelengths within a close spectral range. For example, obtaining diffraction-limited images of the discrete emissions in 33.4 and 33.5 nm wavelengths is an important application in solar imaging [60] and this is not possible with the state-of-the-art spectral imagers.

To demonstrate the performance of the spectral imaging technique for this practical scenario, two pairs of solar images obtained for a spectral band centered at 33.5 nm is used in this study where one of each pair is considered as the emission at 33.4 nm wavelength and the other is at 33.5 nm. Furthermore, one pair is selected from solar images that are visually similar to each other whereas the second pair contains more spatial difference. These solar images are shown in Fig. 4.5.

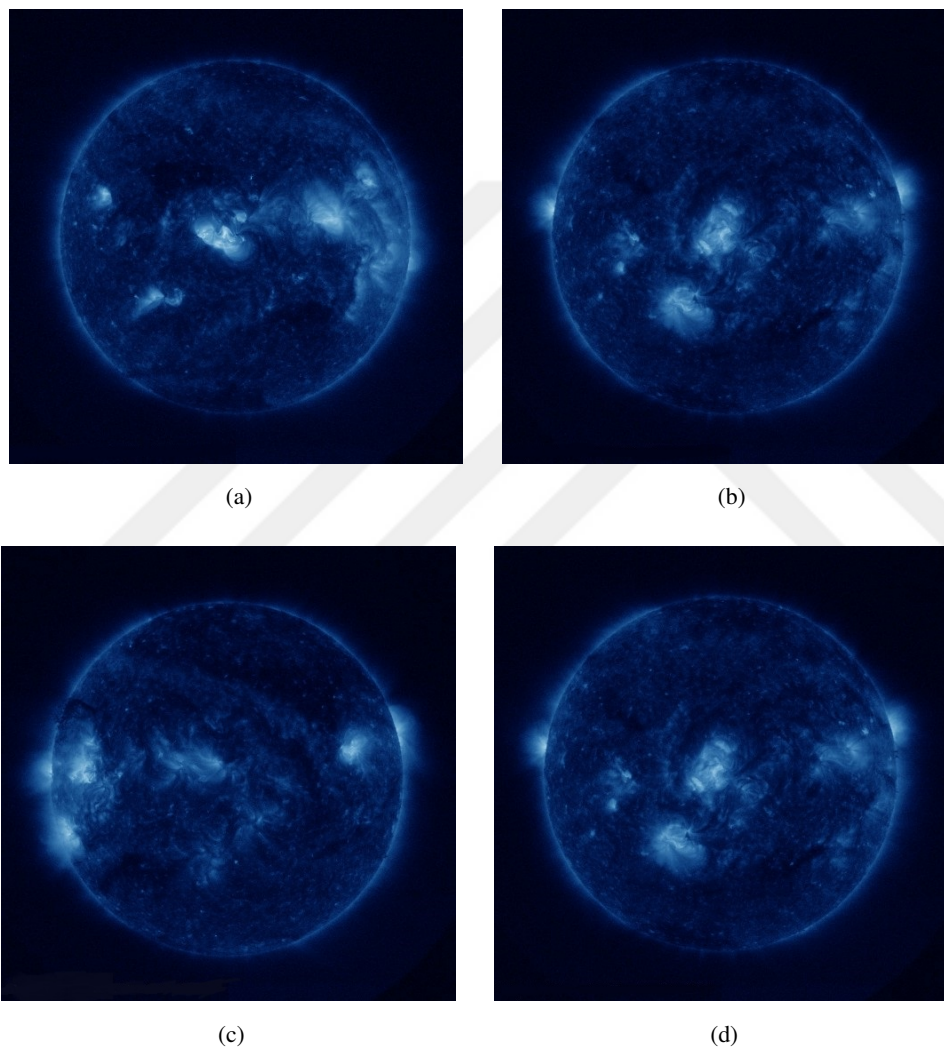


Figure 4.5: (a) - (b) and (c) - (d): Two pairs of solar images that are used for performance evaluation. Note the visual resemblance of the upper pair. Pairs a-b and c-d will be referred as SI1 and SI2. Courtesy of NASA/SDO and the AIA, EVE and HMI science teams.

- **Indian Pines:** This spectral image data set has a datacube size of 145x145x224 and is captured using AVIRIS sensor that covers a spectral range of 400 nm - 2500 nm. The scene includes two main highways, a rail line, some built structures and several fields of agricultural products. A pair of images from different bands of this datacube is used and is shown in Fig. 4.6.

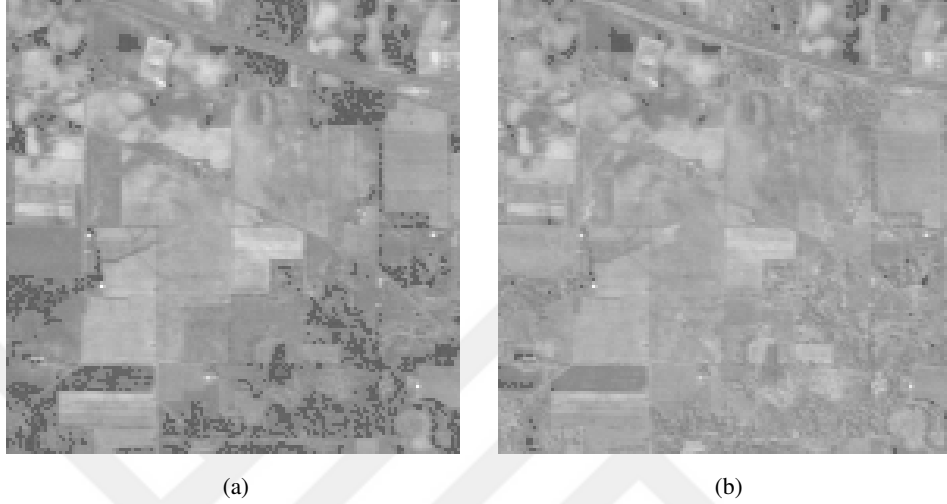


Figure 4.6: (a) - (b): A pair of images from the corrected Indian pines dataset that will be referred to as IP.

- **Natural Images:** This pair consists of the grayscale versions of the well-known "Cameraman" and "Lena" images which are shown in Fig. 4.7a and 4.7b. This completely different pair of natural images is used to obtain an insight about the performance of the technique when the two spectral images, unlike other pairs, are poorly correlated.

An accurate simulation of the measurement data, as given in Eqn. 4.6, requires the presence of noise. To simulate the measurement noise of the detector, an additive white Gaussian noise is added to all simulated measurements. The amount of added noise is characterized in terms of SNR where SNR is defined as [76]

$$SNR(dB) = 10 \log_{10} \left( \frac{\sigma_t^2}{\sigma_n^2} \right), \quad (4.23)$$

and  $\sigma_t^2$  and  $\sigma_n^2$  are the variances of the simulated output data,  $t$ , and the additive noise,



Figure 4.7: (a) "Cameraman" and (b) "Lena" images.

w, respectively.

### 4.3.3 Regularization Choices

In the original reconstruction method developed for photon sieve spectral imaging [6], discrete derivative operator (DDO), which penalizes total variation in the reconstructed images when  $p$  is set to 1, is used as the regularization operator  $\mathbf{L}$ . In this study, performance evaluation of the spectral imaging modality is not only tested with the discrete derivative operator, but also with different choices of regularization operators. In this section, these regularization choices will be explained.

- **Discrete Derivative Operator (DDO):** This regularization choice, known as total variation when  $p = 1$ , incorporates prior information about the variations in the images. To include the discrete derivative operator along both  $x$  and  $y$  directions, the regularization matrix is defined as

$$\mathbf{L} = \begin{bmatrix} \mathbf{D}_x \\ \mathbf{D}_y \end{bmatrix} \quad (4.24)$$

where  $\mathbf{D}_x$  and  $\mathbf{D}_y$  are the discrete approximations to the gradient operator along  $x$  and  $y$  directions, each with dimensions  $N^2 \times N^2$  for an image of size  $N \times N$ .



- **Discrete Cosine Transform (DCT):** Setting matrix  $\mathbf{L}$  in the regularization term of Eqn. 4.7 as the DCT operator, one can determine a solution for  $\tilde{\mathbf{s}}$  that minimizes the  $\ell_p$ -norm of its DCT coefficients along with the least-squares data fidelity term. The DCT is an important tool in signal and image processing, especially for lossy compression and sparse representation. For example, in JPEG compression, it enables lossy compression when applied on an image by discarding the small-valued coefficients corresponding generally to higher frequency components of the DCT. In this study, 2-D DCT coefficients are computed for the entire image as a whole, rather than block processing as in JPEG compression.
- **Discrete Wavelet Transform (DWT):** DWT is another commonly used sparsifying transform. In fact, it is well-known that DWT coefficients of natural images tends to be sparse. In this study, Symmlet-8 wavelet is used in a 2-level wavelet decomposition process, and the resulting coefficients are used in the regularization term.

#### 4.4 Numerical Results

A series of numerical experiments is performed to evaluate the performance of the spectral imaging technique with photon sieves, focusing on its reconstruction aspect. Throughout the experiments, a photon sieve design with a diameter of 25 mm, a minimum fabricable structure of 5  $\mu\text{m}$  and a number of transparent zones of 125 is used along with two sources of wavelengths 33.4 and 33.5 nm. Also, smoothing parameter,  $\beta$ , in the approximated  $\ell_p$ -norm regularization term is chosen to be  $10^{-5}$  and SNR is fixed to 30 dB except for the experiment in Sect. 4.4.3 where the effect of SNR on the reconstruction performance is investigated. As part of the numerical experiments, optimum values for the regularization parameters are determined for each choice of the regularization operator and for each image pair in Sect. 4.4.1, the effect of measurement plane locations on the reconstruction performance is investigated in Sect. 4.4.2, effect of number of observations is examined in Sect. 4.4.4 and finally, effect of spectral separation between two sources is analyzed in Sect. 4.4.5.

#### 4.4.1 Selection of Regularization Parameters

The minimization problem contains two free parameters to choose, namely  $\alpha$  and  $p$ . In this section, the effect of these regularization parameters on the performance of image reconstruction will be evaluated for different choices of regularization operators and image pairs.

To evaluate the success of each regularization operator given in Sect. 4.3.3, the optimal pair of  $(\alpha, p)$  parameters is determined for each case. Reconstruction performance as a function of regularization parameters is given in Appendix A for each regularization operator and image pair. There, contour plots for all combinations of images, regularization operators and quality metrics are available for an SNR value of 30 dB. Reconstructed images with different regularization operators and optimal regularization parameters are given in Figures 4.10, 4.11, 4.12 for SI1, IP and NI image pairs, respectively. Also the reconstruction quality obtained with optimal regularization parameters is summarized in Table 4.1.

	SI1		SI2		IP		NI		Avg. SSIM	Avg. PSNR
	SSIM	PSNR	SSIM	PSNR	SSIM	PSNR	SSIM	PSNR		
DDO	0.974	42.479	0.972	41.095	0.961	38.401	0.939	32.923	<b>0.961</b>	<b>38.725</b>
DCT	0.969	41.869	0.965	40.066	0.958	37.995	0.909	31.540	0.950	37.868
DWT	0.969	41.841	0.964	40.026	0.958	37.346	0.905	31.368	0.949	37.645
Average	0.971	42.063	0.967	40.396	0.959	37.914	0.918	31.944	0.953	38.079

Table 4.1: Reconstruction performance with optimal regularization parameters for each regularization operator and image pair.

For SI1 image pair, Fig. 4.8 shows the detailed reconstruction performance as a function of regularization parameters for the three different regularization operators. Quick examination of Table 4.1 and Fig. 4.8 reveals that the best regularization operator is DDO for all the image pairs used. In fact, results show that DDO operator performs better than all other regularization operators regardless of the pair of images that is used. For this reason, in the remaining tests, only DDO operator will be used for regularization.

For the outperforming DDO operator, Fig. 4.9 shows the detailed reconstruction performance as a function of regularization parameters for all different image pairs. Note

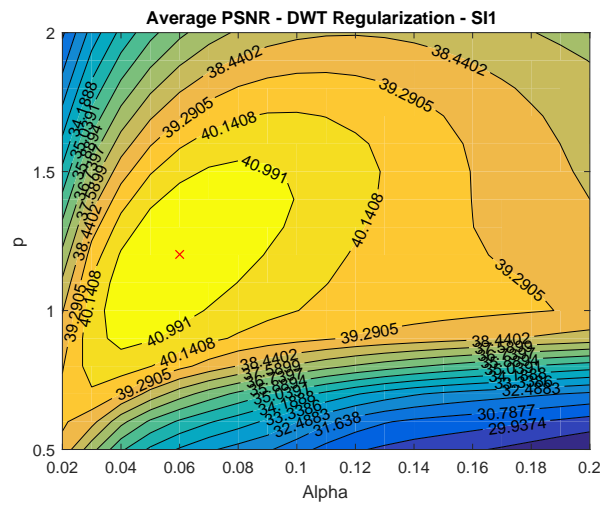
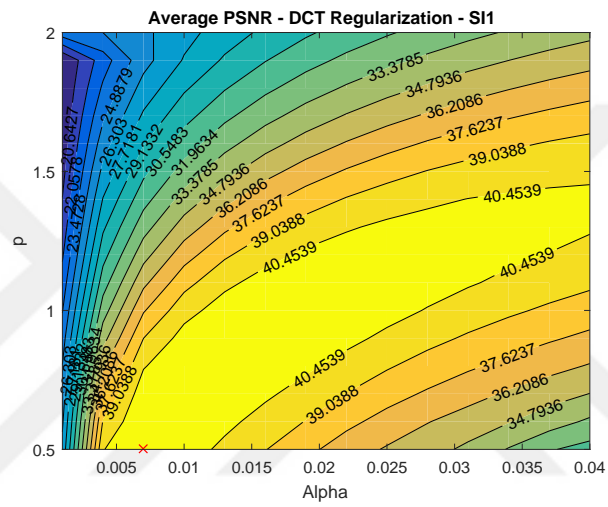
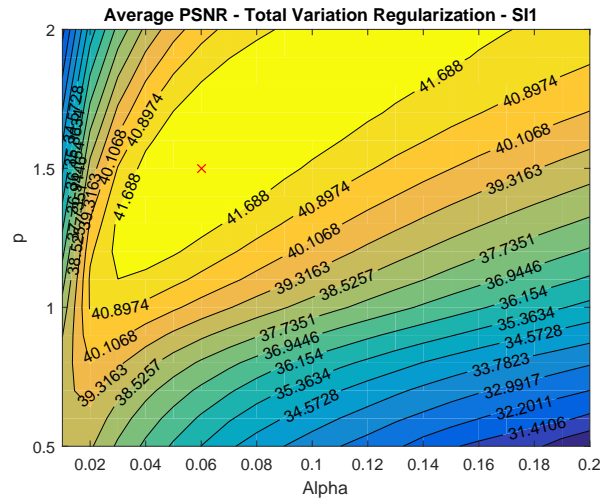


Figure 4.8: Reconstruction performance for different regularization operators and SI1 image pair.

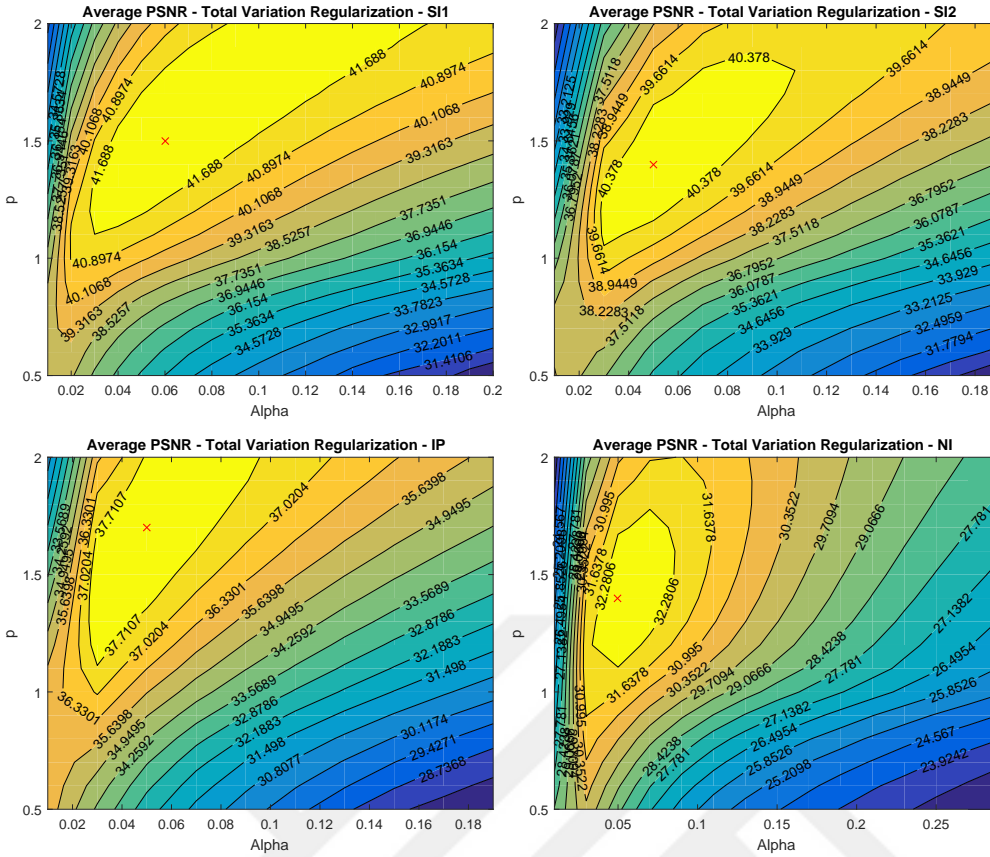


Figure 4.9: Reconstruction performance for different image pairs and DDO operator.

that  $\alpha = 0.05$  and  $p = 1.5$  appears to be nearly optimal regardless of the image pair used. This shows that optimal values of the regularization parameters are not sensitive to the underlying image pairs to be reconstructed.

Also note that, examining Fig. 4.9, one can conclude that the highest reconstruction quality for all regularization operators is that of SI1 image pair, which is the most similarly looking image pair. Moreover, results show that the lowest quality is obtained for NI image pair for all the regularization operators. However, the reconstruction performance of this poorly correlated image pair may not be representative for practical use since spectrally close bands often tend to yield similar 2-D intensities as in other pairs. Yet, the performance obtained for NI image pair is still useful since it can be interpreted as the worst-case performance.

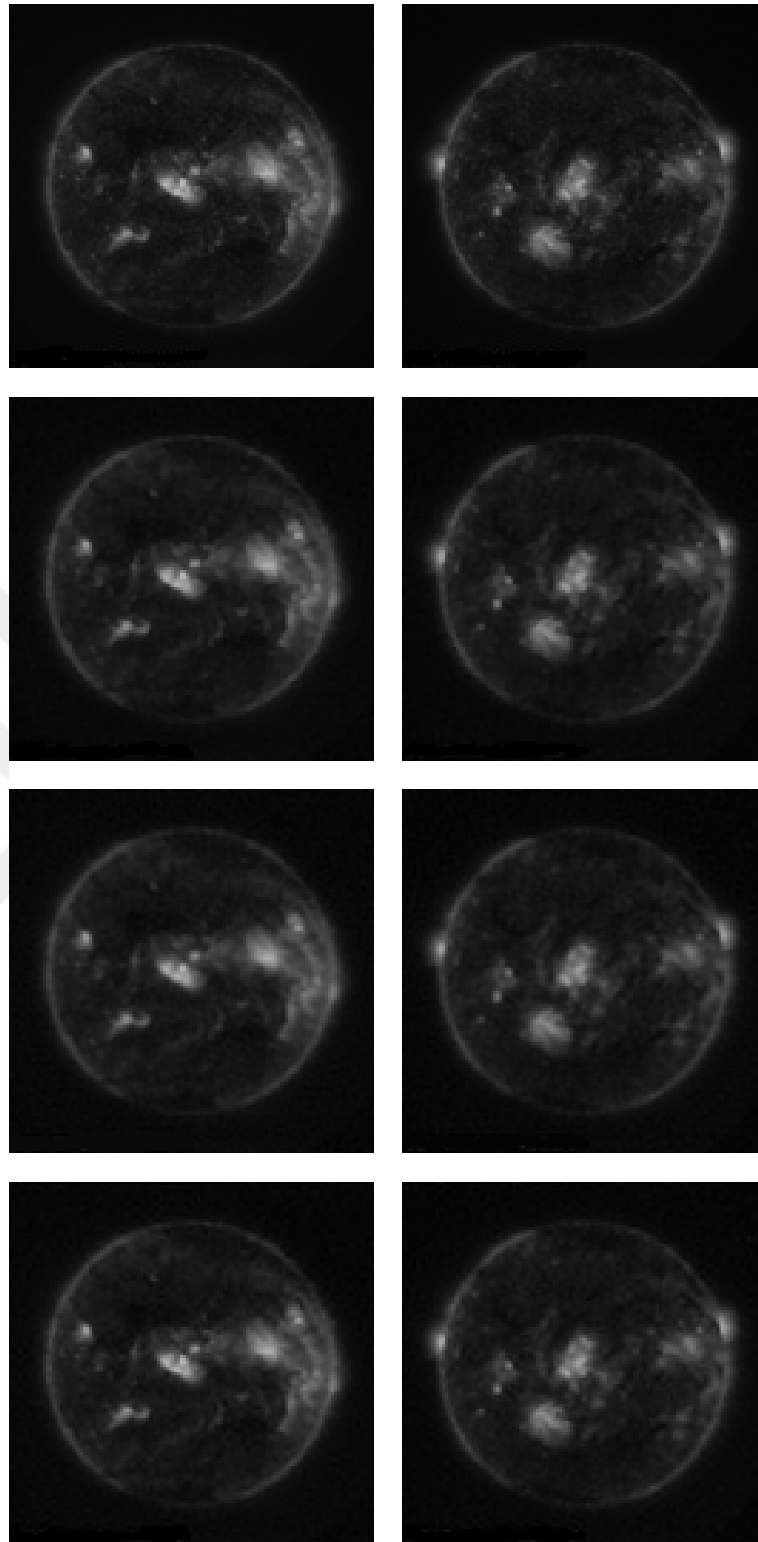


Figure 4.10: From top to bottom: Diffraction-limited S11 image pair, reconstructions with DDO, DCT and DWT operators for regularization.

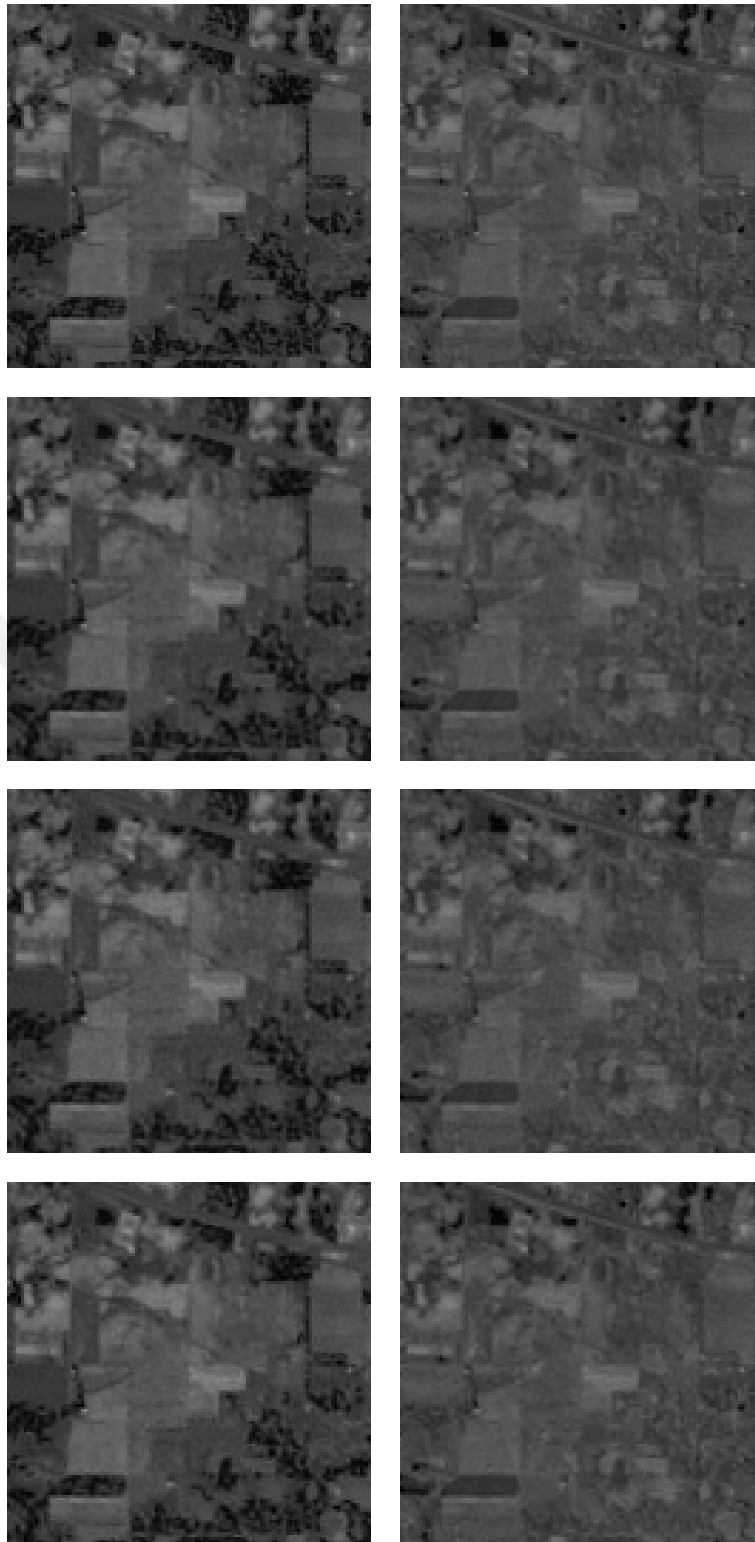


Figure 4.11: From top to bottom: Diffraction-limited IP image pair, reconstructions with DDO, DCT and DWT operators for regularization.



Figure 4.12: From top to bottom: Diffraction-limited NI image pair, reconstructions with DDO, DCT and DWT operators for regularization.

#### 4.4.2 Effect of Measurement Plane Locations

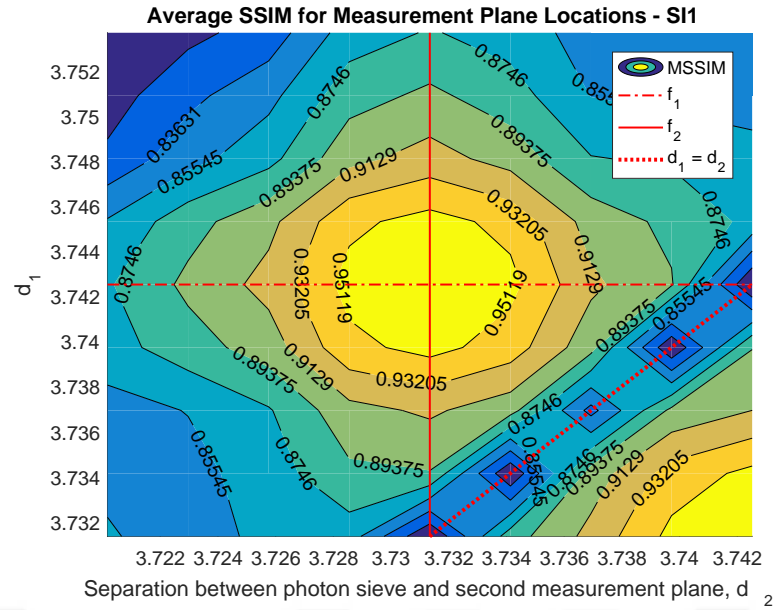
As described in Sect. 4.1, to reconstruct the spectral datacube, photon sieve imaging system takes multiple 2-D measurements that contain each spectral image with different focusing amount. An intuitive examination of this strategy yields a guess for the optimal locations of measurement planes as the focus of each wavelength of interest. The goal of the numerical test performed in this section is to verify this guess by analyzing the imaging performance for two sources as a function of the locations of two measurements to be acquired.

This reasonable guess is based on the fact that the relative amount of residual intensity from wavelengths other than the wavelength of interest is minimum when a measurement is taken from the focus for that particular wavelength. This observation is a direct result of the wavelength dependent focusing property of photon sieves. Yet, in practice, it may also not be possible to place the measurement planes at the exact focus of the wavelength to be imaged. Instead, a certain amount of known misplacement can be introduced when physically constructing the imaging system. Thus, the numerical test performed here will also illustrate how sensitive the reconstruction performance is to measurement locations.

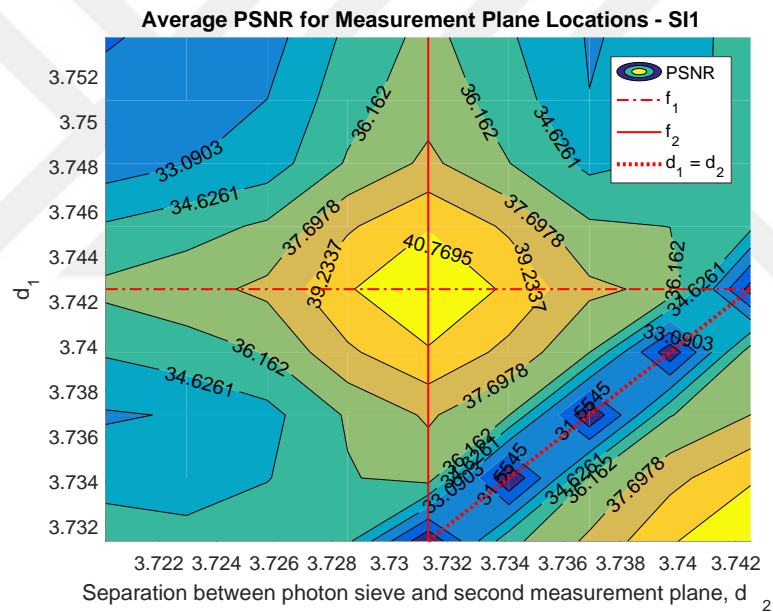
To evaluate the performance for different measurement plane distances,  $d_k$ , a numerical experiment is performed. By keeping the imaging setting same other than the measurement locations (such as same photon sieve design, input spectral composition and SNR), reconstructed images obtained from different measurements with DDO-based regularization are used to compute the reconstruction quality (i.e. SSIM and PSNR). Result for SI1 image pair is shown in Fig. 4.13 and results for all other image pairs are available in Appendix B. Note that all tests are performed for a regularization parameter set of ( $\alpha = \alpha_{optimal}, p = 1.3$ ), regularization operator of DDO, source wavelengths of  $\lambda_1 = 33.4$  and  $\lambda_2 = 33.5$  nm. Corresponding focal lengths for wavelengths  $\lambda_1$  and  $\lambda_2$  are 3.7425 and 3.7313 meters, and depth of foci (DOFs) are 1.497 and 1.493 millimetres.

Investigating Fig. 4.13, one can conclude that the reconstruction performance is maximized when the measurements are taken at the foci of the wavelengths of interest, as





(a)



(b)

Figure 4.13: Reconstruction performance for varying measurement plane locations,  $d_1$  and  $d_2$ , for SI1 image pair.

expected. In the bottom right portion of the image, the measurement planes are again in the foci of the wavelengths, hence same optimal performance is observed. Results show that a similar reconstruction performance can be obtained when the measure-

ment planes are placed within  $\pm 1$  DOF of foci. Also, as the dashed line labelled as  $d_1 = d_2$  demonstrates, the reconstruction quality significantly drops as the measurement planes get close to each other (Similar results for other image pairs are available in Appendix B).

#### 4.4.3 Effect of Measurement Noise

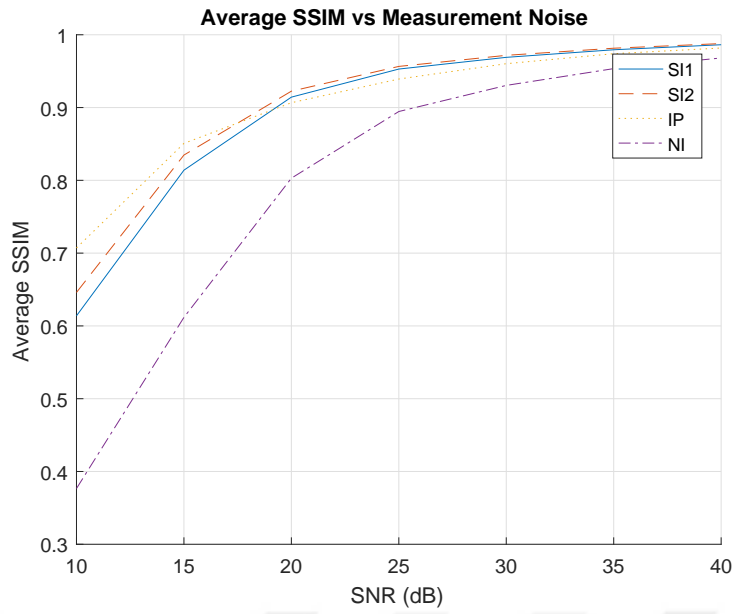
Another important design consideration for the studied spectral imaging modality is SNR. Aim of the reconstruction method is to reconstruct the individual images for each wavelength of interest in the presence of noise, blur, and the residuals from other bands. As given in Eqn. 4.2, observed total intensity at a measurement plane consists of contributions from all spectral bands of the scene. In theory, it is possible to obtain almost perfect reconstructions if the exact PSF for each contributing wavelength is known and the observations are noise-free. But in practice, all measurements are exposed to a certain amount of noise. The presence and amount of measurement noise on observations has a prominent effect on performance.

In this numerical experiment, the effect of SNR on image reconstruction quality is analyzed. To perform this analysis, the imaging setting is chosen as in previous sections. A Monte Carlo run with five different noise realizations are performed by using the optimal regularization parameters for each image pair. Then the reconstruction quality metrics are calculated and averaged over the five runs. The results for all four pairs of images are presented in Fig. 4.14. In addition, reconstructed images of SI1 and NI pairs for different levels of SNR are respectively shown in Figures 4.15 and 4.16.

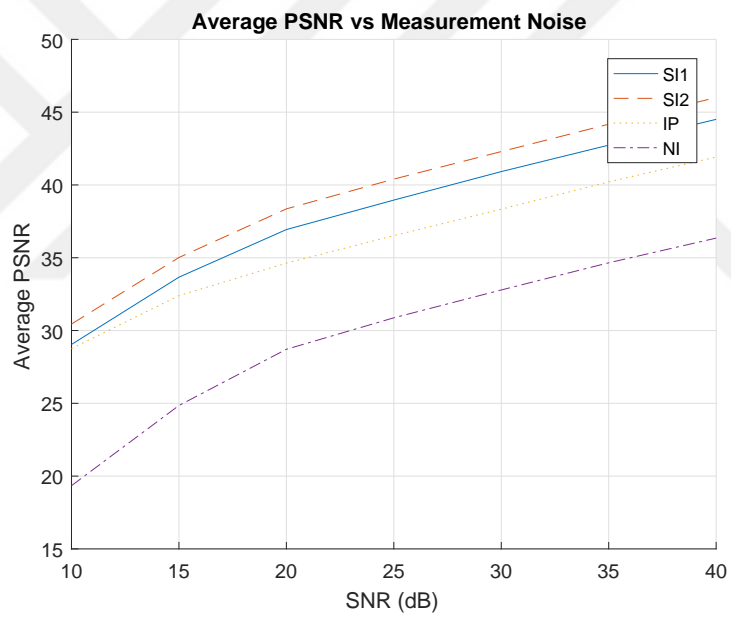
As expected, the reconstruction performance increases with the increased SNR. Yet, even for medium and medium-to-low SNR values as low as 15 dB, the reconstruction method still improves the observed images significantly.

#### 4.4.4 Effect of Number of Measurements

In this numerical experiment, the number of measurements,  $K$ , is increased while the number of sources is kept constant and the resulting observations are exposed to



(a)



(b)

Figure 4.14: Reconstruction performance (a) in SSIM and (b) in PSNR for varying SNR levels for SI1, SI2, IP and NI image pairs.

different levels of SNR. The aim of this study is to determine how much improvement is achieved in the reconstructions with additional measurements.

Increasing the number of measurements in this experiment corresponds to taking ob-

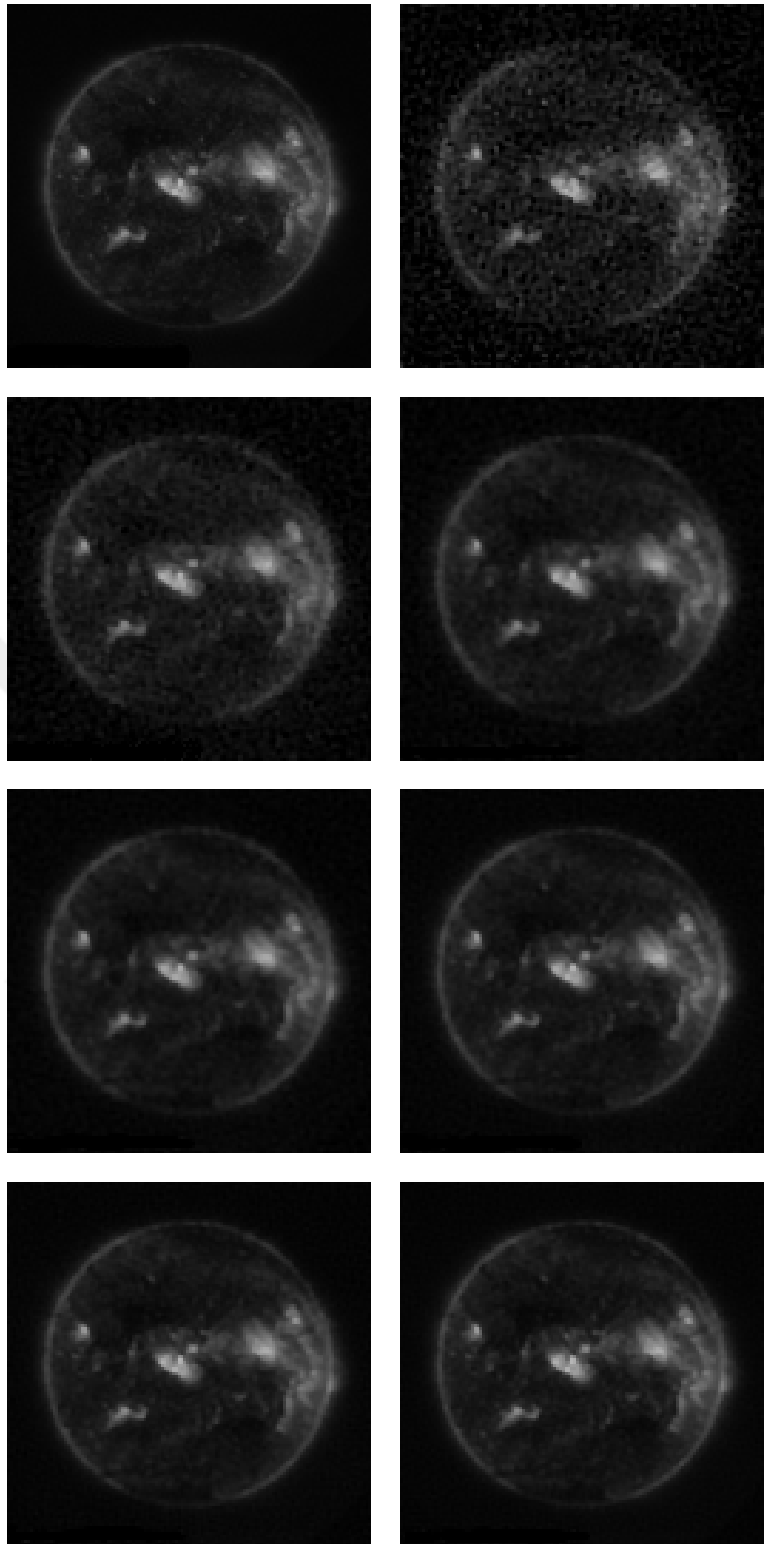


Figure 4.15: Top left: First diffraction-limited intensity image of SII pair. Rest from left to right and top to bottom: Reconstructed images for a measurement noise with SNR values of 10, 15, 20, 25, 30, 35 and 40 dB.



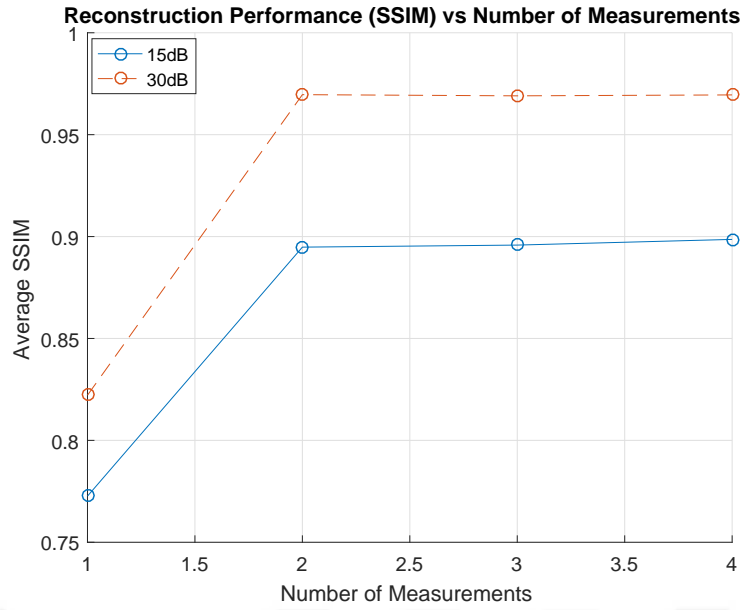
Figure 4.16: Top left: First diffraction-limited intensity image of NI pair. Rest from left to right and top to bottom: Reconstructed images for a measurement noise with SNR values of 10, 15, 20, 25, 30, 35 and 40 dB.

servations from equally spaced measurement planes between the two focal planes,  $f_1$  and  $f_2$ , corresponding to the wavelengths,  $\lambda_1$  and  $\lambda_2$ . For instance, for the case of three measurements, the separations of the measurement planes from the photon sieve plane are  $f_1$ ,  $(f_1 + f_2)/2$  and  $f_2$ . A special case is the case of  $K = 1$ ; in this case, the reconstruction is performed using a single observation taken from the distance of  $(f_1 + f_2)/2$ . Results for this numerical experiment are presented in Fig. 4.17 for the S11 image pair and two different SNR levels of 15 and 30 dB using 5 Monte Carlo trials, while the source wavelengths are kept as 33.4 and 33.5 nm.

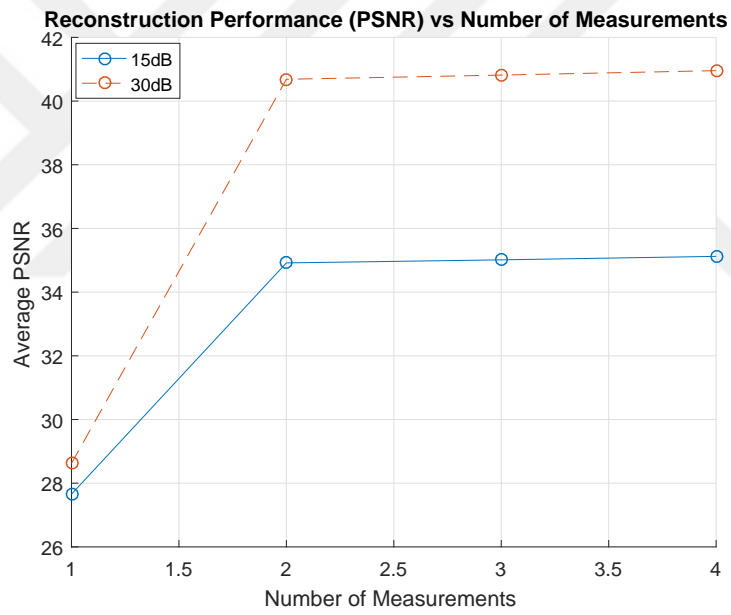
Examination of Fig. 4.17 shows that the reconstructions are only marginally improved when the number of measurements are increased more than two. Hence one can conclude that for both low and high SNR cases taking two measurements is sufficient and additional measurements do not worth the cost. On the other hand, for the case with a single measurement taken between the two focal planes, the reconstruction performance is poor. Further examination of the reconstructed images for  $K = 1$  case, as given in Fig. 4.18, reveals that the reconstructed images for the distinct wavelengths appear to be similar; hence the spectral imaging technique fails to separate the two spectral components with a single measurement taken between the focal planes. This is because the PSFs acting on the two spectral components are almost the same at this distance of  $(f_1 + f_2)/2$ . An additional experiment is performed for this case by taking the single measurement either at  $f_1$  or  $f_2$ . As can be seen in Fig. 4.17, although the spectral imaging technique still fails in these cases in terms of reconstructing both spectral images, it can at least recover one of the spectral images (the one associated with the focal plane that the measurement is taken).

#### 4.4.5 Effect of Spectral Separation

One of the important features of the spectral imaging technique with photon sieves is the improved spectral resolution. As mentioned in Sect. 4.4, in all the previous tests, the numerical experimental setup is constructed such that there are two sources of radiation with wavelengths 33.4 and 33.5 nm. This corresponds to a spectral resolution of 0.1 nm and a physical separation of 11.2 mm between the foci of sources or equivalently a separation of 7.4 DOF from the focus of each source. In this experiment, the



(a)



(b)

Figure 4.17: Reconstruction performance (a) in SSIM and (b) in PSNR for varying number of observations.

effect of spectral separation between two sources will be analyzed by varying  $\lambda_1$  that was fixed to 33.4 nm earlier and keeping  $\lambda_2$  constant at 33.5 nm.

As the spectral separation between the two sources is decreased, the corresponding

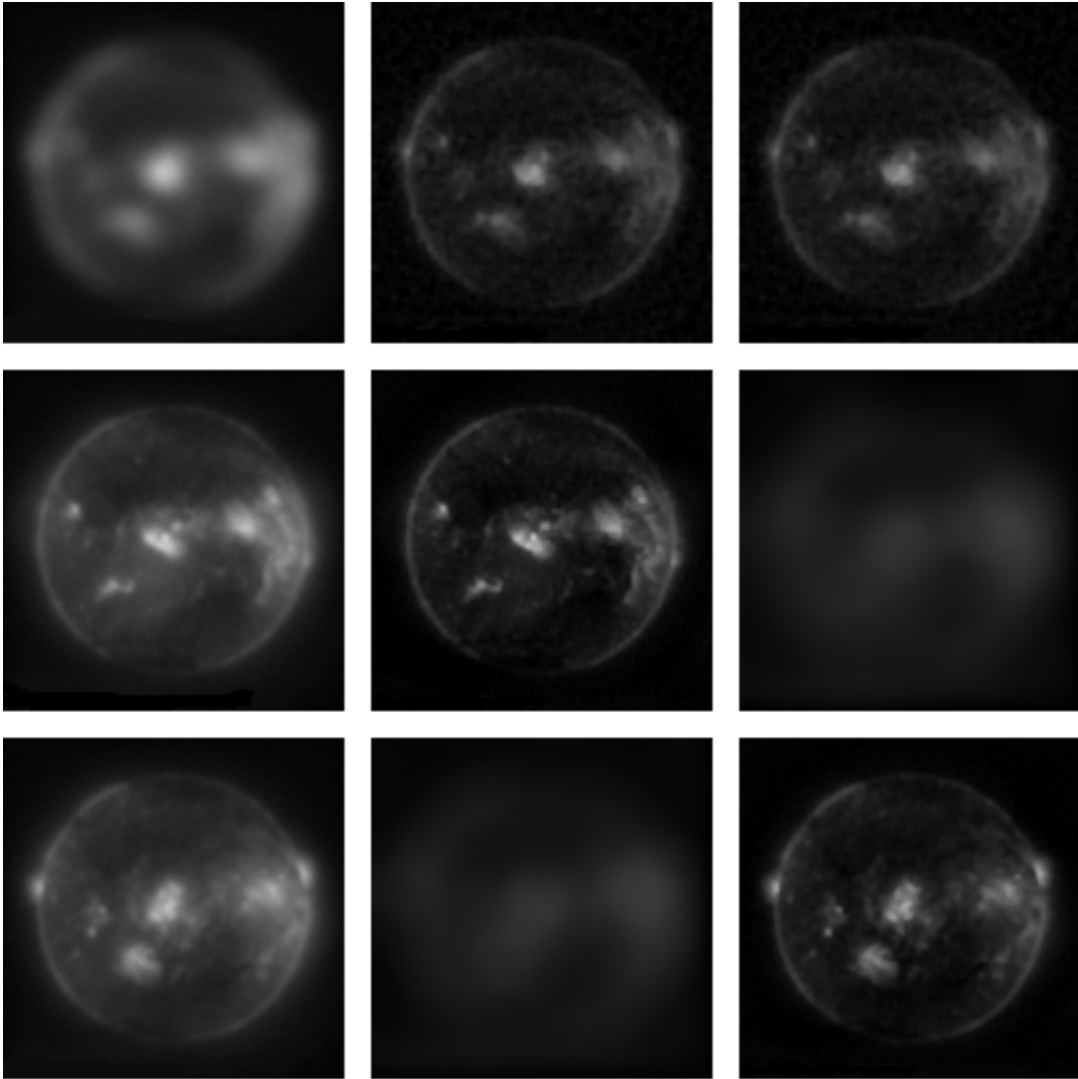


Figure 4.18: Reconstructed images obtained with a single measurement and SNR=30 dB. Top row from left to right: single measurement taken at  $(f_1 + f_2)/2$ , reconstructed images for the first and second wavelengths. Middle row from left to right: single measurement taken at  $f_1$ , reconstructed images for the first and second wavelengths. Bottom row from left to right: single measurement taken at  $f_2$ , reconstructed images for the first and second wavelengths.



foci of distinct sources get closer to each other. This gradually degrades the image reconstruction performance as the similarity between two observations is increased, as also discussed in Section 4.4.2. In this experiment, the performance of reconstruction is numerically investigated for varying spectral separation between sources. The results for this numerical experiment are presented in Fig. 4.19.

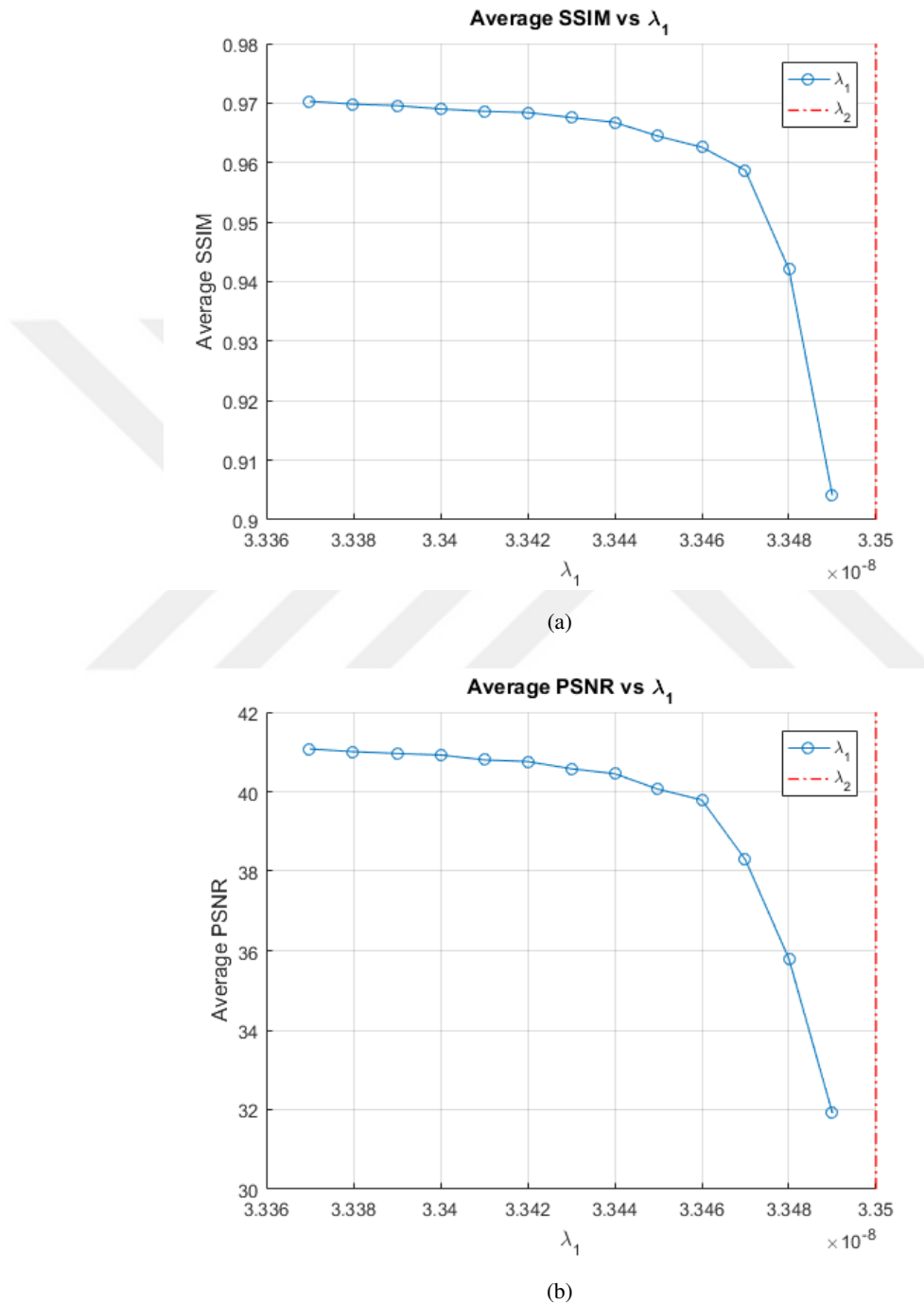


Figure 4.19: Reconstruction performance for varying  $\lambda_2$  and for SI1 pair of images.

$\lambda_2$ (nm)	33.37	33.38	33.39	33.40	33.41	33.42	33.43	33.44	33.45	33.46	33.47	33.48	33.49
Dist. between Foci ( $DOF_2$ )	9.7	9.0	8.2	7.5	6.7	6.0	5.2	4.5	3.7	3.0	2.2	1.5	0.7

Table 4.2: Changing separation between the foci of wavelengths in terms of DOF of  $\lambda_2$ .

Results show that it is possible to obtain good reconstructions even for when  $\lambda_1 = 33.48$  and  $\lambda_2 = 33.5$  nm, corresponding to a spectral resolution of 0.02 nm. To understand the significance of this result, consider the corresponding separations between the foci of different wavelengths in terms of DOF of the second source, as presented in Table 4.2. Investigating Table 4.2, one can observe that good reconstructions can be achieved even when the focus of the second source is only one DOF away from the focus of the first source. In practice, this result corresponds to a relative spectral bandpass of  $(33.5 - 33.48)/33.5 = 5.97 \times 10^{-4}$ . One can conclude that a spectral resolution of 0.02 nm is achievable with this modality; that is, photon sieve spectral imaging technique can resolve radiation from spectral components that are as close as 0.02 nm in wavelength within the proximity of 33.5 nm. This spectral resolution is more than two orders of magnitude higher than what can be achieved with the current state-of-the-art spectral imaging technology.

## CHAPTER 5

### CONCLUSIONS

Spectral imaging is an important diagnostic tool for a wide-variety of applications such as remote sensing, physics, chemistry, biology, and medicine. Although the field has been an active research area for a considerably long time, new imaging modalities that offer higher performance and flexibility are still of interest as the applications in science and engineering grow rapidly. Inevitably all optics-based techniques suffer from the physical limitations inherent in their optical components and face the difficulty of acquiring the three-dimensional spectral data set with the intrinsically two-dimensional detectors. Increasingly demanding considerations such as spatial, spectral and time resolution, as well as optical throughput push the efforts on the field to go beyond its physical limits, and thus keep the century and a half year old field still an active area of research.

In this study, a recently developed computational spectral imaging technique with photon sieves is analyzed both numerically and experimentally. This technique offers unprecedented spatial and spectral resolution for scenes with discrete spectrum compared to the conventional techniques, while requiring only a light-weight and low-cost imaging system. The technique is of particular importance in the EUV and x-rays since at these short wavelengths alternative spectral imaging techniques have strong physical limitations.

In this thesis, a detailed up-to-date survey of existing spectral imaging techniques is presented. Moreover, a fast and accurate method is developed to compute the two-dimensional point-spread function of diffractive imaging elements and is also experimentally validated. A compact, cheap and versatile experimental setup is also built

for the photon sieve imaging system, and PSF measurements taken with this setup are used to validate the theoretical forward models. Lastly, computational image reconstruction method of the photon sieve spectral imager is described and the performance of the reconstruction method is evaluated for different regularization operators and under different practical scenarios of interest to determine the practical capabilities and limits of the approach.

Developed PSF computation method accurately obtains the 2-D PSF of a photon sieve as well as any diffractive imaging element with a given aperture function. While the previously developed methods for this purpose have high computational cost and are only applicable to certain diffractive elements, the developed method is an FFT-based fast method with significantly lower computational complexity, and is general enough that it can be used for any photon sieve configuration, as well as for any other diffractive imaging element such as Fresnel lenses and their modifications, and any other mask-like patterns including coded apertures.

Constructed experimental setup is intended to be a versatile and cheap prototype for the photon sieve imaging system. In fact, since a programmable DMD is used, the system can realize any binary diffractive imaging device. The 2-D measurements for the PSF of a photon sieve obtained with this experimental setup show strong agreement with theory and serve as a proof of concept for the DMD-based photon sieve system.

Besides the analysis of focusing properties of the photon sieve system, image reconstruction method used with photon sieve spectral imager is also examined in this study. Starting with the formulations of the forward and inverse problems, details of a fast numerical algorithm for solving the inverse problem, which is specialized to this imaging modality, is described. Then, using this algorithm, the image reconstruction performance is evaluated for this computational imaging modality under the scenarios of different regularization operators and parameters as well as varying number of observations, amount of measurement noise, measurement plane locations and spectral composition of the scene.

The discrete derivative operator is shown to be the optimal choice for the regularization operator in the  $\ell_p$ -norm based regularization. It is also observed that good re-

constructions are possible even with medium and medium-to-low SNR values. This observation is important in practice in the design of the imaging system since this will determine the exposure time. Two other important design parameters are the number of measurements to take and the locations of these measurement planes. Numerical results suggest that it is sufficient to take as many measurements as the number of spectral components. Moreover, the optimal locations for the measurements are found to be at the focal planes of the corresponding wavelengths of interest. Another numerical experiment of this study is related to the spectral separation of sources. It is observed, for the considered EUV solar imaging application, that the spectral resolution achievable with the photon sieve spectral imager is more than two orders of magnitude higher than what can be achieved with the current state-of-the-art spectral imaging technology.

## **5.1 Future Work**

As a future work, the constructed experimental setup for PSF measurement is planned to be used for the practical demonstration of the photon sieve spectral imager. Also, we intent to improve the success of the reconstruction method by using data-adaptive regularization methods.



## APPENDIX A

### RECONSTRUCTION PERFORMANCE FOR DIFFERENT REGULARIZATION PARAMETERS

In the following figures, the image reconstruction performance of the spectral imaging modality is presented for different image pairs, regularization parameter pairs,  $(\lambda, p)$ , and regularization operators. Note that the values of the optimal regularization parameters are marked with a red cross in each of the figures.

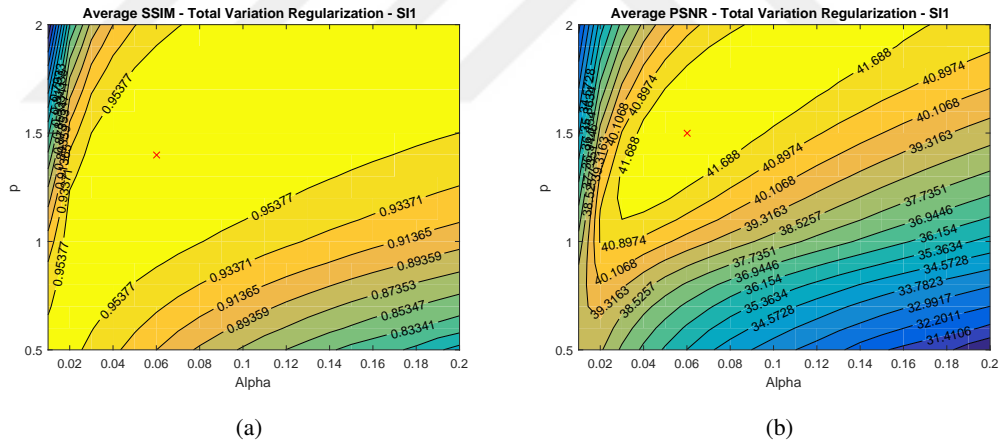
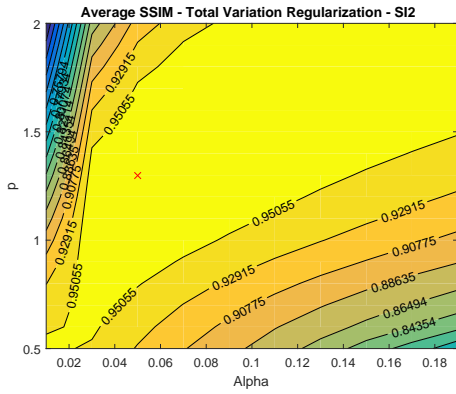
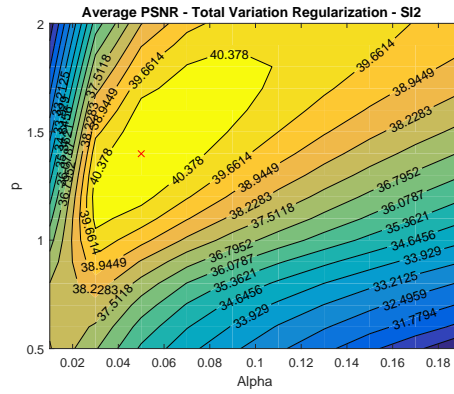


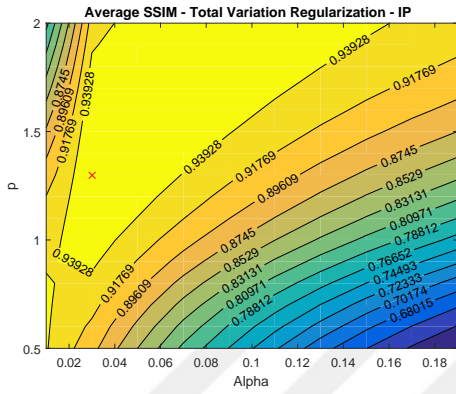
Figure A.1: Reconstruction performance for regularization with DDO operator and for S11 image pair where the left column shows the results in SSIM metric and the right column in PSNR.



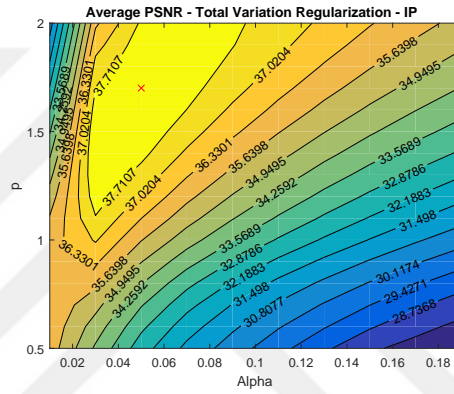
(a)



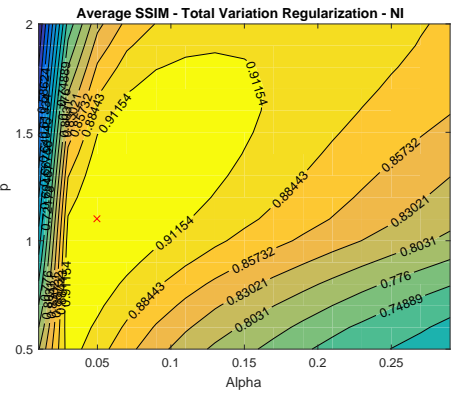
(b)



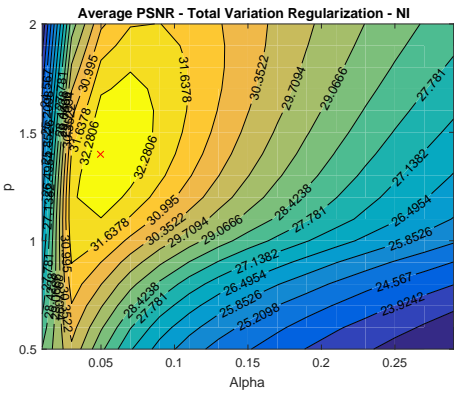
(c)



(d)



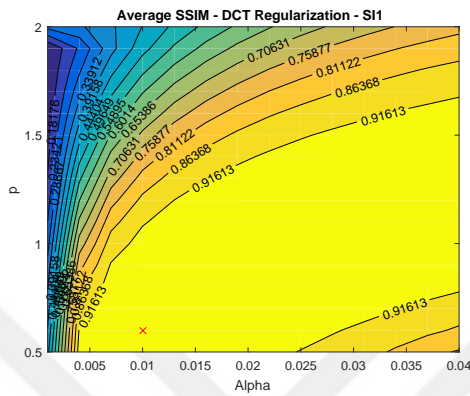
(e)



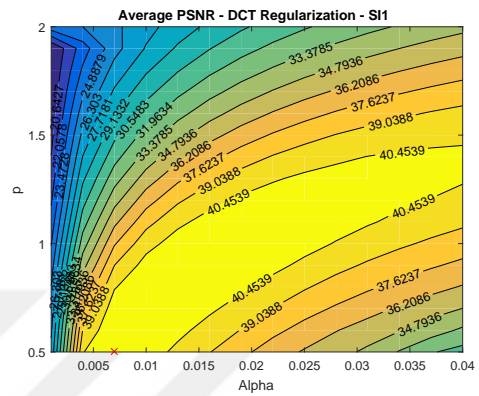
(f)

Figure A.2: Reconstruction performance for regularization with DDO operator. From top to bottom: SI2, IP and NI image pairs where the left column shows the result in SSIM metric and right column in PSNR.

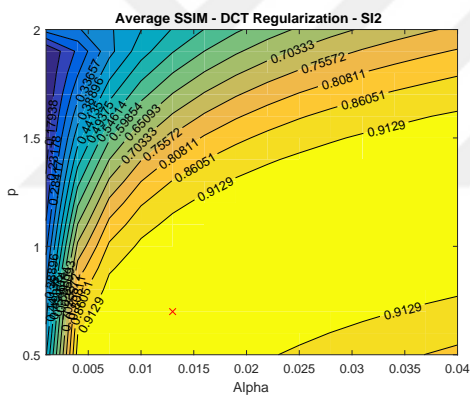




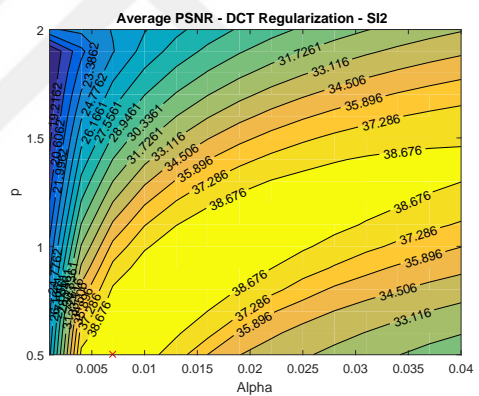
(a)



(b)



(c)



(d)

Figure A.3: Reconstruction performance for regularization with DCT operator. Top row for SI1 image pair and bottom is for SI2 where the left column shows the results in SSIM metric and right column in PSNR.

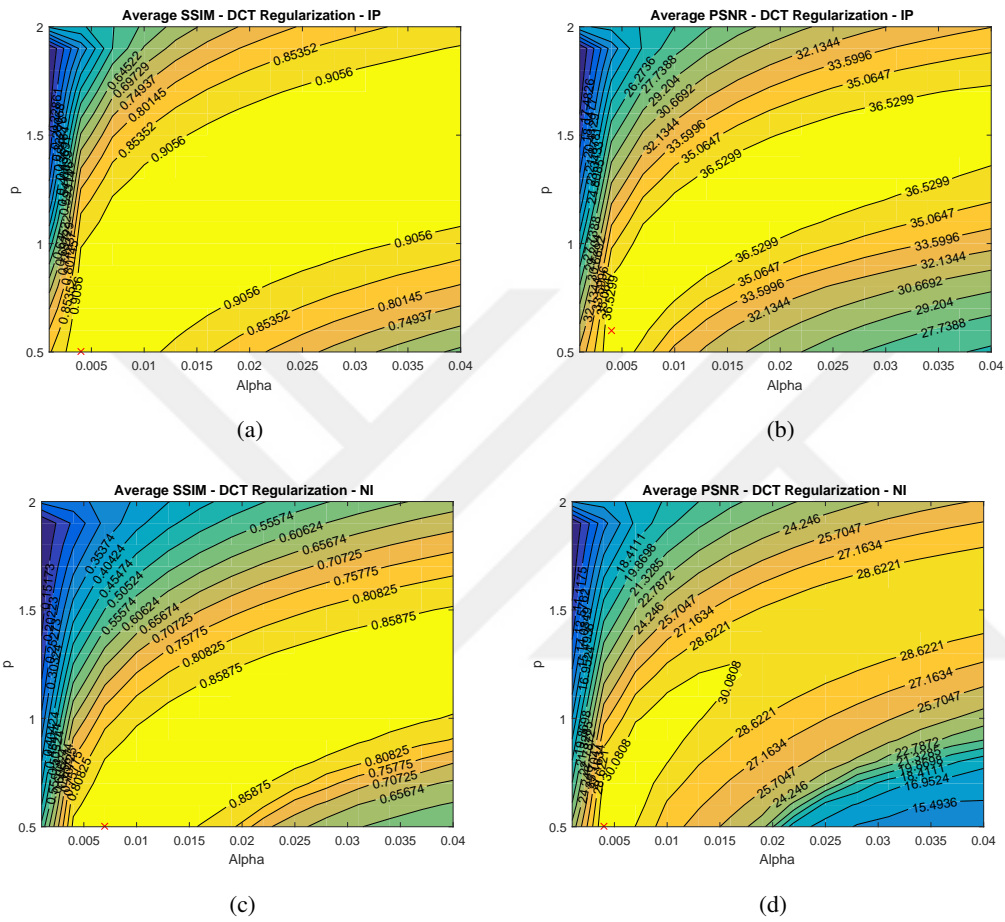
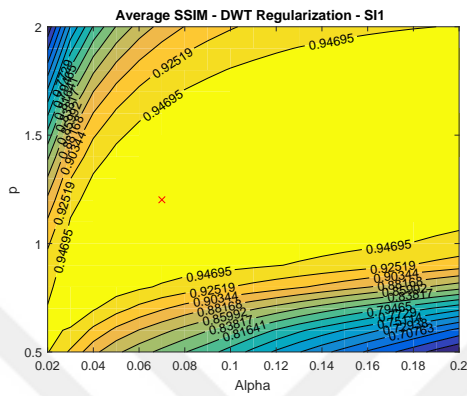
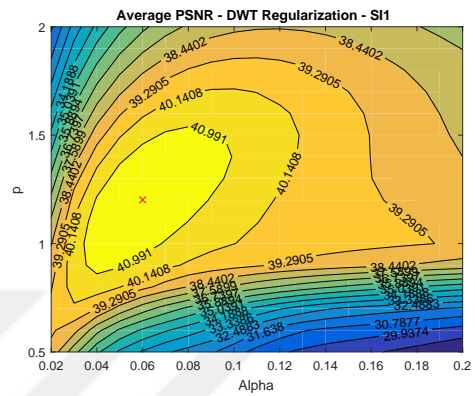


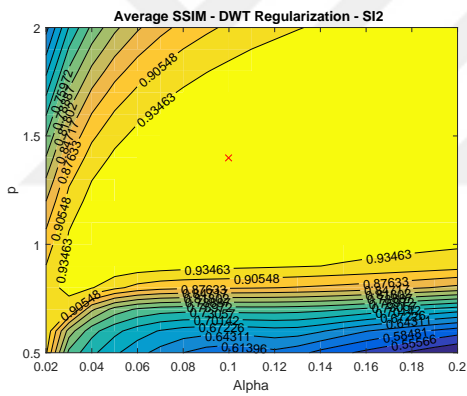
Figure A.4: Reconstruction performance for regularization with DCT operator. Top row for IP image pair and bottom is for NI where the left column shows the performance in SSIM metric and the right column in PSNR.



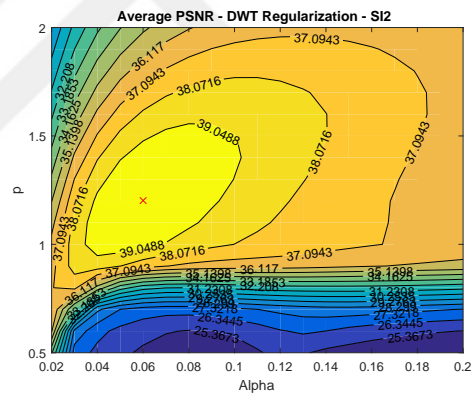
(a)



(b)



(c)



(d)

Figure A.5: Reconstruction performance for regularization with DWT operator. Top row for SI1 image pair and bottom is for SI2 where the left column shows the performance in SSIM metric and the right column in PSNR.

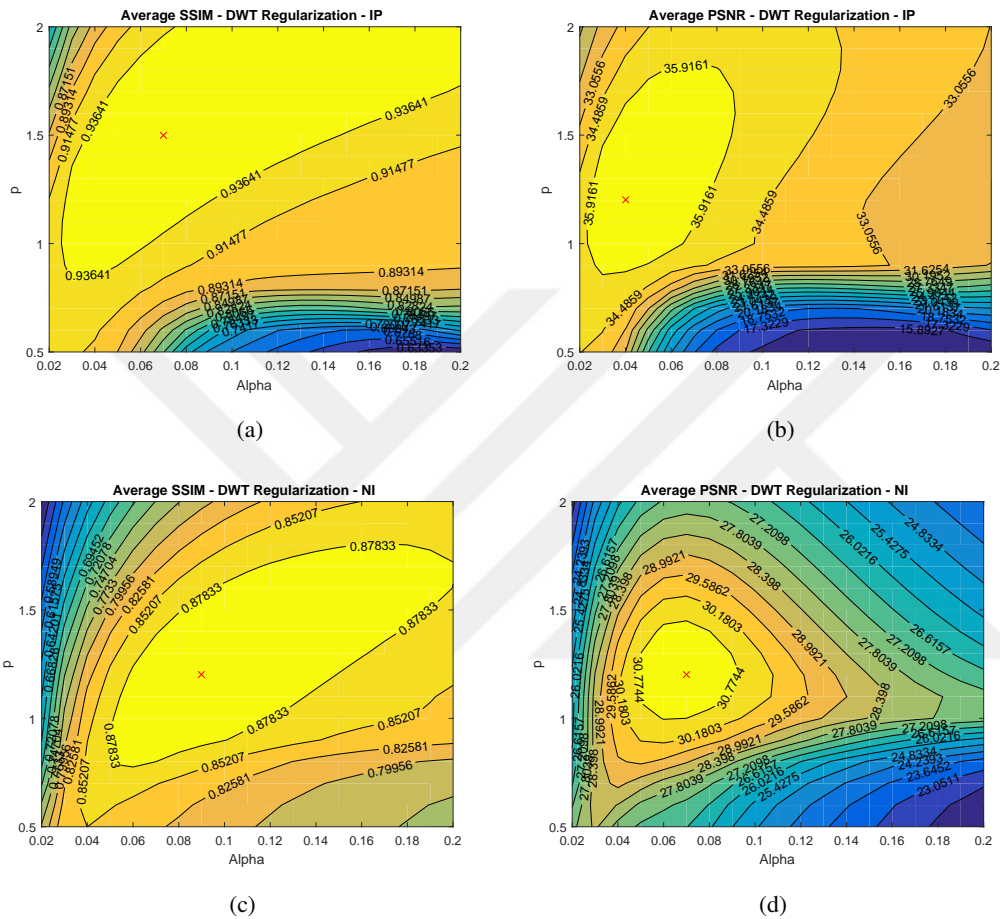


Figure A.6: Reconstruction performance for regularization with DWT operator. Top row for IP image pair and bottom is for NI where the left column shows the performance in SSIM metric and the right column in PSNR.

## APPENDIX B

### RECONSTRUCTION PERFORMANCE FOR DIFFERENT MEASUREMENT PLANE LOCATIONS

In the following figures, the image reconstruction performance of the photon sieve spectral imager is evaluated for varied measurement plane locations considering different image pairs and reconstruction quality metrics.

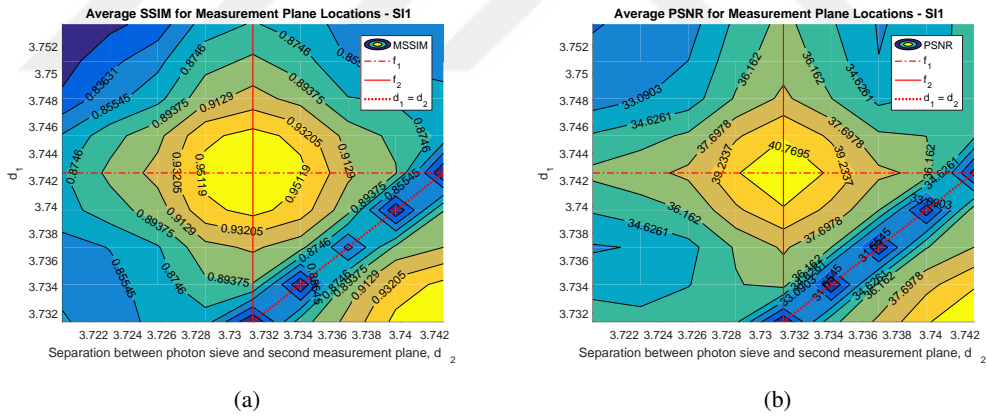
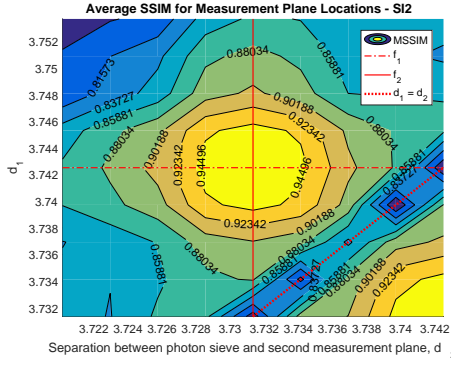
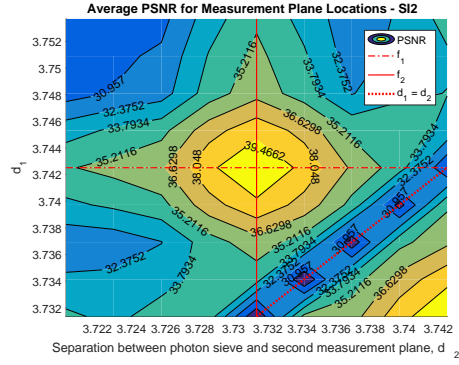


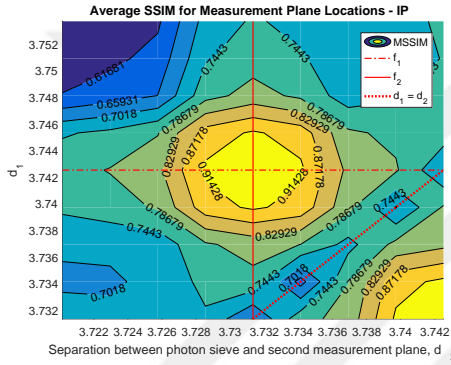
Figure B.1: Reconstruction performance for varying measurement plane locations,  $d_1$  and  $d_2$ , for SI1 image pair where left column is the performance in SSIM metric and right column is in PSNR.



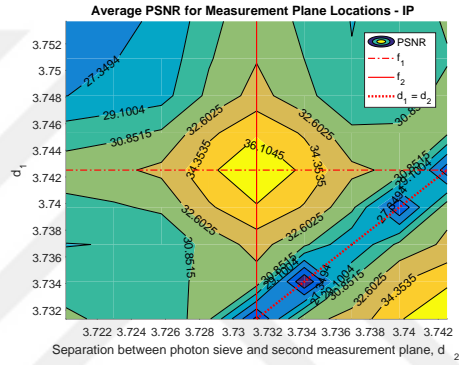
(a)



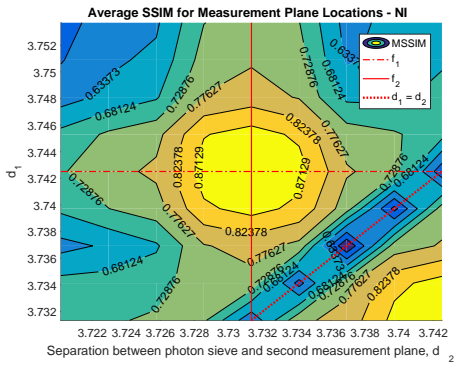
(b)



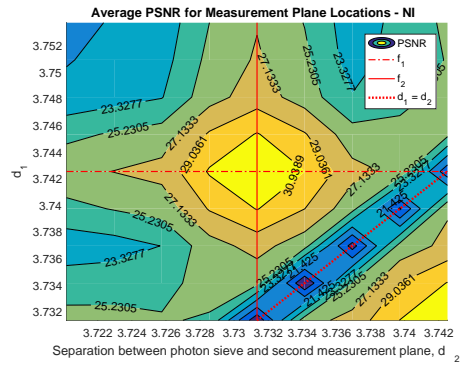
(c)



(d)



(e)



(f)

Figure B.2: Reconstruction performance for varying measurement plane locations,  $d_1$  and  $d_2$ , for SI2, IP and NI image pairs, from top to bottom. Left column is the performance in SSIM metric and right column is in PSNR.

## REFERENCES

- [1] “Hyperspectral imaging.” [https://en.wikipedia.org/wiki/Hyperspectral\\_imaging](https://en.wikipedia.org/wiki/Hyperspectral_imaging). Accessed: 2016-09-16.
- [2] N. Hagen and M. W. Kudenov, “Review of snapshot spectral imaging technologies,” *Optical Engineering*, vol. 52, no. 9, 2013.
- [3] “Angular resolution.” [https://en.wikipedia.org/wiki/Angular\\_resolution](https://en.wikipedia.org/wiki/Angular_resolution). Accessed: 2016-08-27.
- [4] “Fundamentals and applications in multiphoton excitation microscopy.” <http://www.microscopyu.com/techniques/multi-photon/multiphoton-microscopy>. Accessed: 2016-08-27.
- [5] Q. Li, X. He, Y. Wang, H. Liu, D. Xu, and F. Guo, “Review of spectral imaging technology in biomedical engineering: Achievements and challenges,” *Journal of Biomedical Optics*, vol. 18, no. 10, 2013.
- [6] F. S. Oktem, F. Kamalabadi, and J. M. Davila, “High-resolution computational spectral imaging with photon sieves,” in *2014 IEEE International Conference on Image Processing (ICIP)*, pp. 5122–5126, IEEE, 2014.
- [7] F. S. Oktem and T. Alkanat, “Fast computation of two-dimensional point-spread functions for photon sieves,” in *3D Image Acquisition and Display: Technology, Perception and Applications*, pp. JT3A–34, Optical Society of America, 2016.
- [8] “DLP6500FYE 0.65 1080p MVSP S600 DMD,” tech. rep., Texas Instruments, 2016.
- [9] B. Lee, “System design considerations using TI DLP technology: Down to 400 nm,” tech. rep., Texas Instruments, 2014.
- [10] I. Asimov and J. A. Shulman, *Isaac Asimov’s book of science and nature quotations*. Weidenfeld & Nicolson, 1988.
- [11] P. Janssen, “Sur la methode qui permet de constater la matiere protuberantielle sur tout le contour du disque solaire [On a method to see the entire solar corona],” *Comptes Rendus Acad. Sci*, vol. 68, pp. 713–715, 1869.
- [12] C. Fabry and A. Perot, “Sur les franges des lames minces argentees et leur application a la mesure de petites epaisseurs dair,” *Ann. Chim. Phys*, vol. 12, pp. 459–501, 1897.

- [13] P. Hariharan, *Basics of interferometry*. Academic Press, 2010.
- [14] P. Mouroulis and M. M. McKerns, “Pushbroom imaging spectrometer with high spectroscopic data fidelity: Experimental demonstration,” *Optical Engineering*, vol. 39, no. 3, pp. 808–816, 2000.
- [15] I. Bowen, “The image-slicer: A device for reducing loss of light at slit of stellar spectrograph.,” *The Astrophysical Journal*, vol. 88, p. 113, 1938.
- [16] J. T. Meade, B. B. Behr, and A. R. Hajian, “A new high-resolution, high-throughput spectrometer: First experience as applied to Raman spectroscopy,” in *SPIE Defense, Security, and Sensing*, International Society for Optics and Photonics, 2012.
- [17] T. Walraven and J. Walraven, “Some features of the leiden radial velocity instrument.,” in *Auxiliary Instrumentation for Large Telescopes*, pp. 175–183, 1972.
- [18] S. D’Odorico, G. Avila, and P. Molaro, “More light through the fibre: An upgrading of the link 3.6 m-CES.,” *The Messenger*, vol. 58, pp. 58–60, 1989.
- [19] G. Avila, C. Guirao, and T. Baader, “High efficiency inexpensive 2-slices image slicers,” in *SPIE Astronomical Telescopes+ Instrumentation*, International Society for Optics and Photonics, 2012.
- [20] F. Diego, “Confocal image slicer,” *Applied Optics*, vol. 32, no. 31, pp. 6284–6287, 1993.
- [21] H. Matsuoka, Y. Kosai, M. Saito, N. Takeyama, and H. Suto, “Single-cell viability assessment with a novel spectro-imaging system,” *Journal of Biotechnology*, vol. 94, no. 3, pp. 299–308, 2002.
- [22] N. Kapany, “A light funnel for stellar spectrograph,” in *Astronomical Optics and Related Subjects*, vol. 1, p. 288, 1956.
- [23] D. W. Fletcher-Holmes and A. R. Harvey, “Real-time imaging with a hyperspectral fovea,” *Journal of Optics A: Pure and Applied Optics*, vol. 7, no. 6, p. S298, 2005.
- [24] J. Baudrand and G. A. Walker, “Modal noise in high-resolution, fiber-fed spectra: A study and simple cure,” *Publications of the Astronomical Society of the Pacific*, vol. 113, no. 785, p. 851, 2001.
- [25] N. Gat, G. Scriven, J. Garman, M. De Li, and J. Zhang, “Development of four-dimensional imaging spectrometers (4D-IS),” in *SPIE Optics+ Photonics*, International Society for Optics and Photonics, 2006.
- [26] J. Kriesel, G. Scriven, N. Gat, S. Nagaraj, P. Willson, and V. Swaminathan, “Snapshot hyperspectral fovea vision system (HyperVideo),” in *SPIE Defense, Security, and Sensing*, International Society for Optics and Photonics, 2012.



- [27] G. Courtes, “Méthodes d’observation et étude de l’hydrogène interstellaire en émission,” in *Annales d’Astrophysique*, vol. 23, p. 115, 1960.
- [28] J. Larkin, M. Barczys, A. Krabbe, S. Adkins, T. Aliado, P. Amico, G. Brims, R. Campbell, J. Canfield, T. Gasaway, *et al.*, “OSIRIS: A diffraction limited integral field spectrograph for Keck,” *New Astronomy Reviews*, vol. 50, no. 4, pp. 362–364, 2006.
- [29] G. Courtes, Y. Georgelin, R. Bacon, G. Monnet, and J. Boulesteix, “A new device for faint objects high resolution imagery and bidimensional spectrography,” in *Instrumentation for Ground-Based Optical Astronomy*, pp. 266–274, Springer, 1988.
- [30] L. Gao, R. T. Kester, and T. S. Tkaczyk, “Compact image slicing spectrometer (ISS) for hyperspectral fluorescence microscopy,” *Optics Express*, vol. 17, no. 15, pp. 12293–12308, 2009.
- [31] J. Stoffels, A. A. J. Bluekens, and J. M. P. Petrus, “Color splitting prism assembly,” Apr. 11 1978. US Patent 4,084,180.
- [32] B. Ozeki, “Prism system for use in tricolor separation,” Feb. 7 1978. US Patent 4,072,405.
- [33] C. Mead, “Color separation prisms having solid-state imagers mounted thereon and camera employing same,” Sept. 2 2003. US Patent 6,614,478.
- [34] D. Basiji and W. Ortyń, “Imaging and analyzing parameters of small moving objects such as cells,” June 19 2001. US Patent 6,249,341.
- [35] S. E. Headland, H. R. Jones, A. S. D’Sa, M. Perretti, and L. V. Norling, “Cutting-edge analysis of extracellular microparticles using imagestreamx imaging flow cytometry,” *Scientific Reports*, vol. 4, 2014.
- [36] J. Beale, A. Harvey, and D. Fletcher-Holmes, “Imaging spectrometer including a plurality of polarizing beam splitters,” Oct. 21 2008. US Patent 7,440,108.
- [37] A. R. Harvey, D. W. Fletcher-Holmes, A. Gorman, K. Altenbach, J. Arlt, and N. D. Read, “Spectral imaging in a snapshot,” in *Biomedical Optics 2005*, pp. 110–119, International Society for Optics and Photonics, 2005.
- [38] A. R. Harvey and D. W. Fletcher-Holmes, “High-throughput snapshot spectral imaging in two dimensions,” in *Biomedical Optics 2003*, pp. 46–54, International Society for Optics and Photonics, 2003.
- [39] I. Baldry and J. Bland-Hawthorn, “A tunable echelle imager,” *Publications of the Astronomical Society of the Pacific*, vol. 112, no. 774, p. 1112, 2000.

- [40] A. Chalabaev, E. Le Coarer, P. Rabou, Y. Magnard, P. Petmezakis, and D. Le Mignant, “The GraF instrument for imaging spectroscopy with the adaptive optics,” *Experimental Astronomy*, vol. 14, no. 3, pp. 147–181, 2002.
- [41] Z. Malacara and M. Servin, *Interferogram analysis for optical testing*, vol. 84. CRC press, 2016.
- [42] M. W. Kudenov and E. L. Dereniak, “Compact snapshot birefringent imaging Fourier transform spectrometer,” in *SPIE Optical Engineering+ Applications*, International Society for Optics and Photonics, 2010.
- [43] L. Gao and L. V. Wang, “A review of snapshot multidimensional optical imaging: Measuring photon tags in parallel,” *Physics Reports*, vol. 616, pp. 1–37, 2016.
- [44] M. W. Kudenov and E. L. Dereniak, “Compact real-time birefringent imaging spectrometer,” *Optics Express*, vol. 20, no. 16, pp. 17973–17986, 2012.
- [45] R. Shogenji, Y. Kitamura, K. Yamada, S. Miyatake, and J. Tanida, “Multispectral imaging using compact compound optics,” *Optics Express*, vol. 12, no. 8, pp. 1643–1655, 2004.
- [46] T. Okamoto and I. Yamaguchi, “Simultaneous acquisition of spectral image information,” *Optics Letters*, vol. 16, no. 16, pp. 1277–1279, 1991.
- [47] T. V. Bulygin and G. N. Vishnyakov, “Spectrotomography: A new method of obtaining spectrograms of two-dimensional objects,” in *Analytical Methods for Optical Tomography*, pp. 315–322, International Society for Optics and Photonics, 1992.
- [48] J. M. Mooney, “Angularly multiplexed spectral imager,” in *SPIE’s 1995 Symposium on OE/Aerospace Sensing and Dual Use Photonics*, pp. 65–77, International Society for Optics and Photonics, 1995.
- [49] R. Gordon, R. Bender, and G. T. Herman, “Algebraic reconstruction techniques (ART) for three-dimensional electron microscopy and x-ray photography,” *Journal of Theoretical Biology*, vol. 29, no. 3, pp. 471–481, 1970.
- [50] M. Descour and E. Dereniak, “Computed-tomography imaging spectrometer: experimental calibration and reconstruction results,” *Applied Optics*, vol. 34, no. 22, pp. 4817–4826, 1995.
- [51] L. A. Shepp and Y. Vardi, “Maximum likelihood reconstruction for emission tomography,” *IEEE Transactions on Medical Imaging*, vol. 1, no. 2, pp. 113–122, 1982.
- [52] R. E. Blahut, *Theory of remote image formation*. Cambridge University Press, 2004.

- [53] A. Wagadarikar, R. John, R. Willett, and D. Brady, “Single disperser design for coded aperture snapshot spectral imaging,” *Applied Optics*, vol. 47, no. 10, pp. B44–B51, 2008.
- [54] C. Fernandez, B. D. Guenther, M. E. Gehm, D. J. Brady, and M. E. Sullivan, “Longwave infrared (LWIR) coded aperture dispersive spectrometer,” *Optics Express*, vol. 15, no. 9, pp. 5742–5753, 2007.
- [55] M. Gehm, M. Kim, C. Fernandez, and D. Brady, “High-throughput, multiplexed pushbroom hyperspectral microscopy,” *Optics Express*, vol. 16, no. 15, pp. 11032–11043, 2008.
- [56] S. McCain, M. Gehm, Y. Wang, N. Pitsianis, and D. Brady, “Coded aperture Raman spectroscopy for quantitative measurements of ethanol in a tissue phantom,” *Applied Spectroscopy*, vol. 60, no. 6, pp. 663–671, 2006.
- [57] M. Gehm, R. John, D. Brady, R. Willett, and T. Schulz, “Single-shot compressive spectral imaging with a dual-disperser architecture,” *Optics Express*, vol. 15, no. 21, pp. 14013–14027, 2007.
- [58] Q. Zhang, R. Plemmons, D. Kittle, D. Brady, and S. Prasad, “Joint segmentation and reconstruction of hyperspectral data with compressed measurements,” *Applied Optics*, vol. 50, no. 22, pp. 4417–4435, 2011.
- [59] F. S. Oktem, *Computational imaging and inverse techniques for high-resolution and instantaneous spectral imaging*. PhD thesis, University of Illinois at Urbana-Champaign, 2014.
- [60] J. M. Davila, “High-resolution solar imaging with a photon sieve,” in *SPIE Optical Engineering+ Applications*, International Society for Optics and Photonics, 2011.
- [61] F. S. Oktem, J. M. Davila, and F. Kamalabadi, “Image formation model for photon sieves,” in *2013 IEEE International Conference on Image Processing*, pp. 2373–2377, IEEE, 2013.
- [62] F. L. Pedrotti and L. S. Pedrotti, *Introduction to optics 2nd edition*, vol. 1. New Jersey: Prectice Hall, 1993.
- [63] F. M. Grimaldi, *Physico-mathesis de lumine, coloribus et iride*. Victorii Benatii, 1963.
- [64] C. Huygens, *Traité de la lumière: où sont expliquées les causes de ce qui luy arrive dans la reflexion, & dans la refraction, et particulièrement dans l’etrange refraction du cystal d’Islande*. Chez Pierre vander Aa, 1885.
- [65] D. Attwood, *Soft x-rays and extreme ultraviolet radiation: Principles and applications*. Cambridge University Press, 2007.

- [66] L. Kipp, M. Skibowski, R. Johnson, R. Berndt, R. Adelung, S. Harm, and R. Seemann, “Sharper images by focusing soft x-rays with photon sieves,” *Nature*, vol. 414, no. 6860, pp. 184–188, 2001.
- [67] G. Andersen, “Membrane photon sieve telescopes,” *Applied Optics*, vol. 49, no. 33, pp. 6391–6394, 2010.
- [68] G. E. Artzner, J. P. Delaboudiniere, and X. Song, “Photon sieves as EUV telescopes for solar orbiter,” in *Astronomical Telescopes and Instrumentation*, pp. 158–161, International Society for Optics and Photonics, 2003.
- [69] G. Andersen, O. Asmolov, M. E. Dearborn, and M. G. McHarg, “Falconsat-7: a membrane photon sieve cubesat solar telescope,” in *SPIE Astronomical Telescopes+ Instrumentation*, pp. 84421C–84421C, International Society for Optics and Photonics, 2012.
- [70] F. S. Oktem, J. M. Davila, and F. Kamalabadi, “Image formation model for photon sieves,” in *20th IEEE International Conference on Image Processing (ICIP), 2013*, pp. 2373–2377, IEEE, 2013.
- [71] Q. Cao and J. Jahns, “Focusing analysis of the pinhole photon sieve: individual far-field model,” *JOSA A*, vol. 19, no. 12, pp. 2387–2393, 2002.
- [72] K. Rossmann, “Point spread-function, line spread-function, and modulation transfer function: Tools for the study of imaging systems 1,” *Radiology*, vol. 93, no. 2, pp. 257–272, 1969.
- [73] C. J. Sheppard and I. J. Cooper, “Fresnel diffraction by a circular aperture with off-axis illumination and its use in deconvolution of microscope images,” *JOSA A*, vol. 21, no. 4, pp. 540–545, 2004.
- [74] P. C. Hansen, *Discrete inverse problems: insight and algorithms*, vol. 7. Siam, 2010.
- [75] C. R. Vogel and M. E. Oman, “Fast, robust total variation-based reconstruction of noisy, blurred images,” *IEEE Transactions on Image Processing*, vol. 7, no. 6, pp. 813–824, 1998.
- [76] R. C. Gonzalez and R. E. Woods, “Digital image processing,” *Nueva Jersey*, 2008.
- [77] Z. Wang, A. C. Bovik, H. R. Sheikh, and E. P. Simoncelli, “Image quality assessment: From error visibility to structural similarity,” *IEEE Transactions on Image Processing*, vol. 13, no. 4, pp. 600–612, 2004.